LATVIAN JOURNAL of PHYSICS and TECHNICAL SCIENCES

ISSN 0868 - 8257

4

(Vol. 59)

2022

CONTENTS

LATVIAN JOURNAL of PHYSICS and TECHNICAL SCIENCES

LATVIJAS FIZIKAS un TEHNISKO ZINĀTŅU ŽURNĀLS

ЛАТВИЙСКИЙ ФИЗИКО-ТЕХНИЧЕСКИЙ ЖУРНАЛ

Published six times a year since February 1964
Iznāk sešas reizes gadā kopš 1964. gada februāra
Выходит шесть раз в год с февраля 1964 года

4 (Vol. 59) • 2022

RĪGA

Language Editor: O. Ivanova
Computer Designer: I. Begicevs

INDEXED (PUBLISHED) IN

www.scopus.com
www.sciendo.com
EBSCO (Academic Search Complete, www.epnet.com), INSPEC (www.iee.org.com).
VINITI (www.viniti.ru), Begell House Inc/ (EDC, www.edata-center.com).

Issuers: Institute of Physical Energetics,
Institute of Solid State Physics, University of Latvia
Registration Certificate Number: 000700221

Editorial Contacts:
14 Dzerbenes Street, Riga, LV - 1006
Ph.: + 371 67551732
E-mail: leo@lza.lv
www.fei-web.lv

sciendo

LATVIAN JOURNAL OF PHYSICS
AND TECHNICAL SCIENCES
2022, N 4

DOI: 10.2478/lpts-2022-0029

MATHEMATICAL MODEL FOR HOUSEHOLD OFF-GRID SIMULATION (OFF-GRID SYSTEM SIZING)

E. Groza, K. Gicevskis, O. Linkevics, S. Kiene

Faculty of Electrical and Environmental Engineering,
Riga Technical University,
12/1 Azenes Str., Riga, LV-1010, LATVIA
*e-mail: olegs.linkevics@edu.rtu.lv

The paper presents the results of the research, which was initiated in our previous publication. The main goal of the research is to develop and validate our own multi-objective simulation tool for determination of optimal mix and sizing of off-grid and grid-connected microgrid systems. The first version of the developed model was tailored specifically for simulation of household off-grid system, which consisted of solar photovoltaics (PV), micro wind turbine, electric batteries, and backup power generator. Proposed algorithms are based on simulation of mentioned resources and hourly electric loads of off-grid system with the objective to reduce unsupplied energy volumes and total system costs. Several alternatives were considered with different configurations of the off-grid system and dispatching strategies of available resources. The developed model was validated with calculations of real off-grid system and results were compared to those, which were made in the previous publication, using Homer Pro software.

Keywords: *Annual costs of system, dispatch strategy, microgrid equipment sizing, off-grid system, RES fraction.*

1. INTRODUCTION

In recent years, microgrid systems either when operated in an off-grid or a grid-connected mode have been recognized as one of the most suitable, cost-effective, and sustainable solutions for commercial, industrial, and residential electrification applications [1], [2]. Decreasing costs of renewable energy technologies, fluctuating fossil fuel prices, environmental concerns and security of electricity supply are the main reasons for looking towards the development of emerging microgrid systems [3].

However, research on such systems still must be examined. For instance, microgrids have challenges regarding determination of proper equipment sizing, the voltage and frequency disturbance problems in unpredictable weather conditions, difficulties with monitoring and managing local power generation and loads, along with constrains related to designing protection devices to cope with bi-directional power flows and so on [1]. Within this paper, our focus is on autonomous household scale microgrid equipment sizing problems.

The microgrid equipment sizing is understood as quantification of the power capacities for renewable generators (solar, wind, etc.), as well as for backup power generator and determination of the power (kW) and energy (kWh) capacities of a battery energy storage system (BESS). The proper sizing of the microgrid may reduce the risk of oversize system equipment, which could lead to higher initial capital costs. On the other hand, it may reduce the risk of undersize equipment, which can lead to the poor power supply reliability [4]. Moreover, environmental and social aspects are no less important. Therefore, it is necessary to consider how to minimize emissions, how to promote socially acceptable system development, which includes issues with land use, visual impact, acoustic noise, etc.

According to literature review, several types of methods and different indicators might be considered in the evaluation process of such microgrid equipment. The sizing methods can be classified as classical methods, software tools, hybrid methods and most recently also artificial intelligence methods as shown in Table 1. In the most common cases, four types of indicators are identified which further describe the performance of microgrid: economic indicators (LCOE, LCC, ACS, NPV etc.), reliability indicators (LPSP, LOLP, EENS, etc.), environmental indicators (CE, LCA, EE), and social indicators (HDO, JC, SA, etc.) [5], [6].

In addition to the review mentioned above, some articles have summarised the latest trends of algorithm and indicators, and future overall challenges of microgrid sizing methodologies. For example, ant colony (ACO), firefly algorithm (FA), particle swarm optimization (PSO) and genetic algorithm (GA) and their performance were comprehensively analysed by [7] regarding how to select an appropriate algorithm to solve non-linear problems in the context of storage-based off-grid systems under different alternatives. The results reveal that FA performs better, with the least relative error. Other paper [2] evaluated sizing of an autonomous microgrid considering droop control. Results indicated that a competitive total cost could be obtained if the droop parameters were calculated considering the microgrid sizing results. Electric system cascade extended analysis was developed in [8]. In it, the LPSP, LCC and the LCOE together with tri-objective optimization functions were implemented and validated with system advisor model software. Authors of this paper argue that this analysis might help choose the suitable RES capacities for any site worldwide. In [9], a model for a remote community off-grid PV/diesel system using dynamic modelling and artificial neural network (ANN) techniques was developed. Within a comparative analysis, authors concluded that utilising dynamic and predictive modelling techniques would enable the model to be expandable, and simple to use while still maintaining its accuracy. Using an iterative approach based on a recursive algorithm, improvements were made to a techno-economic optimal sizing technique of a hybrid off-grid microgrid system in [6]. However, a new mutation adaptive differential evolu-

tion (MADE) based on a multi-objective optimization algorithm is presented in [10] to optimise the configuration of the off-grid stand-alone photovoltaic systems. It is also worth mentioning the authors of previous publication [4] which showed how important it was to choose the right dispatch strategy for off-grid system regarding equipment sizing, and at the end how it affected the net present costs (NPC) over the project lifetime.

Table 1. Microgrid Equipment Sizing Methods and Indicators [5], [6]

Type of sizing methods	**Type of indicators**
Classical: - probabilistic - analytical - numerical - iterative	**Economic:** -levelized cost of electricity (LCOE) -life cycle cost (LCC) -annualized cost of system (ACS) -total net present value (NPV)
Software tools: - Homer Pro - RETScreen, - PVSOL - Hybrid 2 - Transys	**Reliability**: - loss of power supply probability (LPSP) - loss of load probability (LOLP) - expected energy not supplied (EENS) - deficiency of power supply probability (DPSP) - loss of load expected (LOLE), - loss of energy expected (LOEE)
Hybrid methods: - combined dynamic programming and region-elimination technique algorithm (DP-RET) - hybrid Simulated Annealing–Tabu Search - hybrid Big Bang-Big Crunch algorithm (HBB -BC) - hybrid GA-mixed integer linear programming (GA-MILP)	Environmental: - carbon emission (CE) - embodied energy (EE) - carbon footprint of energy (CFOE) - life cycle assessment (LCA)
Artificial intelligence: - genetic algorithm (GA) - particle swarm optimization (PSO) - simulated annealing (SA) - ant colony optimization (ACO) - artificial bee colony (ABC)	**Social**: - human development index (HDI) - job creation (JC) - portfolio risk (PR) - social acceptance (SA) - social cost of carbon (SCC)

In general, according to the literature review, it can be noticed that there are still difficulties in the field of equipment capacity optimization:

1. improvements in load forecasting and adoption to methods are necessary;
2. calculation time step of power output is critical for the optimization of the results; thus, it should be reduced considerably as much as possible (less than 1 hour is preferable);
3. improved sizing methods equipment could be installed in the research area to obtain real-time data and verify simulation results;
4. new evaluation indicators may be used to provide more effective and overall assessment as the microgrids are emerging solutions for sustainability policy goals;
5. artificial intelligence sizing methods have advantages in accuracy and computation speed compared to traditional methods, while, on the other hand, those significantly increase optimization complexity;
6. as good practice equipment sizing is validated and improved also with more than one optimization tool.

It can also be concluded that existing

articles mainly focus on microgrid operation state; therefore, future research might have more efforts on the planning, construction state, and microgrid servicing.

The main aim of the present research is to introduce a new multi-objective simulation tool to evaluate the performance of several off-grid cases under different dispatch approaches, which would further increase knowledge of such systems and flexibility of already existing simulation tools. The developed tool is used to justify a composition and capacities of an off-grid system equipment for the real pilot project, which currently is under implementation. It is expected that this approach can be used and easily replicated for configurations that are more complex.

2. MODEL FOR THE HOUSEHOLD OFF-GRID SIMULATION

The simulation model described in the present research was developed for the real case evaluation. At that time, the information for the sizing of the system was rather insufficient. The model determined necessary generation and storage capacities, helped assess the payback of the off-grid project and allowed visualising operating conditions.

The model has been applied to an off-grid system composed of solar PV, wind turbine, battery energy storage system (BESS or battery) and backup power generator. The model presented in this section is designed as a set of algorithms, which determine the operation of off-grid solution according to the load and supply power balances as indicated in Fig. 1 and Table 2.

Table 2. Parameter Abbreviations

Parameter	Abbr.	Parameter	Abbr.	Parameter	Abbr.
Electric load (kW)	P_l	Max amount of energy of the battery (kWh)	E_{bmax}	Power of PV modules (kW)	P_{gPV}
Generated power (kW)	P_g	Min amount of energy of the battery (kWh)	E_{bmin}	Power of wind generators (kW)	P_{gW}
Other generation capacities (kW)	P_n	State of charge of the battery (%)	SOC	Rated power of backup generator (kW)	P_r
Rated power of the battery (kW)	P_{br}	Max state of charge of the battery (%)	SOC_{max}	Minimal power of backup generator	P_{rmin}
Rated energy capacity of the battery (kWh)	E_{br}	Min state of charge of the battery (%)	SOC_{min}	Levelized costs of electricity, EUR/kWh	LCOE

The model has been developed to provide the highest (close to 100 %) electricity availability, considering that the electricity generation sources (PV, wind, etc.) connected to the off-grid are stochastic. Thus, energy storage and backup generator are needed.

For simplicity, the time interval for modelling of off-grid system is assumed to be one hour; thus, the load and at the same time the required generation capacity are defined as *Pl* in the time interval *t*. Total power generated (kW) at the time interval *i* (excluding backup generator) *Pg(i)* in Eq. (1) is defined as the sum of power capacity of solar modules, wind turbine and potentially other generation sources such as fuel cell, small-scale CHP unit, etc.

$$P_{g(t)} = P_{gPV(t)} + P_{gW(t)} + \ldots + P_{n(t)}. \quad (1)$$

As the off-grid system requires a battery energy storage system, it is necessary to determine its state of charge status at the time interval *t*:

$$\mathrm{SOC_{(t)}} = \mathrm{SOC_{(t-1)}} + \frac{\mathrm{E_{b(t)}}}{\mathrm{E_{br}}}, \quad (2)$$

where $\mathrm{SOC_{(t-1)}}$ is the state of charge of the BESS in the previous time interval, $\mathrm{E_{br}}$ is the rated energy capacity of the BESS, $\mathrm{E_{b(t)}}$ is the amount of energy BESS charged or discharged in the time interval. In addition, the model calculates the maximum possible charge and discharge capacities (kW) of the BESS (4), which at the same time gives us the amount of energy per cycle. During the first cycle $\mathrm{SOC_{(t)}}=\mathrm{SOC_{max}}$:

$$E_{bmax} = \left(SOC_{(t)} - SOC_{min}\right) \times E_{br}. \quad (3)$$

$P_{bmax}=E_{bmax}$, for time interval t = 1h. (4)

If there is a surplus or shortage of electricity (kW) at the time interval *t* in the off-grid system, Eq. (5) is used:

$$P_{(t)} = P_{g(t)} - P_{l(t)}. \quad (5)$$

In next equations (6 and 7), the model assesses whether to start-up the back-up generator and at what power:

$$\text{if } P_{bmax(t)} < P_{(t)}; \quad (6)$$

$$P_{r(t)} = P_{br} - P_{bmax(t)} - P_{(t)}. \quad (7)$$

If the BESS and other sources can cover the load, the backup generator will not be scheduled for operation. If not, the power output of the back-up generator during the time interval *t* is determined within the range P_{rmin}-P_r. The calculation is adjusted so that the back-up generator operates closer to the nominal (rated) output and charges the battery at maximum possible power during the time interval *t*.

The actual power rating (kW) of the BESS and its nature (charging / discharging) in the model is determined by Eq. (8):

$$P_{b(t)} = P_{(t)} + P_{r(t)}. \quad (8)$$

The actual charged or discharged energy rating (kWh) of the BESS $\mathrm{E_b(i)}$ at the time interval is determined by Eqs. 9–11:

$$if\, P_{b(t)} > 0, then\, k_{b(t)} = 0.9; \quad (9)$$

$$if\, P_{b(t)} < 0, then\, k_{b(t)} = 1/0.9; \quad (10)$$

$$E_{b(t)} = P_{b(t)} \times k_{b(t)} \times 1h, \quad (11)$$

where k_b is the efficiency of the BESS. The simulation cycle ends with Eq. 11) to initialize calculations for the next time interval *t*:

$$t = t + 1. \quad (12)$$

Fig. 1 shows a block scheme within the sequence of operations of the described off-grid system.

The annual costs and levelized cost of energy (LCOE) of the off-grid system are determined in a separate algorithm. Before using the algorithm, configuration of the model is necessary to set up the required dispatching strategy and input data.

The overall model optimization focuses on four aspects: off-grid system highest availability, lowest surplus generation, lowest operation hours of the backup generator, lowest LCOE.

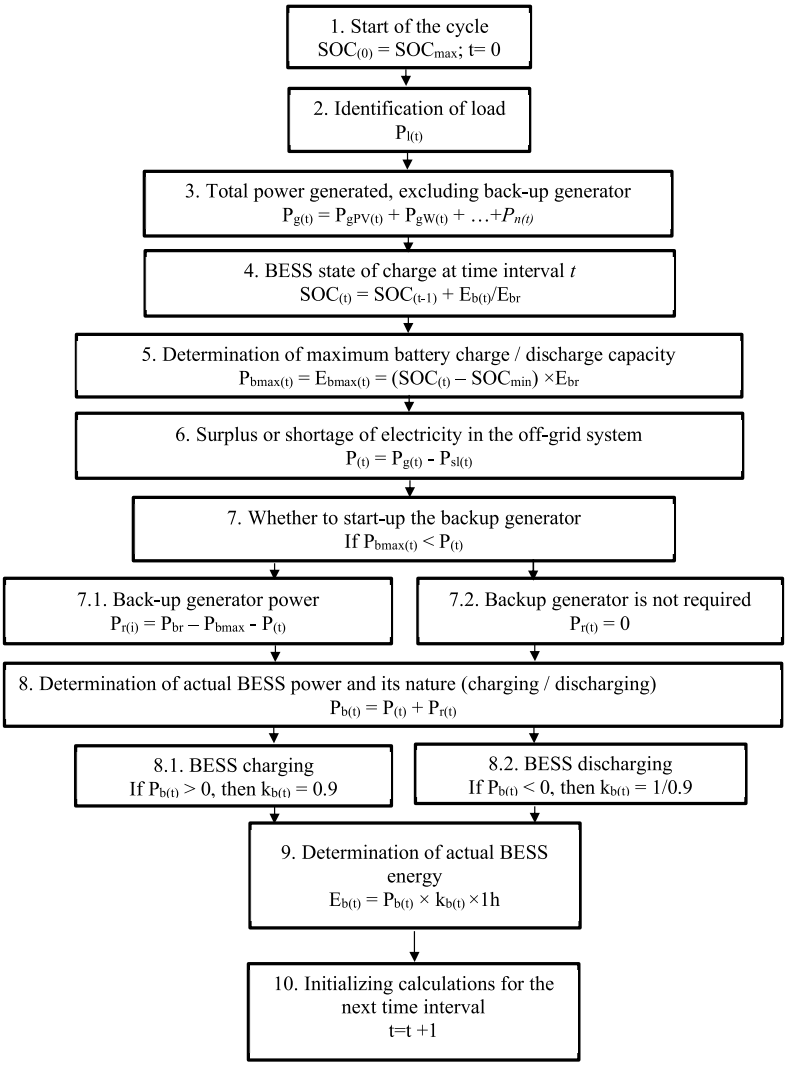

Fig. 1. Operational principles of the model of off-grid system.

3. ANNUAL COSTS OF OFF-GRID SYSTEM

The objective function in the calculations is minimization of the levelized cost of electricity (LCOE), which in this case is determined based on the method of the annual cost of system (ACS) [11].

ACS covers annual capital cost (ACC), annual operation and maintenance costs (AOM), annual replacement costs (ARC), annual fuel costs of backup generator (AFC) and annual emission cost (AEC). ACS (in EUR) is estimated as follows:

$$ACS = ACC + AOM + ARC + AFC + AEC. \quad (13)$$

Annual capital cost (in EUR) of each unit which does not need replacement during project lifetime, such as PV system, wind turbine, back-up generator and inverter, is calculated as follows:

$$ACC = C_{cap} \cdot CRF(i, y), \quad (14)$$

in which

$$CRF = \frac{i \cdot (1+i)^y}{(1+i)^y - 1}, \quad (15)$$

where C_{cap} is the capital cost of each component in EUR, but *y* is the project lifetime in years. *CRF* is capital recovery factor, a ratio to calculate the present value of a series of equal annual cash flows, and *i* is the annual real interest rate.

The annual operation and maintenance cost as a function of capital cost, reliability of components (λ) and their lifetime (y) can be determined using the following equation:

$$AOM = C_{cap} \cdot \frac{1-\lambda}{y}. \quad (16)$$

ARC is the annual cost value (in EUR) for replacing units during the project lifetime. In this study, a unit that needs replacement is only battery banks. Other units do not require replacement because their lifetime is the same as project lifetime. Economically, annual replacement cost is calculated as follows:

$$ARC = C_{rep} \cdot SFF(i, y_{rep}), \quad (17)$$

where C_{rep} is the replacement cost of battery banks in EUR, but is the lifetime of battery banks in years. In this case, the replacement cost of battery banks is like its capital cost. *SFF* is the sinking fund factor, a ratio to calculate the future value of a series of equal annual cash flows. This factor is calculated as follows:

$$SFF = \frac{i}{(1+i)^y - 1}. \quad (18)$$

AFC of backup generator unit is estimated based on optimum dispatch of backup generator system. The fuel consumption (in liters) based on load characteristic of the back-up diesel generator is calculated for each time interval *t* using the following equation:

$$F(t) = 0.246 \cdot P_r(t) + 0.08415 \cdot P_r, \quad (19)$$

where is the rated power of backup generator in kW, $P_r(t)$ is the actual power generated at time interval *t* in kWh. The fuel cost (in EUR) is calculated for a year by multiplying hourly fuel consumption by fuel costs:

$$AFC = C_f \cdot \sum_{t=1}^{8760} F(t), \quad (20)$$

where C_f is the fuel cost per litre (EUR/l). To reach the maximum efficiency of operation the unit should be operated within rated power and specified maximum value.

AEC is the annual emission cost (in EUR) to capture CO_2 emission generated from backup generator system. The AEC can be expressed as follows:

$$AEC = \sum_{t=1}^{8760} E_f \cdot E_{cf} \cdot P_r(t)/1000, \quad (21)$$

where E_f is the CO_2 emission factor, kg/kWh, E_{cf} is the CO_2 emission cost in EUR/t.

By calculating the ACS it is possible to determine levelized cost of electricity (LCOE), which shows how much each kWh of electricity costs in the particular microgrid (EUR/kWh).

$$LCOE = \frac{ACS}{E_{AEC}}, \quad (22)$$

where is the annual energy consumption of a microgrid (kWh). Other parameters used in the calculations are shown in Table 3.

Table 3. The Economic Data Considered for Calculations

Parameter	Data	Parameter	Data	Parameter	Data
Project lifetime (years)	20	Reliability of PV panel (coef.)	0.98	Cost of Wind turbine (EUR/kW)	3500
Real interest rate (%)	4	Reliability of wind turbine (coef.)	0.8	Cost of battery bank (EUR/kWh)	540
PV panel lifetime (years)	25	Reliability of inverter (coef.)	0.98	Cost of battery bank (EUR/kW)	540
Wind turbine lifetime (years)	20	Reliability of battery (coef.)	0.98	Cost of inverter (EURkW)	1300
Inverter lifetime (years)	20	Reliability of backup generator (coef.)	0.9	Fuel cost (Cf) (EUR/l)	1.2
Battery lifetime (years)	10	Cost of backup generator (EUR/kW)	380	Emission factor (kg/kWh)	0.34
Backup generator lifetime (hours)	15 000	Cost of PV panel (EUR/kW)	1250	Emission cost (EUR/t)	30

The parameters shown in Table 3 can be changed as needed for other microgrids.

4. CASE STUDY

For the case study, real household hourly load data are collected, integrated in the model, and used in simulations. Household average daily electricity demand is 30.27 kWh, which reaches 11.049 MWh on an annual basis. The household consists of 2 persons. A heat pump, which is used for heat and hot water supply, and an electric vehicle for transports needs can be considered the biggest consumers of electricity in this household. This type of household matches with aims for electrification, which has a critical role to play for achieving the European Union decarbonization policy targets.

Fig. 2 shows the typical daily load curve (for 24-hour period) of this household, with a heat pump and electric vehicle charging. The largest amount of electricity is consumed at nighttime while an electrical vehicle is charging. For the case, it is highly important to choose the appropriate generation and storage solutions. When the readings were taken, the household was connected to the distribution system operator grid; thus, the energy availability were not an issue and always corresponded with the demand. Nonetheless, the connection allows the household not to consider load shifting.

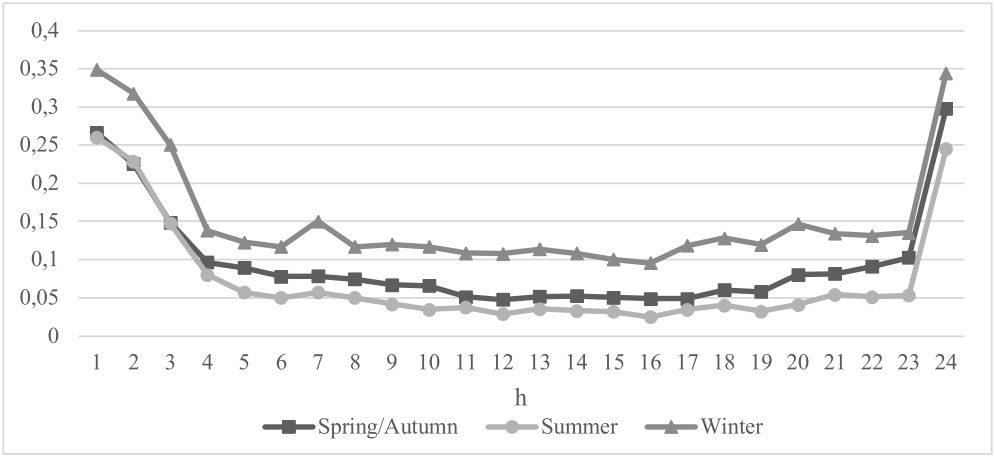

Fig. 2. Daily load curve in relative values for three seasons.

As shown in Table 4, five equipment sizing alternatives were evaluated. First three sizing alternatives are taken from the previous research on microgrid sizing with Homer software. The capacity of the back-up generator is at least 11 kW considering that system must cover the maximum daily load (which is around 9 kW), thus ensuring higher security of supply [4]. Two additional sizing options were developed to find the most sustainable and economically efficient solution.

Table 4. Average Equipment Size for All Alternatives

System equipment	1st alternative	2nd alternative	3rd alternative	4th alternative	5th alternative
BESS (kW)	4.7	5	5	8.2	8.2
BESS (kWh)	22	28.3	17.8	30	16
Solar panels (kW)	4	9.4	0	6.2	3
Wind (kW)	3	0	4	2	2
Backup generator (kW)	11	11	11	13	13

In this study, the results are displayed for the following alternatives: three dispatch strategies, different sizing options, power sources PV, wind, BESS, backup generator, the dispatch strategy is combined, and there is no capacity shortage.

5. RESULTS

Table 5 shows the results for all five equipment sizing alternatives considering three different dispatch strategies.

Table 5. Results of Simulations

Alternative	**1st**	**2nd**	**3rd**	**4th**	**5th**
Combined charging dispatch strategy (CCDS)					
Backup gen. operating hours	1277	1234	1448	778	953
Excess renewable energy, kWh	1290	3990	71	2083	1029
Excess vs. total renew. generation, %	18 %	40 %	2 %	26 %	20 %
LCOE, EUR/kWh	0.71 €	0.73 €	0.73 €	0.79 €	0.70 €
Load following strategy (LFS)					
Backup gen. hours	2249	2276	2804	1923	2333
Excess renewable energy, kWh	1073	3646	46	1870	676
Excess vs. total renew. generation, %	13 %	33 %	1 %	21 %	10 %
LCOE, EUR/kWh	0.81 €	0.83 €	0.87 €	0.91 €	0.85 €
Cycle charging strategy (CCS)					
Backup gen. hours	1406	1355	1561	949	1248
Excess renewable energy, kWh	2273	5336	293	2999	1408
Excess vs. total renew. generation, %	32 %	52 %	7 %	37 %	26 %
LCOE, EUR/kWh	0.78 €	0.80 €	0.80 €	0.87 €	0.83 €

Like Homer Pro software, while setting up the project, using a simulation tool it is possible to configure dispatch strategies to determine operating principles of how generation can provide the load.

1) Combined charging dispatch strategy (CCDS) – intelligently switches between load following and cycle charging strategy. That way it can improve performance over the cycle charging and load following dispatch strategies by making more efficient use of back-up generator.

2) Load following strategy (LFS) – when a generator is needed, it produces only enough power to meet the demand. It tries not to charge battery with back-up diesel generator unless it reaches the minimum power of generator. Load following tends to be more optimal in off-grid systems with a lot of renewable power that sometimes exceeds the load.

3) Cycle charging strategy (CCS) – whenever a back-up generator is required, it operates at full capacity, and surplus power charges the battery bank. It stops charging battery at the setpoint of battery state of charge. Cycle charging tends to be more optimal in off-grid systems with little or no renewable power.

To better understand how different dispatch strategies impact the operation of generating sources and BESS charging/discharging, the visualization of off-grid operation in summer and winter day for two equipment sizing alternatives and three dispatch strategies is provided in Table 6 and 7. The graphs show the power source and amount of generation, energy storage capacity, load and its nature, battery power and its nature, backup generators power. The dates were chosen to represent the extreme situations where there was surplus or deficiency of renewable generation. During the observation period, there was low wind output on 7th July and low PV output on 13th November. By comparing the 2nd and the 5th alternatives, it is clearly visible that the microgrid benefits of diversified generation sources allow minimising the backup generators workload and maximising the share of renewables. Dispatch strategies pose the most impact on LCOE.

Table 6. Visualization of Off-Grid Operation for the 2nd Alternative and Dispatch Strategies

2nd alternative: BESS power 5 kW, capacity 28.3 kWh, solar power 9.4 kW, wind power 0 kW, diesel gen. 11 kW	
Date	13th November
Combined charging CCDS	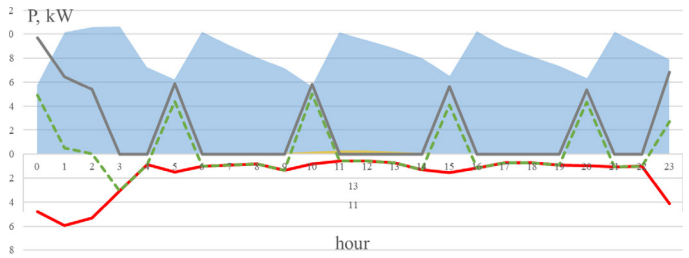
Load following LFS	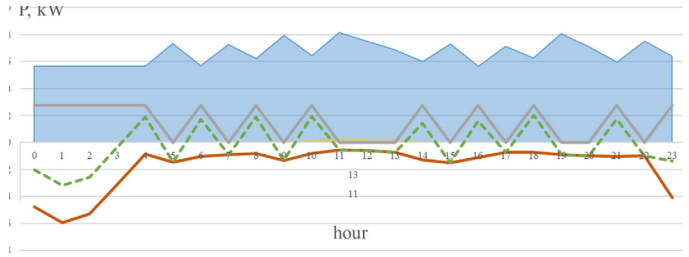
Cycle charging CCS	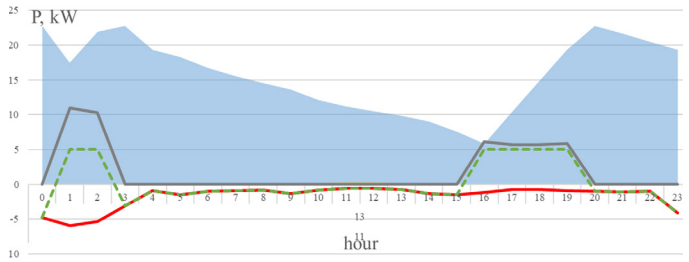
Date	7th July
Combined charging CCDS	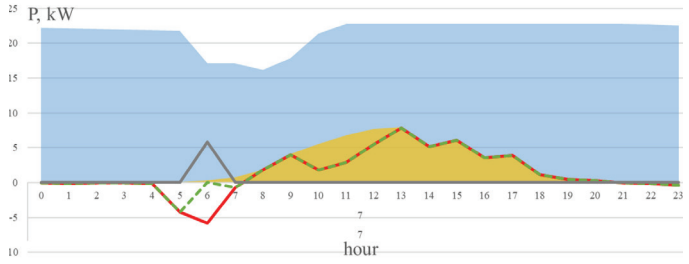
Load following LFS	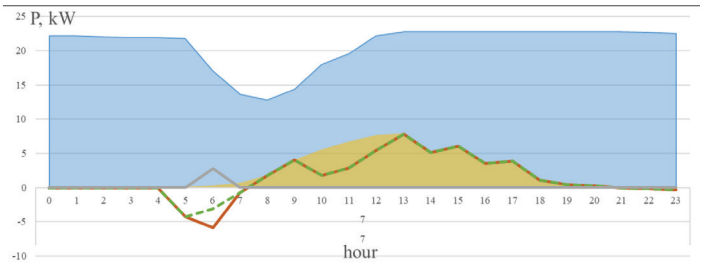

Cycle charging CCS	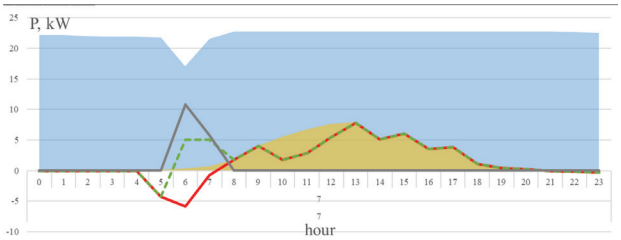
LEGEND	

Table 7. Visualization of Off-Grid Operation for the 5th Alternative and Dispatch Strategies

5th alternative: BESS power 8.2kW, capacity 16kWh, solar power 3 kW, wind power 2kW, diesel gen. 13 kW	
Date	13th November
Combined charging CCDS	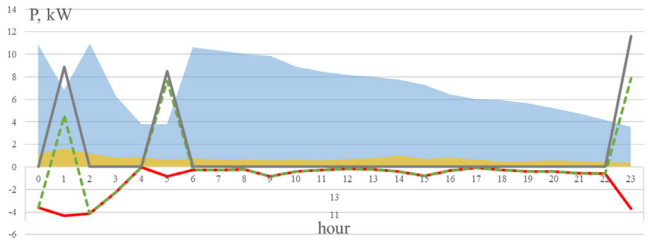
Load following LFS	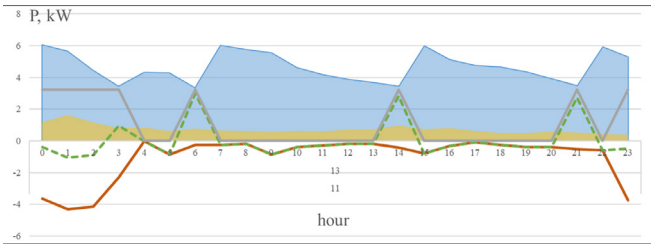
Cycle charging CCS	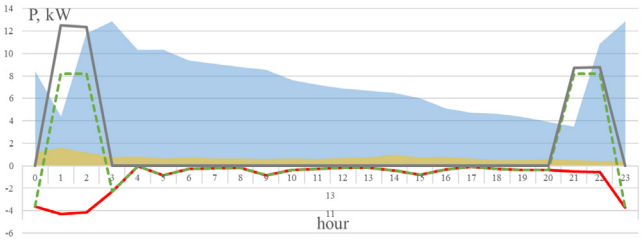
Date	7th July
Combined charging CCDS	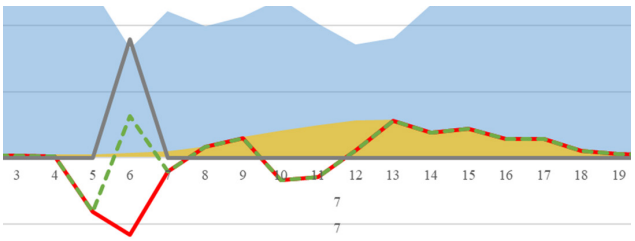

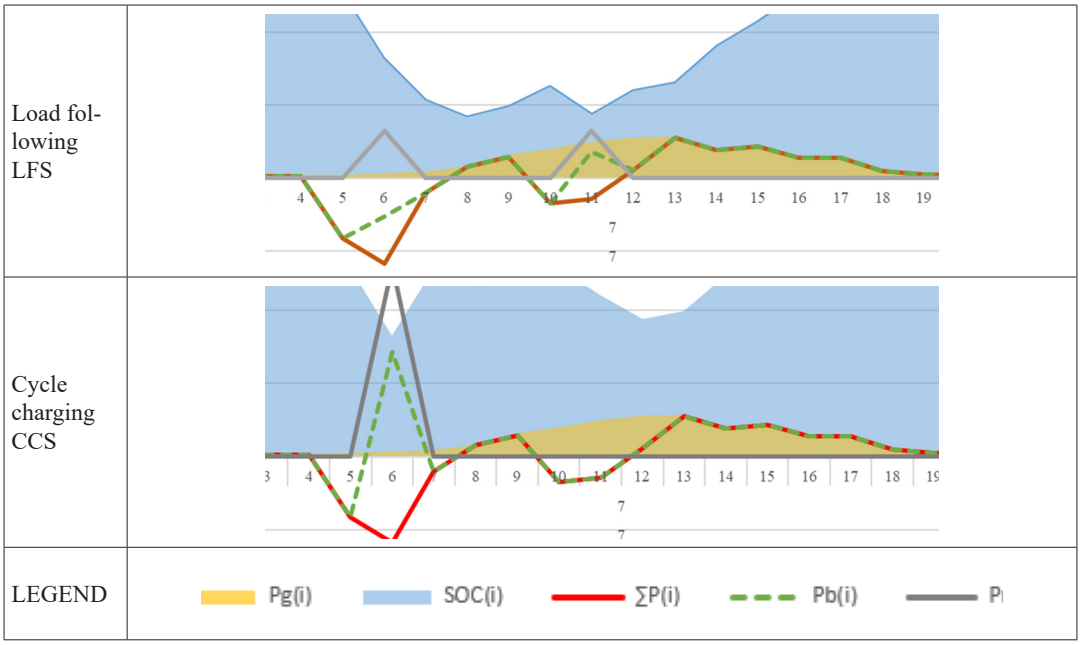

In addition to the analysis before, in the next three figures comparison of results between the new simulation tool and Homer Pro software is made.

Firstly, backup generator operating hours are analysed. As it is necessary to avoid the use of electricity produced by the backup generator when renewable energy can be used instead, it is necessary to pay attention to the operating hours of the backup generator. As shown in Fig. 3, in all alternatives and dispatching strategies, the new tool displays more backup generator hours than Homer Pro software. The largest difference is observed at load following strategy (LFS). Nevertheless, both tools show that the generator hours will be the smallest for the 1st alternative at combined charging dispatch strategy (CCDS).

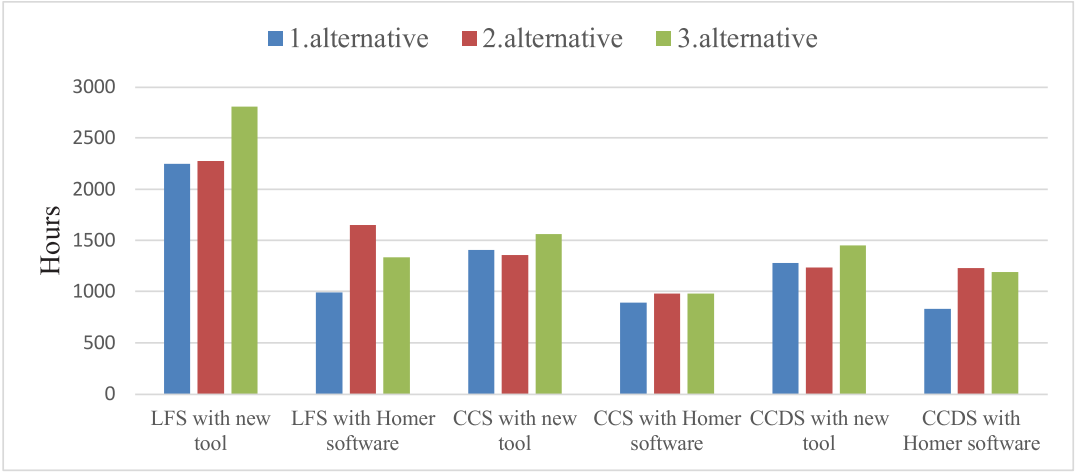

Fig. 3. Backup generator operating hours.

Secondly, "excess electricity" is analysed. Excess electricity occurs when surplus power in off-grid is produced (either by the back-up generator or by a renewable sources) and the battery or load is unable to take all electricity. Excess electricity as the percentage (%) of the total generation of three off-grid alternatives and three different dispatch strategies is shown in Fig. 4.

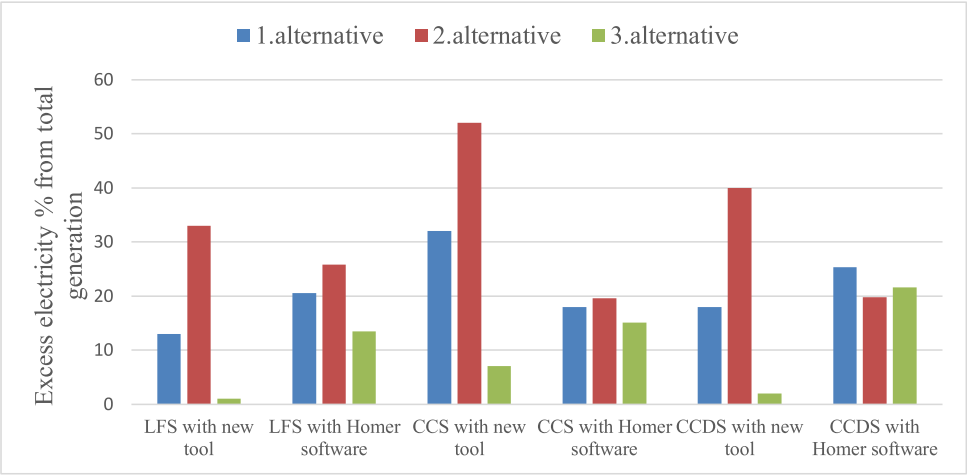

Fig. 4. Excess electricity in the all off-grid alternatives.

In average, for both tools the smallest "excess electricity" was shown by the third alternative – 10.03 %, followed by the first alternative (21.13 %) and the second alternative (31.7 %). Despite excess electricity (%) differs between the tools (especially for an alternative that includes wind), the overall trend is the same and it shows, that if the off-grid system consists of PV panels then it is crucial to correctly size its capacity and match it with adequate storage capacity.

Finally, in Fig. 5 we compare three alternatives regarding the levelized cost of electricity as the average cost per kWh of useful electrical energy produced by the system. We did not cover the LCOE in our previous publication, but we use the gained results this time.

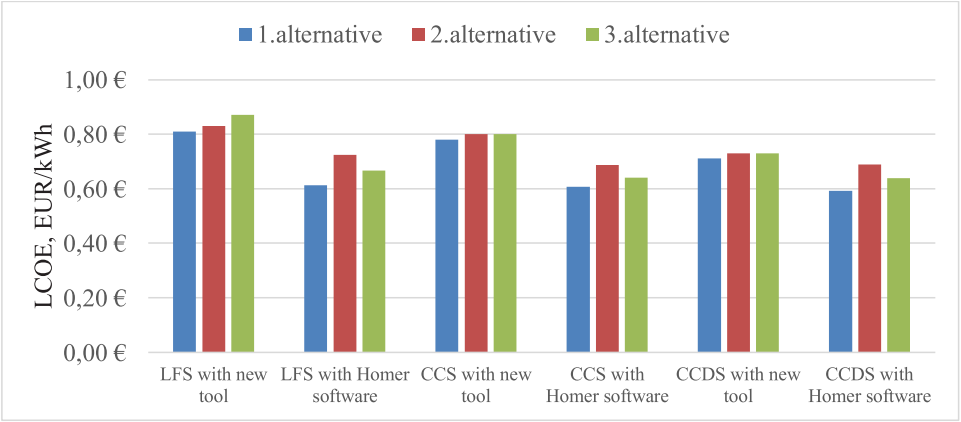

Fig. 5. Levelized cost of electricity for all off-grid alternatives.

As shown in Fig. 5, for the new tool average costs are between 0.72 EUR/kWh and 0.84 EUR/kWh, while in case of Homer Pro software they range from 0.64 EUR/kWh to 0.67 EUR/kWh. The results differ due to the emission cost implemented in the new tool and difference in models themselves. In general, both simulation tools show similar trends, which confirms and validates their accuracy.

6. DISCUSION AND CONCLUSION

The case study and comparison of results to the authors' previous publication have shown that new multi-objective simulation tool can be used as an assessment tool for microgrid equipment sizing determination. It allows analysing potential generation by source, BESS charging / discharging versus the required load, calculating annual system costs and other parameters. It gives all the necessary key values to evaluate the possibility to create a microgrid solution.

By comparing simulation results of the new multi-objective simulation tool (considered in this publication) and Homer software (from the previous publication), it can be concluded that both tools show similar trends with regard to three parameters: backup generator operating hours, excess electricity and LCOE. The differences in results might be caused by additional emission cost (30 EUR/t), and only one capacity shortage level – 0 %, which was not the case in the previous publication using Homer Pro software. Another reason for the differences may be related to approaches/algorithms themselves which differ in both tools.

Furthermore, if we compare the two additional alternatives (4th and 5th), we see that the most sustainable and economically efficient solution would be using the combined charging dispatch strategy. However, there is no solution which would correspond to "the greenest and optimal solution". On the one hand, the 4th alternative is with fewer backup generator operating hours – 778; on the other hand, the 5th alternative has an LCOE of less than 0.09 EUR/kWh comparing with the 4th alternative. Thus, the end user must decide on dilemma whether to use a "sustainable" or "economically efficient" solution.

In this publication, the results again show that the dispatch strategy has great impact on the microgrid costs. Nevertheless, like Homer Pro software, the case study revealed that the combined charging dispatch strategy (CCDS) with both solar and wind sources is the most suitable one of all the alternatives.

Practically, both tools have their advantages and disadvantages. The Homer Pro allows highly automatizing the sizing offering, thus providing a quick multi scenario approach. While our own developed simulation model gives advantage to tweak the equipment sizing for very specific cases and can be further implemented on multiple software tools taking into account users' preferences. It can be used to validate results from other software tools as well.

The battery rated power should be at least as large as the sum of non-dispatchable generation. In case there is no load and there is full generation power, it is highly significant to store every generated kWh. At the same time, it should be greater than backup generator minimal power – in case of small load and empty battery, the generator will not be used sufficiently. As there is load from electrical vehicle in consumption the amount of energy the BESS should hold

should be close to the battery capacity of the electric vehicle; otherwise, electric vehicle might be charged with diesel generator if no renewables are present.

For the further research it would be useful to compare the model against real case off-grid microgrid solution.

REFERENCES

1. Gao, D. (2015). Basic Concepts and Control Architecture of Microgrids. *Energy Storage for Sustainable Microgrid,* 1–34.
2. Rey, J. M., & Vergara, P. P. (2022). Sizing of an Autonomous Microgrid Considering Droop Control. *International Journal of Electrical Power and Energy Systems, 136*, 1–10. doi: 10.1016/j.ijepes.2021.107634.
3. Manbachi, M. (2018). *Energy Management Systems for Hybrid AC / DC Microgrids: Challenges and Opportunities*. Elsevier Inc.
4. Gicevskis, K., Linkevics, O., Gorza, E., & Kiene, S. (2021). Multiple scenario and criteria approach for optimal solution and sizing of household off-grid system. In *2020 IEEE 8th Workshop on Advances in Information, Electronic and Electrical Engineering (AIEEE 2020),* (pp. 31–37). 22–24 April 2021, Vilnius, Lithuania.
5. Lian, J., Zhang, Y., Ma, C., Yang, Y., & Chaima, E. (2019). A Review on Recent Sizing Methodologies of Hybrid Renewable Energy Systems. *Energy Convers. Manag.*, *199*, 112027. doi: 10.1016/j.enconman.2019.112027.
6. Amara, S., Toumi, S., Ben, C., & Salah, A. (2021). Improvement of Techno-Economic Optimal Sizing of a Hybrid Off-Grid Micro-Grid System. *Energy*, *233*, 121166. doi: 10.1016/j.energy.2021.121166.
7. Shahzad, M., Ma, T., Jurasz, J., Ahmed, S., & Mikulik, J. (2020). Performance Comparison of Heuristic Algorithms for Optimization of Hybrid Off-Grid Renewable Energy Systems. *Energy*, *210*, 118599. doi: 10.1016/j.energy.2020.118599.
8. Chennaif, M., Maaouane, M., Zahboune, H., & Elhafyani, M. (2021). Tri-Objective Techno-Economic Sizing Optimization of Off-Grid and On-Grid Renewable Energy Systems Using Electric System Cascade Extended Analysis and System Advisor Model. *Appl. Energy*, *305*, 117844. doi: 10.1016/j.apenergy.2021.117844.
9. Yap, W. K., & Karri, V. (2015). An Off-Grid Hybrid PV / Diesel Model as a Planning and Design Tool, Incorporating Dynamic and ANN Modelling Techniques. *Renew. Energy*, *78*, 42–50. doi: 10.1016/j.renene.2014.12.065.
10. Mohammed, H., Gomes, C., & Hazim, H. (2020). Sizing and Implementing Off-Grid Stand-Alone Photovoltaic / Battery Systems Based on Multi-Objective Optimization and Techno-Economic (MADE) Analysis. *Energy*, *207*, 118163. doi: 10.1016/j.energy.2020.118163.
11. Suryoatmojo, H. & Elbaset, A. A., Syafaruddin .., & Hlyama, T. (2010). Genetic algorithm Based Optimal Sizing of PV-Diesel-Battery System Considering CO2 Emission and Reliability. *International Journal of Innovative Computing, Information and Control*, *6*, 4631–4649.

sciendo

LATVIAN JOURNAL OF PHYSICS
AND TECHNICAL SCIENCES
2022, N 4

DOI: 10.2478/lpts-2022-0030

ENERGY TRANSPORT IN SiO_2 CRYSTALS: LUMINESCENCE EXCITATION SPECTRA OF STISHOVITE AND α-QUARTZ

A. N. Trukhin

Institute of Solid State Physics, University of Latvia,
8 Kengaraga Str., Riga, LV-1063, LATVIA
email: truhins@cfi.lu.lv

The migration of elementary electronic excitations was studied in a single crystal of stishovite and compared with migration in a crystal of α-quartz and polycrystalline stishovite powder. The research method is based on comparing the transfer of absorbed energy to luminescence centers, used as detectors of quasiparticles, and the near-surface nonradiative annihilation of electronic excitations. A sign of migration is the appearance of some minima in the photoluminescence (PLE) excitation spectrum in the region of maxima in the intrinsic absorption spectrum. The PLE spectrum of stishovite contains the first minimum at 9.8 eV, indicating the migration of electronic excitations and the existence of an intrinsic absorption band in stishovite at 9.8 eV. In α-quartz, the first minimum in the PLE spectrum is located at 10.5 eV and corresponds well to the intrinsic absorption band of the exciton.

Keywords: Electronic excitations migration, photoluminescence excitation, stishovite single crystal.

1. INTRODUCTION

The method for studying energy migration is based on the transfer of energy absorbed by the material to the luminescence center by the corresponding elementary electronic excitations created by the exciting light. The effect of modulating the transmission efficiency of the penetration depth of the exciting light due to the different absorption levels in the intrinsic spectrum of the material is used as a sign of energy migration. (See for example [1]–[3]). If moving elementary electronic excitations (which are the same as quasiparticles) are created in the material by

light, then their number approaching the luminescence center, which plays the role of a quasiparticle detector, depends on the competitive process of diffusion of quasiparticles into the near-surface region, where they annihilate nonradiatively. The thinner the absorbing layers, for high values of the absorption coefficient, the less the number of particles reaches the luminescence center, which is evident from the decrease in the luminescence quantum yield. Thus, at the maximum of the absorption band, a minimum luminescence yield is observed if the quasiparticles are mobile. Relationship between the yield of luminescence excited by the transfer of electronic excitations and the absorption coefficient [1] is given by:

$$\eta = K \cdot h\nu \cdot (1 + \alpha L)^{-1}, \quad (1)$$

where α is the absorption coefficient, $h\nu$ is the photon energy, K is a constant, $L = (D\tau)^{1/2}$ is the diffusion length, D is the diffusion coefficient, and τ is the quasiparticle life time.

The energy transfer spectra of the α-quartz [3], [4] are in good agreement with expression (1) in comparison with the known optical absorption spectrum in the intrinsic range. For a stishovite crystal, such an absorption spectrum is not yet known, even the optical reflection spectra have not yet been measured. Measurement of the energy transfer spectra from the luminescence excitation spectra would make it possible to qualitatively understand the features of the intrinsic absorption spectrum of stishovite. For a single crystal of stishovite, such measurements have not yet been carried out due to difficulties with the small size of the available single crystals. For the case of stishovite in the form of powder, the luminescence excitation spectra are measured [5] and I would very much like to get the spectra of a single crystal.

In fact, a comparison of the optical properties of the stishovite crystal and the α-quartz crystal revealed differences in the positions of the intrinsic absorption edges. For α-quartz crystal, the intrinsic absorption edge obeys the Urbach rule in the form interpreted by Toyozawa (see, e.g., [6]). This means an exponential spectral dependence with a shift towards lower energy as the temperature rises. At 293 K, the absorption coefficient is 10 cm^{-1} at 8.5 eV. At 600 K, the same absorption level occurs at 7.9 eV. For a single crystal of stishovite, the fundamental absorption edge does not depend on temperature, the level of the absorption coefficient equal to 10 cm^{-1} is at 8.75 eV [7].

Stishovite has not yet been sufficiently studied; however, theoretical and experimental approaches to the study have now begun and the first results have been obtained [7]–[10]. These publications revealed the luminescence of defects present in the grown stishovite single crystal. In a freshly grown single crystal of stishovite, two types of luminescence centers with two bands were observed. One UV (4.75 eV), the other blue (3.1 eV) [7] are observed under excitation of x-ray [8], e-beam [9] and excimer lasers [10]. The process of luminescence excitation is complex. One part of the process is associated with intracenter excitation of the defect. In this case, a rapid decay of photoluminescence is observed, amounting to ~ 17 μs for the blue band and 1–2 ns for the UV band at 80 K [11]. Another part of the process is recombination. Thus, the effect of increasing the photoluminescence duration up to ms for the blue band and up to tens of microseconds for the UV band was discovered when a single crystal of stishovite was heated even to a high (340 K) temperature [12]. The effect is explained by the formation of a certain complex with an OH group or / and a diamond-like carbon defect upon photo-

excitation of the luminescence center. The complex is destroyed by heating, providing slow recombination luminescence [12].

The small size of the stishovite single crystal made it difficult to observe the photoluminescence upon excitation with conventional discharge light sources. An attempt was made to measure the luminescence excitation spectra of a stishovite single crystal using a windowless light source with a discharge in hydrogen through a vacuum monochromator. The main measurement method was the use of the optical transparency of a stishovite single crystal. The sample was pressed into a copper holder with a hole sealed with indium. The holder also served as a shield against scattered light from the monochromator, and the glow was recorded on the other side of the excited sample. In addition to collecting light with a concave mirror, a long integration of the measuring point was carried out. The measurements were taken through a blue filter.

2. ENERGY TRANSPORT IN QUARTZ

Energy transfer spectra for an α-quartz crystal have been measured over a wide range of photon energies [4], [13].

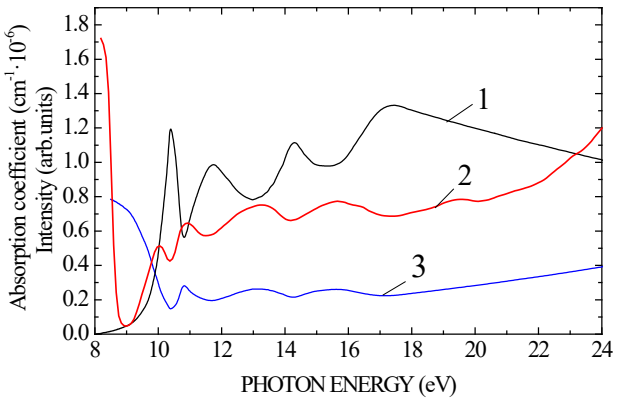

Fig. 1. The absorption spectrum of crystalline quartz – 1 calculated using *k* [13] ($\alpha=2\pi k/\lambda$, where coefficient k – extinction and λ is wavelength) and the luminescence excitation spectrum of Cu^+ centers – 2, T = 290 K. Also, the energy transfer spectrum calculated according to expression (1) – 3, which was calculated under the condition of one type of migrating quasiparticle (only one value is assumed $L = (D\tau)^{1/2}$ - 100 nm). The observed difference with the measured PLE spectrum is explained by the fact that energy transfer is carried out by many different electronic excitations [4], [14]. The point 8.5 eV is a boundary separating intrinsic absorption and intracenter absorption in quartz.

As the main effect, it was found that the luminescence excitation spectra corresponded to expression (1) when compared with the known optical absorption spectrum in the intrinsic range (Fig. 1). Here, the intrinsic absorption maxima (represented by the reflectance spectrum) correspond to minima in the measured luminescence excitation spectrum, indicating the transfer of absorbed energy. Details of interpretation can be found in [14].

3. ENERGY TRANSPORT IN STISHOVITE

The measurements of luminescence excitation spectra for stishovite single crystal were performed through blue filter.

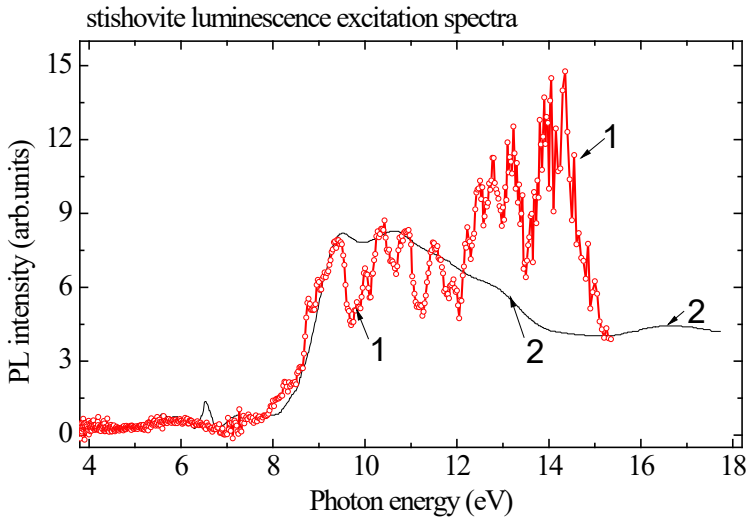

Fig. 2. Photoluminescence excitation spectra of stishovite single crystal – 1 (points connected with a line to guide eye) and spectrum of stishovite powder – 2 taken from paper [5]. The points in 1 above 12 eV are noisier because of smaller light intensity of hydrogen discharge light source in this range of spectrum.

The best result is shown in Fig. 2. There is a good agreement between the PLE spectra of a single crystal and the previously measured PLE spectra of stishovite powder [5] using radiation from a storage ring. The first minimum at 9.8 eV is present in both spectra, although in the spectrum of Ref. [5] the modulation is not so expressive. This can be explained by the migration of energy, which is better in a single crystal than in powder.

I did not consider other minima in the PLE spectrum (for example, at 10.6 and 11.9 eV), because there is no correlation with the spectrum from [5], apparently measured with much greater accuracy. Thus, we can assume the presence of a band at 9.8 eV in the intrinsic absorption spectrum of stishovite. The predicted band at 9.8 eV is possibly some analogue of the 10.5 eV band in α-quartz. However, there is still no evidence of the exciton nature of the 9.8 eV band. Other minima in the noisy spectrum measured by me require additional verification.

The mechanism of energy migration in stishovite is assumed to be realized by electron-hole pairs, since we did not find signs of excitons, for example, due to the lack of observation of a self-trapped exciton. If excitons could be created by light in stishovite, they effectively dissociated into electron-hole pairs. This is in contrast to α-quartz, where electron-hole pairs created by light have a short lifetime [15], effectively compressing to excitons, thereby providing a very efficient creation of self-trapped excitons.

4. CONCLUSIONS

The energy absorbed by a single crystal of stishovite leads to the creation of quasiparticles – electron-hole pairs, which migrate in the volume and excite defects, which are detectors of electronic excitations. The measured emission spectrum of the detectors indicates the presence of some bands in the intrinsic absorption spectrum. The intrinsic absorption band at 9.8 eV is most clearly revealed experimentally.

ACKNOWLEDGEMENTS

The financial support of the Latvian Science Council Grant No lzp-2021/1-0215 and the funding of the University of Latvia as the Centre of Excellence within the European Union's Horizon 2020 Framework Programme H2020-WIDESPREAD-01-2016-2017-TeamingPhase2 under grant agreement No. 739508, project CAMART², are greatly acknowledged.

REFERENCES

1. Zurakovsky, A. P., Gluskin, E. S., & Elango, M. A. (1979). *Fiz.Tverd.Tela (Sov.Sol.St.Phys.)* 21, 233.
2. Agranovich, V. M. (1968). Theory of Excitons. M: Nauka.
3. Zhurakovski, A. P., Trukhin, A. N., & Elango, M. A. (1980). Energy Transfer in Crystalline and Glassy Quartz Subjected to Synchrotron Radiation in the Ultrasoft X-Ray Range. *Sov. Phys. Solid State, 22* (12), 3727–3730; *Sov. Phys. Solid State, 22* (12) American Institute of Physics, (1981) 2183.
4. Trukhin, A. N. (1978). Investigation of the Photoelectric and Photoluminescent Properties of Crystalline Quartz and Vitreous Silica in Fundamental Absorption Region. Model for Electronic Structure and Migration of Energy in SiO2. *Phys. Status Sol. (b), 86*, 67–75. Trukhin, A. N. (1980). Study of Exciton in SiO2. Luminescent Centers as Exciton Detector. *Phys. Stat. Sol. (b)*, *98*, 541.
5. Paleari, A., Chiodini, N., Di Martino, D., Meinardi, F., & Fumagalli, P. (2003). Ultraviolet-Excited Radiative Decay Channels of Defect States in High-Density Sixfold-Coordinated SiO2. *Phys. Rev. B, 68*, 184107–184111.
6. Godmanis, I., Truhins, A., & Hubner, K. (1983). Exciton-Phonon Interaction in Crystalline and Vitreous SiO2. *Phys.Stat. Sol.(b), 116*, 279–288.
7. Truhins, A. N., Jansons, J. L., Dyuzheva, T. I., Lityagina, L. M., & Bendeliani, N. A. (2004). Intrinsic Absorption Edge of Stishovite and Coesite. *Sol. State Commun., 131*, 1–5.
8. Trukhin, A. N., Jansons, J. L., Dyuzheva, T. I., Lityagina, L. M., & Bendeliani, N. A. (2003). Luminescence of Different Modifications of Crystalline Silicon Dioxide: Stishovite and Coesite. *Sol. St. Commun., 127*, 415–418.
9. Trukhin, A., Kulis, P., Jansons, J., Dyuzheva, T., Lityagina, L., & Bendeliani, N. (2005). Host-Defect Luminescence of Stishovite. *Phys. Stat. Sol. (c)*, *2*, 584–587.
10. Trukhin, A. N., Jansons, J. L., Dyuzheva, T. I., Lityagina, L. M., & Bendeliani, N. A. (2008). Photoluminescence Excited by ArF and KrF Lasers and Optical Absorption of Stishovite Mono-Crystal. *J.Phys.: Condens. Matter, 20*, 175206.

11. Trukhin, A. N., Smits, K., Sharakosky, A., Chikvaidze, G., Dyuzheva, T. I., & Lityagina, L. M. (2011). Luminescence of Dense, Octahedral Structured Crystalline Silicon Dioxide (Stishovite), *J. Lumin., 131,* 2273–2278.
12. Trukhin, A., & Antuzevics, A. (2019). Photoluminescence and Electron Spin Resonance of Silicon Dioxide Crystal with Rutile Structure (Stishovite). *Physica Status Solidi (a), 215*, 1800457. https://doi.org/10.1002/pssa.201800457.
13. Lamy, P. L. (1977). Optical Constants of Crystalline and Fused Quartz in the Far Ultraviolet. *Appl. Opt., 16*, 2212–2214.
14. Trukhin, A. N. (1992). Excitons in SiO2: A Review. *J. Non-Cryst. Sol., 149*, 32–45.
15. Martin, P., Guizard, S., Daguzan, Ph., Petite, G., D'Oliveira, P., Meynadier, P., & Perdrix, M. (1997). Subpicosecond Study of Carrier Trapping Dynamics in Wide-Band-Gap Crystals. *Phys.Rev. B, 55*, 5799.

sciendo

LATVIAN JOURNAL OF PHYSICS
AND TECHNICAL SCIENCES
2022, N 4

DOI: 10.2478/lpts-2022-0031

ANALYSIS OF TEST RESULTS OF THE DEVELOPED SYNCHRONOUS RELUCTANCE MOTOR FOR PUBLIC TRANSPORT APPLICATION

K. Gulbis[1*], U. Brakanskis[1], E. Kamolins[1],
M. Gorobecs[1], A. Potapovs[1], K. Sejejs[1], J. Zarembo[2],
V. Burenin[2]

[1]Riga Technical University
6A Kīpsalas Str., Riga, LV-1048, LATVIA
[2]JSC Riga Electric Machine Building Works
53 Ganību dambis, Riga, LV-1005, LATVIA
*e-mail: Karlis.gulbis_1@rtu.lv

The paper describes the design and control method of the synchronous reluctance machine with improved efficiency compared to traction induction motor for electric vehicle application.

Magnetic field finite element modelling is used in the design process. The paper presents load characteristics calculation method for the design process, considering the cross magnetic saturation effect. Control algorithm with constant d-axis current control method is developed in the research. The prototype of the machine is constructed and tested.

Keywords*: Design optimization, electric traction, finite-element method, synchronous reluctance machine (synrm), test bench.*

1. INTRODUCTION

Many motor types have been used for electrical vehicles, but in current production permanent magnet motor is dominant. There is a basis for considering synchronous reluctance motor (SynRM) as a suitable candidate for grid-connected electrical vehicle applications such as trams, trolleybuses, metro and trains. SynRM can

substitute traction induction motor (IM) and permanent magnet synchronous motor (PMSM) in these applications in new construction projects or for retrofit projects.

Simple and reliable construction with lower production costs is SynRM advantage compared to PMSM [1]. PMSMs, especially interior permanent magnet synchronous motors with commonly used high-performance neodymium permanent magnets, have property that demagnetization occurs at a high temperature or by a reverse magnetic field. Motors for electrical vehicle application typically are of enclosed type and are characterised by high-temperature rise [2], [3]. SynRM has the potential of equal or higher efficiency compared to IM due to no electrical losses in rotor [1], [4].

For battery electrical vehicles higher efficiency that can be achieved by PMSM machine compared to SynRM will be of greater importance compared to grid-connected electrical vehicle applications. However, there is plenty of research where SynRM has been suggested for battery traction vehicles [5]–[7].

The goal of the research is to design SynRM with the efficiency of at least 95 % that will replace IM with the efficiency of 92.6 % for mass transit electrical vehicle application. The designed SynRM had to retain the same sizing and power supply requirements as the IM.

For a wide range of applications, SynRMs in combination with a frequency converter are produced by several major electrical machine manufacturers [8], [9]. There has been a wide range of studies that deal with problems and design aspects of SynRM [10]–[13].

In this study, the layout of rotor flux barriers described in [10] was used as a basis, and an approximate size of flux barriers was chosen according to [11]. The designed SynRM rotor has salient poles without active elements (windings and permanent magnets) in the rotor.

The designed reluctance machine is intended to operate in the motor mode. The electromagnetic torque of the SynRM increases when the difference between impedances of the rotor direct axis and quadrature axis (magnetic asymmetry of the machine) increases (1).

$$T_{em} = \frac{3V_1^2}{2\Omega} \cdot \left(\frac{1}{X_{aq}} - \frac{1}{X_{ad}}\right) \cdot \sin(2\theta), \qquad (1)$$

where θ – torque angle;
V_1 – supply voltage;
Ω – angular speed;
x_{ad} – armature direct axis field impedance;
x_{aq} – armature quadrature axis field impedance.

2. DESIGN OF SYNRM STATOR AND ROTOR

2.1. The Main Parameters and Design Limitations Set by Project Specification

SynRM was developed to replace IM; therefore, casing size (stator outer diameter D_{os}, stator stack length L and shaft diameter D_{sh}), electrical supply parameters (V, I, f), mechanical parameters (T, n) and construction possibilities of the manufacturer (airgap width δ) had to be considered. Set parameters are compiled in Table 1.

Table 1. The Main Parameters of the Developed SynRM

P_N	180	kW	Rated mechanical power
V_{N1}	420	V	Rated supply line voltage
f_1	50	Hz	Rated supply frequency
n_1	1500	min^{-1}	Rated rotational speed
2p	4		Number of poles
m	3		Number of phases
T_N	1146	N*m	Rated mechanical torque
D_{os}	493	mm	Stator outer diameter
L	290	mm	Stator stack length
δ	1,2	mm	Airgap width

2.2. SynRM Stator Design

The stator was designed by performing calculations described in [14]–[17] with the addition of mathematical modelling of the magnetic field using the finite element modelling method (FEM). For stator parameter optimization, FEM was performed by solving a magnetostatic model with defined three-phase currents in windings. Computations were done for a non-linear model with electrotechnical steel SURA M470-50HP described by B(H) curve. The electrotechnical steel SURA M470-50HP was also used for the manufactured prototype. The fundamental harmonic of the induction in the middle of the air gap B_{1m} was obtained using FEM software subroutine. For computations, typical FEM methods were used for which there is an abundance of literature. Park transformations were used for transition from the three-phase parameters to the direct and quadrature axial parameters.

Parameter optimal value was found by searching for a maximum value of the magnetic asymmetry that was determined from the impedance of the direct and quadrature axis (ratio 2). High electromagnetic torque will be ensured if the magnetic asymmetry is high (1). In this research, winding leakage impedances were assumed to be equal for both components. Direct and quadrature axis field impedances are calculated using (3) and (4). To reduce computation and calculation time at this design stage, magnetic cross saturation was not considered, the effect would be similar for all the considered designs, values were used only for optimization purpose. and values considering magnetic cross saturation are calculated at a later design stage.

$$K_{d/q} = \frac{X_{ad}}{X_{aq}}, \tag{2}$$

$$X_{ad} = \frac{\pi \cdot \sqrt{2} \cdot f \cdot w_1 \cdot k_{w1} \cdot \Phi_{ad1}}{I_d}, \tag{3}$$

$$X_{aq} = \frac{\pi \cdot \sqrt{2} \cdot f \cdot w_1 \cdot k_{w1} \cdot \Phi_{aq1}}{I_q}, \tag{4}$$

where $K_{d/q}$ – magnetic asymmetry coefficient;
X_{ad} – armature winding direct axis field impedance;
X_{aq} – armature quadrature axis field impedance;
Φ_{ad1} – amplitude of direct axis armature magnetic flux fundamental harmonic;
Φ_{aq1} – amplitude of quadrature axis armature magnetic flux fundamental harmonic;
I_d – direct axis current component;
I_q – quadrature axis current component.

Stator parameters for which maximum values of the magnetic asymmetry were determined were inner stator diameter and stator sloth width. Inner stator diameter and stator sloth width were used because it was found that these parameters of all stator parameters, with set design limitations, had the most significant influence on magnetic asymmetry. Optimisation for parameters was done separately to reduce the complexity of the problem but few iterations were used to ensure compliance with each other.

An optimal inner stator diameter value (Fig. 1a) was determined by keeping unchanged: 1) stator slot total area, 2) airgap width and 3) rotor development principles (rotor development principles are explained in the section about the rotor). Variables that are changed with inner stator diameter are 1) yoke height and 2) tooth width.

An optimal stator slot and tooth width value (Fig. 1b) was determined by keeping unchanged: 1) stator slot and tooth combined (section) width; 2) stator slot area; 3) airgap and 4) rotor development principles. Variables that are changed are 1) tooth and slot width; 2) slot height. In the computations using the finite element analysis (FEA), slot and tooth shapes are simplified, without considering wedge shape and rounding, which mainly increase magnetic losses, but the impact of the values on impedance is negligible, and therefore these elements are not binding at this stage.

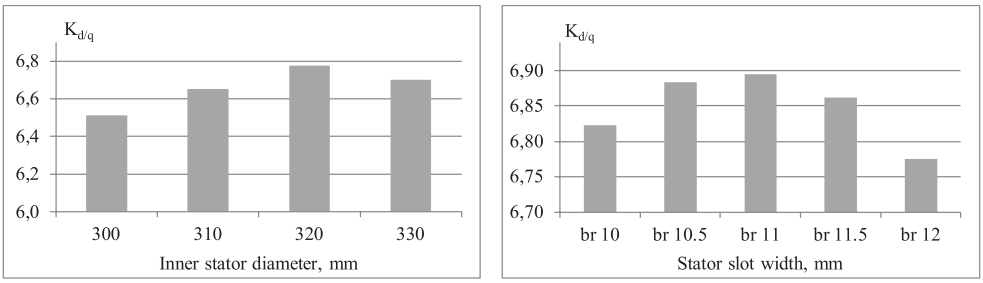

Fig. 1. $K_{d/q}$ at different inner stator diameter sizes (a), stator slot sizes (b).

2.3. SynRM Rotor Design

The rotor was designed by FEM magnetic field modelling for various rotor models. Important parameters were chosen from recommendations in the literature. The number of flux barriers and their positioning were chosen by the method described in [10]. The width of the rotor barriers and flux paths were chosen from recommendations in [11]. Arch and trapezoid types of flux barriers were considered. Designed rotor with the main geometrical parameters is presented in Fig. 2.

According to the recommendations [10], the lowest torque oscillations will be for the design with the number of rotor flux barriers N_{rot} adjusted to the number of stator slots N_{stat} and stator sloths per pole per phase q, with suggested relationship $N_{rot} = N_{stat} \pm 2q$. For design rotor with 48 stator slots $N_{rot} = N_{stat} - 2q = 40$ was chosen. The rotor with $N_{rot} = 56$ provided similar magnetic asymmetry and torque ripple

but the complexity of rotor was greater.

According to the recommendations [11], optimal magnetic asymmetry will be for the design with a flux path width to flux barrier width ratio close to 2:1. FEM simulations showed similar results and flux path width 16 mm and flux barrier width 8 mm were used. Deviation from ratio with increased flux path width was characterised by a reduction in magnetic asymmetry, but the reduced flux path width was characterised by increased torque oscillations.

FEM simulations show that flux barrier shape minimally influences effective torque because the widths of the rotor barriers were equal for both designs and magnetic asymmetry was equal for different shapes but the effect on torque ripple was noticeable. For two shapes considered, arch flux barriers had lower torque ripple. Arch-shaped flux barriers had a common centre located on q-axis with different arch centres considered but 1.35–1.45 r_{rot} provided the best results. Arch-shaped flux barriers have constant flux path width that ensures equal flux path saturation but trapezoid-shaped barriers at incline points will have more saturated regions. FEM results were: for arch-shaped design $T_{max}/T_{min} = 1362/1094\ Nm$ with $T_{ripple} = 22\ \%$, but for trapezoid-shaped design $T_{max}/T_{min} = 1378/1064\ Nm$ with $T_{ripple} = 26\ \%$.

To guarantee the mechanical strength of the rotor it is necessary to create bridges – sections of steel left to physically connect adjacent flux paths across the flux barriers. Bridges reduce magnetic asymmetry by forming a path for quadrature axis flux but they are essential for the structural integrity of the rotor. For designed machine bridges reduce the maximum torque by 7 %. Bridge designs that reduce maximum torque loss have been proposed [18], [19], but they increase manufacturing complexity and their structural integrity is questionable. To reduce torque ripple, flux barriers next to the air gap should be rounded. Rounding of flux barriers had no substantial influence on effective torque. For the designed machine, a radius of 7 mm and 4 mm was considered. Rounding of flux barrier with 7 mm radius had 2 % lower torque ripple compared to the radius of 4 mm.

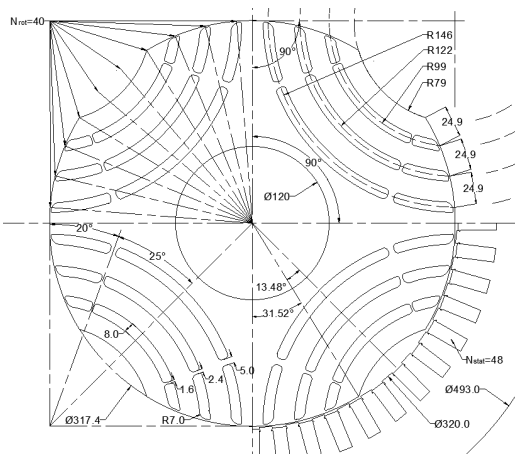

Fig. 2. Geometric parameters.

3. CALCULATION OF LOAD CHARACTERISTICS

During the design stage of SynRM parameters and characteristics, armature reactances x_{ad}, x_{aq}, torque as a function of load angle $T = f(\theta)$ and efficiency η were calculated. To acquire the correct parameters, a designer has to create a precise mathematical model as incorrect results can lead to project suspension at the design stage, overly optimistic conclusions and incorrect choice of the machine control algorithm.

The operating characteristics of SynRM: $T_2 = f(\theta)$; $I, \eta, \cos\varphi = f(P_2)$ rely on the correct calculation of the armature direct axis reactance x_{ad} and the armature

quadrature axis reactance x_{aq}. For correct x_{ad} and x_{aq} calculation, cross magnetic saturation has to be considered. It is complicated to consider magnetic cross saturation at the motor design stage because it is difficult to create FEM mathematical model with which x_{ad} and x_{aq} can be correctly expressed as functions from current *I*. Reactances can be expressed as functions of respective current component I_d and I_q, by modelling the magnetization curve $\Phi = f(F_{mag})$ for the direct and quadrature axes separately, but, in this case, the cross magnetization – effect of I_q current on x_{ad} and the effect of I_d current on x_{aq} – is not considered. To account for cross magnetic saturation effect, load characteristic calculations are performed implementing the algorithm described in [20] where step-by-step explanations are given.

The algorithm includes a numerical calculation part (Steps 1, 3, 4 and 5) and a FEM part (Step 2) (Fig. 3). FEM is performed by defining three-phase currents in winding and solving magnetostatics model similarly as described in previous parts.

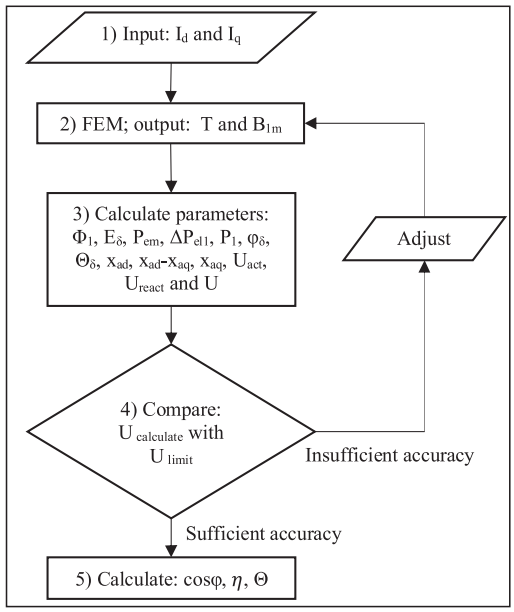

Fig. 3. Algorithm flow chart.

4. IMPLEMENTED CONTROL ALGORITHMS FOR SYNRM

Synchronous reluctance motor has different control strategies. More common ways to control are:

- Constant d-axis current control (CDAC);
- Maximum torque per ampere control (MTPA);
- Maximum power factor control (MPFC);
- Maximum efficiency control (ME).

Use of these control strategies varies from application to application and has its own advantages in certain scenarios. In general, before the field-weakening regime, any of the control strategies could be used. However, during the field-weakening regime, when the motor hits the voltage limitation, it must remain inside the voltage boundaries; thus, this is a priority. Mainly the level of the voltage is kept by maintaining the d-axis current component, and field-weakening approach of $1/v$ is used to keep the voltage in limit.

$$i_d = i_{d\,nominal} \cdot \frac{n_{nominal}}{n_{feedback}}. \quad (5)$$

Each of the control strategies has to achieve specific torque reference, but at different current angles θ. As stated in theoretical background regarding control of the SynRM, each of the strategies has different purpose.

Setting of the currents could be narrowed down to the setting of only current i_d, while current i_q is derived based on refer-

ence torque from the speed controller and current i_d. The derivation is based on Eq. (6).

$$i_q = \frac{T}{3/2 \cdot p \cdot (L_d - L_q) \cdot i_d}. \quad (6)$$

The algorithm approach in a block scheme is shown below, where "current law" is represented in the equation above (Fig. 4).

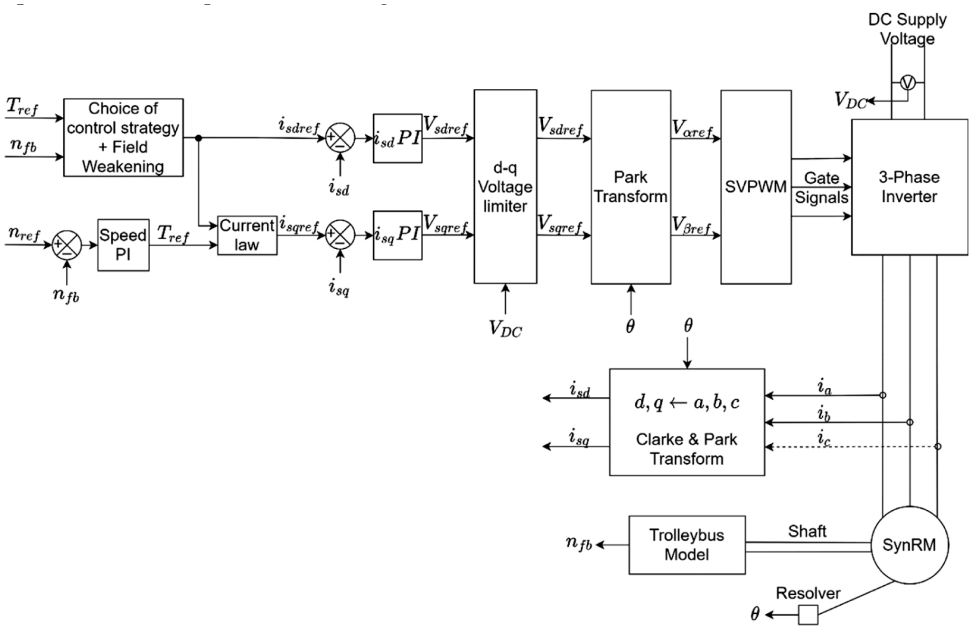

Fig. 4. Control structure of SynRM control with a trolleybus model.

Selection of the control strategy and usage of field-weakening regime are done in the corresponding block. For the Simulink implementation, MATLAB function block is used. It allows for more versatile implementation of a complex algorithm.

MTPA, ME and MPFC need to follow a specific current angle trajectory to achieve reference torque with corresponding requirements. Due to saturation and iron loss, current angle is not a constant and varies with torque reference.

From the laboratory testing $L_d = f(i_d, i_q)$ and $L_q = f(i_d, i_q)$ values were obtained, and they are represented as a lookup table.

To achieve reference torque value, only one combination of i_d and i_q exists for each of the strategies. Therefore, based on laboratory testing results, each of the combinations could be found by calculation. Several dozens of current combinations are found off-line once, prior to simulation, for each of the control strategies. After that, using the curve fitting tool, 4th order polynomial function is obtained as an approximation of each control strategy. The below function represents the general view of the approximation (7). This approach is based on the research [21].

$$i_d^* = p_1 \cdot T_{ref}^4 + p_2 \cdot T_{ref}^3 + p_3 \cdot T_{ref}^2 + p_4 \cdot T_{ref} + T_{ref}. \quad (7)$$

For MTPA coefficients are: p_1=−1.123; p_2=2.87; p_3=−2.667; p_4=1.51. For MPFC coefficients are: p_1=−0.6011; p_2=1.619; p_3=−1.442; p_4=0.9364. All of the coefficients are with 95 % confidence bounds.

For the approximation, per-unit values of current and torque are used because the model is based on the per-unit values.

Below is displayed d-axis current as a function of reference torque for the MTPA strategy (Fig. 5). One is based on laboratory testing and calculation, and the other is curve fitted approximation, with coefficients as shown above.

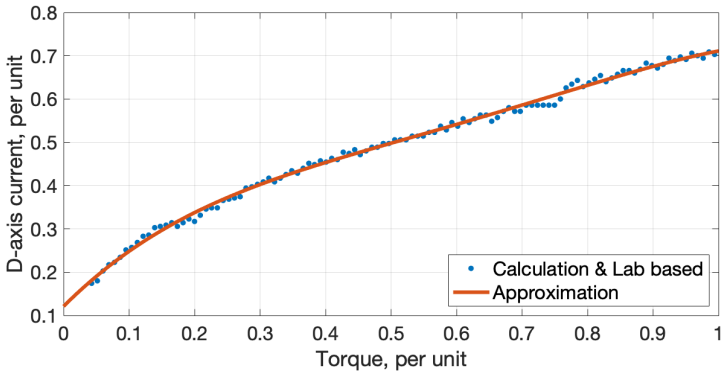

Fig. 5. Direct axis current I^*_d=f(T_{ref}) for MTPA.

Before start of the simulation process, the desired algorithm is chosen via the supplied constant (1–4 for CDAC, MTPA, ME and MPFC, respectively). After that reference current before the field-weakening regime is chosen based on 4th order polynomial approximation or a constant value, while during the field-weakening regime reference d-axis current is selected as previously mentioned.

Start of the field-weakening is based not only on the feedback speed, but also on the voltage limitation. In this case, for each of the control strategies, maximum torque traction characteristic is calculated for above nominal speeds, based on laboratory testing, and approximated using rational-1,1 approach, based on the general expression (8).

$$T_{max} = \frac{p_1 \cdot n + p_2}{n + q_1}. \quad (8)$$

For MTPA coefficients are: $p_1 = -0.08423; p_2 = 0.2507; q_1 = -0.7131$. For MPFC coefficients are: $p_1 = -0.1791$; $p_2 = 0.6121$; $q_1 = -0.5682$. All of the coefficients are with 95 % confidence bounds.

For MPFC nominal speed coincides with CDAC, and is 1500 RPM; in other words, it reaches 420 V limit at that point with the nominal torque of 1145.8 Nm. For MTPA it is 1332 RPM, and for ME it is 1400 RPM, meaning that at those speeds it reaches 420 V, and needs to lower torque to remain at 420 V. Maximum torque, at which motor can follow the control strategy is found from nominal speed till the maximum of 3288 RPM. As with the $i_d^* = f(T_{ref})$, the obtained values are curve fitted to obtain the approximation function, based on the above-mentioned general function.

Such complication for field-weakening regime is needed because during the operation of the motor above nominal speeds, voltage limit is reached only at specific values of the torque. It is important as electric motor commonly operates inside its limiting traction characteristic.

Algorithm takes reference torque and

feedback speed to set the $i_{d_{ref}}$ for each of the regimes, both before and in field-weakening regime.

0) Regime operation is selected at initialisation stage.

1) Maximum torque during chosen regime is defined for current speed: IF speed is below nominal, THEN torque is 1 p.u., ELSE based on $T_{max} = f(n)$ approximation.

2) current is selected: IF speed is below nominal AND reference torque is less than maximum torque, THEN i_d is chosen based on $i_d^* = f(T_{ref})$ approximation, ELSE field-weakening regime.

For CDAC it is a bit different: IF speed is below nominal, THEN $i_d = const.$, ELSE field-weakening regime.

5. COMPUTED, CALCULATED AND EXPERIMENTAL RESULTS

5.1. Magnetic Field Data

Induction distribution in the stator and the rotor magnetic steel (Fig. 6) shows that the machine at load close to the rated is saturated with induction at stator teeth reaching up to 2 T and at the stator yoke reaching up to 1.6 T. Induction in the rotor is distributed evenly as a result of all the considerations implemented at the rotor design stage. It is evident that mechanical strength connections – bridges, get saturated. In the flux carriers, there are no regions with increased magnetic saturation. Increased magnetic saturation is noticeable at bridges and next to the air gap where increased magnetic saturation was expected.

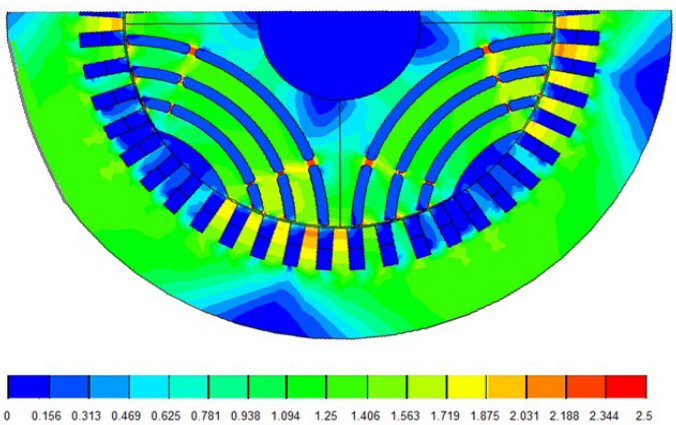

Fig. 6. Magnetic field of the developed SynRM, induction distribution (T), load above the rated: U_{LL}=420V; I=392 A; f=50 Hz; n=1500 min^{-1}.

5.2. Experimental Setup

The experimental setup consists of designed 180 kW SynRM (rotor assembly is shown in Fig. 7a), load 180 kW induction motor, torque and speed meter mounted on shaft between SynRM and load IM (Fig. 7b). SynRM was driven by a custom-

made laboratory frequency converter with constant d-axis current control (CDAC) method. Frequency converter was used for the control of load IM. Electrical parameters were measured by Yokogawa Power Analyser WT-1800. Torque and speed were measured by HBM T40B torque flange.

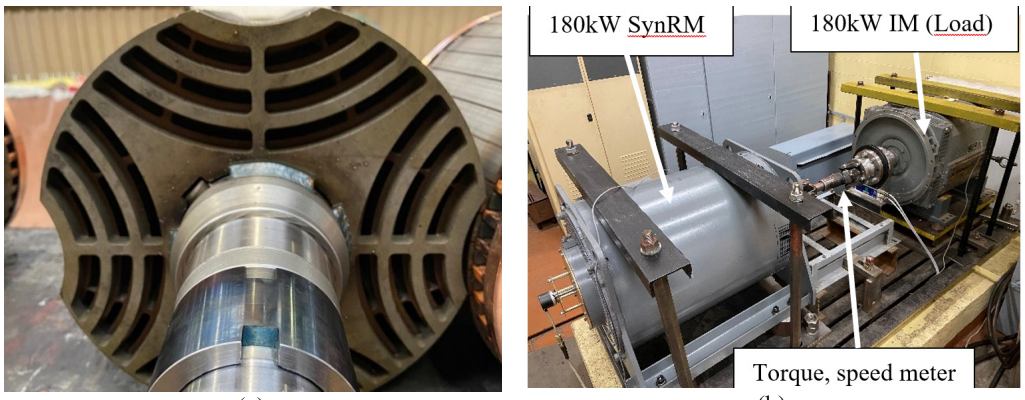

(a) (b)

Fig. 7. Designed SynRM rotor (a), SynRM test bench (b).

5.3. Inductances

For the direct and quadrature axis inductances, comparison between calculated inductances at the design stage and measured inductances is shown in Fig 8. Inductances are displayed as a function from total current I_1 with changing load (from no load to load above rated), constant frequency 50 Hz and constant voltage 420 V (changing i_q and constant i_d). The calculated inductances at the design stage are direct and quadrature axis armature inductances without leakage inductance but measured direct and quadrature axis inductances include leakage inductances. Leakage inductance (0.15 mH) comprises a small fraction of total inductance. The significant mismatch between calculated and measured results is at low current values where calculated quadrature axis inductance rises exponentially but the measured value reduces.

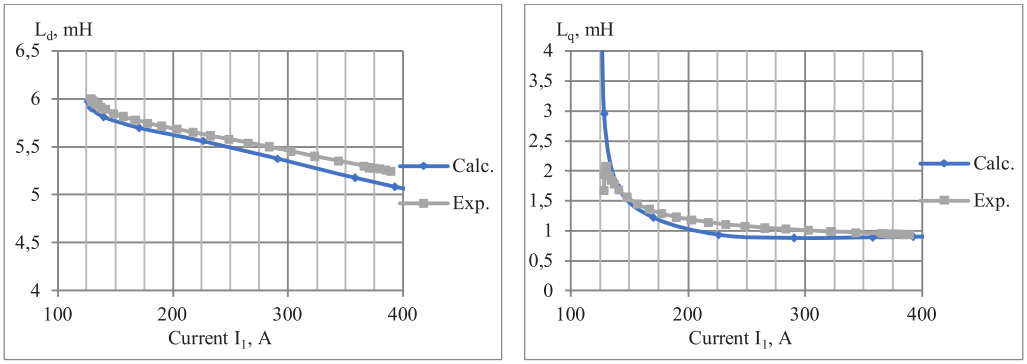

(a) (b)

Fig. 8. Direct axis inductance (a), Quadrature axis inductance (b) as a function from current.

5.4. Loss, Efficiency and Load Curves

Measured and designed parameters are reported in Table 2, additionally for comparison IM parameters are displayed. Losses and efficiency were calculated according to IEC 60034-2-1:2014 “Standard methods for determining losses and efficiency from tests”, with exception of additional loss. Efficiency was determined by direct measurement method. To evaluate the design process, losses were split into their components. Winding loses were calculated from stator winding resistance at 75° C, iron and mechanical loses were calculated from the no-load experiment. In the reported data, additional load losses include frequency converter supply related losses, harmonic losses introduced by voltage waveform of the frequency converter. Reported values are at a constant 50 Hz frequency.

Table 2. SynRM Parameters

Parameter	**Unit**	**Design**	**Measured**	**IM**
Supply current (I_1)	A	392.4	374.2	310
Supply voltage (V_1)	V	420.0	417.0	420
Power factor (cosφ)		0.663	0.699	0,89
Supply power (P_1)	kW	189.2	188.8	201
Mechanical power (P_2)	kW	179.2	179.4	186
Mechanical torque (T_2)	Nm	1 141	1 144	1 193
Winding losses ($\Delta P_{el1\,N}$)	W	5 637	4 904	6 740
Rotor winding losses ($\Delta P_{el2\,N}$)	W	-	-	2 170
Iron losses ($\Delta P_{mag\,N}$)	W	2 873	2 853	3 680
Mechanical losses ($\Delta P_{mech\,N}$)	W	544	816	470
Additional load losses ($\Delta P_{add\,N}$)	W	1 002	857	1 033
Total losses (ΔP_{Σ})	W	10 056	9 430	14 093
Efficiency (η)	%	94.69 %	95.01%	92.6%

Achieved efficiency is reported in Fig. 9a. 95 % efficiency has been reached for loads from 122 kW to 180 kW with maximum efficiency of 95.15 % at 150 kW. Higher efficiency compared to IM is reached due to considerably lower electrical loses. Stator outer diameter or stack length has to be increased for further SynRM efficiency improvement.

Current and voltage as a function from load power show compatibility between calculated and measured results (Fig. 10a). Measured voltage slightly differs from the calculated one. For experiments, voltage was not kept constant, characteristics were measured by adjusting only quadrature axis current with no regulation to direct axis current to account for voltage deviation from rated, but calculated characteristics were produced by changing direct axis and quadrature axis currents until the rated voltage was reached.

SynRM power factor (0.699) (Fig. 9b) is low compared to IM (0.89); consequently, current is higher. When designing SynRM, trade-off between power factor and torque capacity is unavoidable. The primary goal of the research was to obtain required torque and efficiency reducing possibility for power factor optimization.

Mechanical torque is reported in Fig. 10b. At rated voltage, SynRM is with low overload capabilities and if overloading is necessary voltage has to be increased. The increased voltage will reduce efficiency.

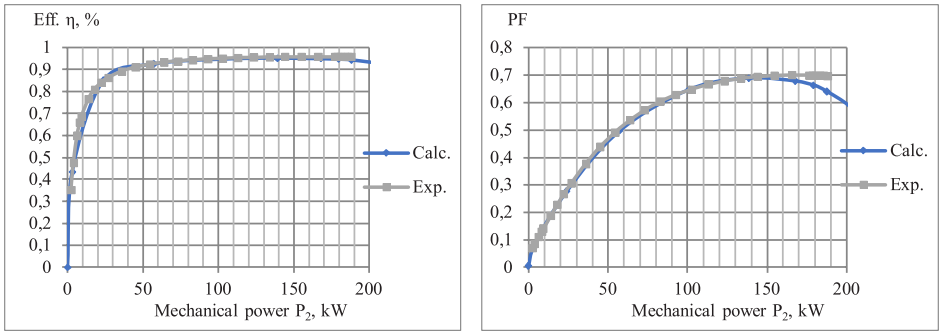

(a) (b)

Fig. 9. Efficiency (a), power coefficient (b) as function from load power.

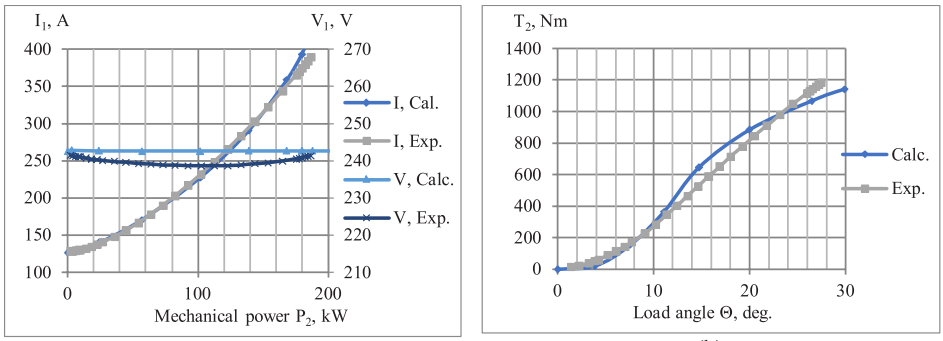

(a) (b)

Fig. 10. Current and voltage from load power (a), Mechanical torque from load angle (b).

Different abovementioned control methods have been simulated for a trolleybus route defined by velocity dynamics function as a reference. All control algorithms obtain a similar ability to maintain predefined speed, perform acceleration and produce an output torque (Fig. 11).

However, the difference in control methods is represented by internal power factor (Fig. 12) and voltage and current (Fig. 13) in different regimes.

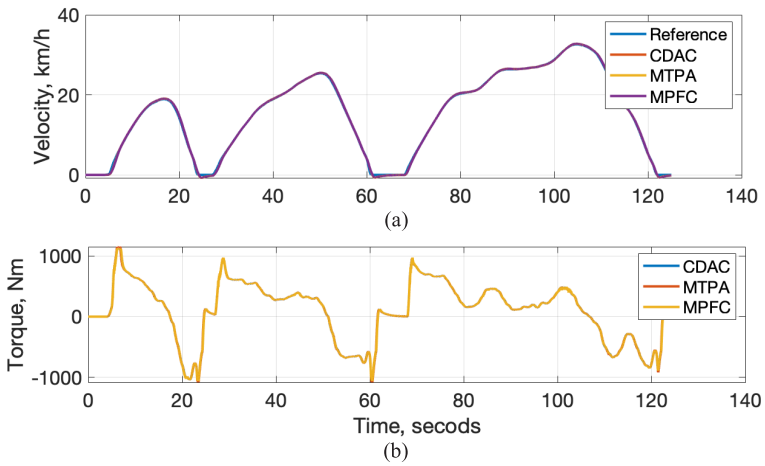

Fig. 11. Speed (a), Mechanical torque (b) from time in (s) in different regimes.

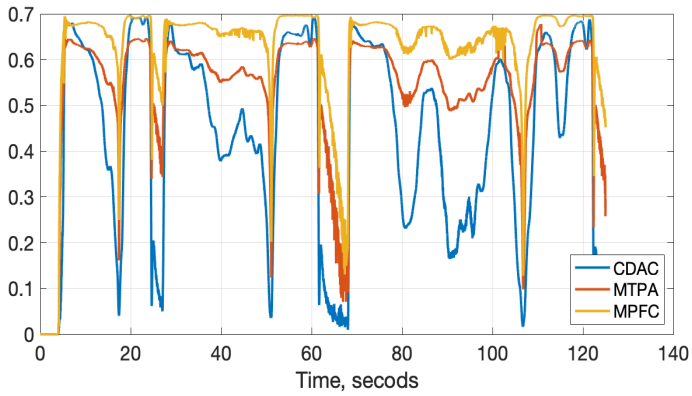

Fig. 12. Internal power factor from time in (s) in different regimes.

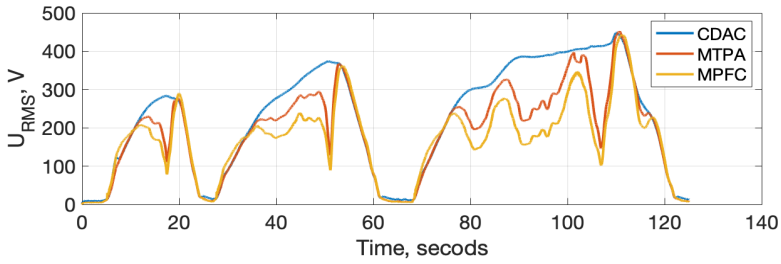

(a)

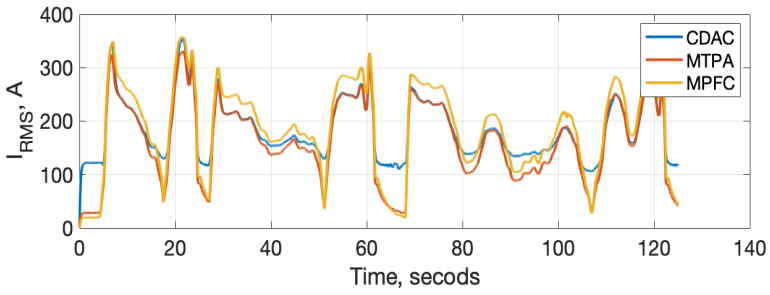

(b)

Fig. 13. RMS voltage (a), RMS current (b) from time in (s) in different regimes.

5.5. Comparison of SynRM and IM

The main goal of optimizing the design of synchronous-reluctance motor (6SynRM.001 Y2) was to increase efficiency while maintaining the required nominal torque. Laboratory testing of SynRM showed (Fig. 14a) that the electric motor provided the required nominal torque up to a nominal speed of 1,500 RPM and did not meet the requirements in the field-weakening regime (above nominal speed). The margin of the maximum torque at nominal voltage is about 15 %.

In traction mode, the electric motor must have a 1.5 times torque margin and have a minimum of 10 % reserve in the field-weakening mode to ensure all of the dynamic characteristics of the vehicle. It is also necessary to consider that the trolley-

bus uses an overhead line network, where low voltage regimes of operation are possible. The reduced voltage directly affects the maximum torque margin, which in the case of the synchronous-reluctance motor would significantly reduce its traction characteristic.

For comparison, Fig. 14b shows the nominal and theoretical maximum traction characteristics of the induction motor (6DTA.002.1 Y2). It can be seen that the maximum torque is significantly higher than the maximum torque of SynRM. In addition, in the field-weakening regime, the induction motor is able to provide the required torque, with a 50 % reserve at the maximum required speed.

The next step is comparison of efficiency indicators of motors. Measured values are shown in Fig. 15a. It can be seen that the stated goal of high efficiency in comparison with IM is achieved at all speeds, and is much less prone to change. For numerical comparison, at the nominal point, efficiencies are equal to: $\eta_{SynRM} = 94.82\ \%$, and $\eta_{IM} = 92.70\ \%$.

High efficiency results in lower losses, leading to lower cooling requirements and lower temperatures during operation. This advantage can allow for longer regimes of operation.

As can be seen from the graph in Fig. 15b $\cos\phi$ in SynRM is significantly inferior to IM. Power factor of 6SynRM.001 Y2 is $\cos\phi = 0.67 - 0.7$, and of 6DTA.002.1 Y2 is $\cos\phi = 0.85 - 0.9$. This difference is based on the physical properties of the machine, and a lower power factor was expected at the design stage from a theoretical calculation.

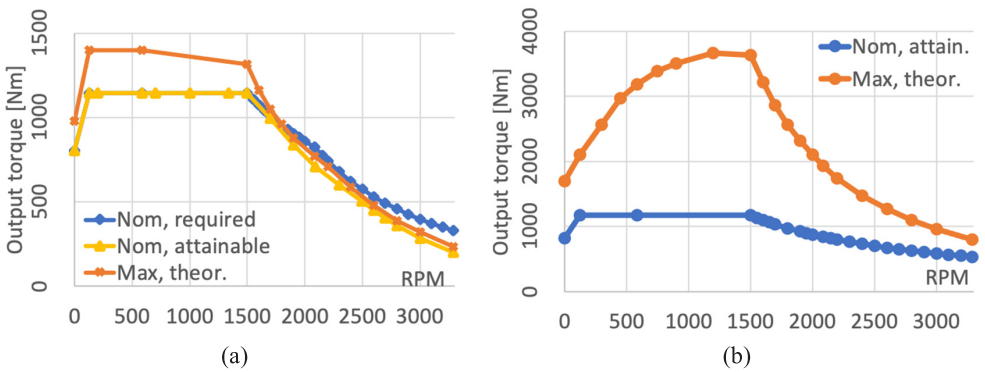

Fig. 14. Traction characteristic of SynRM (a), IM (b).

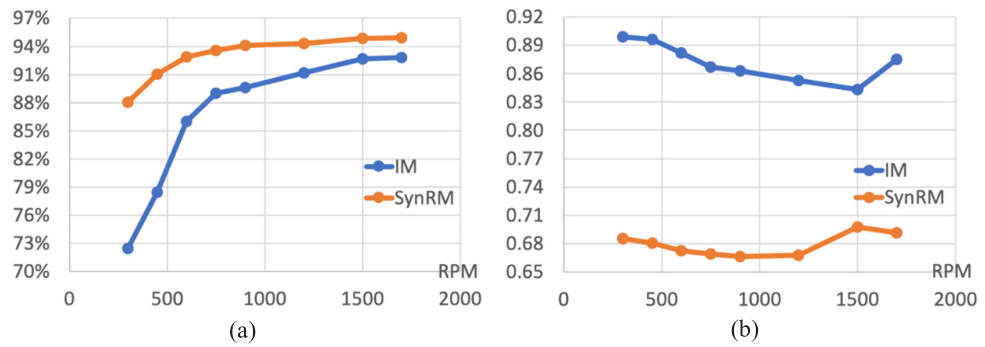

Fig. 15. SynRM and IM efficiency (a), power factor (b).

6. CONCLUSIONS

The design of the synchronous reluctance motor with the improved efficiency compared to induction motor has been completed and the performance has been modelled and experimentally verified. SynRM with the efficiency of 95 % for load range from 120 kW to 180 kW has been developed. The project goal of increasing efficiency, compared to the traction induction machine of 92.6 % while retaining machine sizing and supply parameters, has been achieved. SynRM with reduced winding and iron losses compared to the traction induction machine has been developed. SynRM parameter calculation method implementing magnetic field finite element modelling has been validated by the test results.

After laboratory tests and comparative analysis, it can be concluded that the main advantage of the developed and produced synchronous-reluctance motor, compared to the induction motor, is efficiency. The efficiency of the developed motor is high and almost constant, not only at and near the nominal point, but also in other regimes of operation.

In turn, the desire to increase efficiency negatively affects the torque margin of the SynRM. To ensure the required torque, it is necessary to raise the magnetic induction in the iron, relative to the induction of the IM, which is the main way of forming the torque in the SynRM. As a result, the SynRM provides the required torque up to nominal speed, but fails to meet the additional requirements for the traction application of electric motors. Insufficient torque margin will degrade the dynamic performance of the vehicle in operation.

During the design process, optimization options for this type of electric motor have been tested to increase the pull-out torque. The following relationships have been established: an increase in magnetic flux by 1.25 times increases the pull-out torque by 1.29 times, while the iron loss increases by 1.84 times. This example shows that an increase in the pull-out torque leads to a significant decrease in efficiency (increase in steel losses and in copper losses), but this is one of the main advantages of this type of electric motor.

Low power factor is a disadvantage of SynRM. The power factor does not affect the performance or efficiency of the motor, but requires more current on the stator windings. As a result, it leads to increased losses in the frequency converter, as well as increases the requirements for the maximum current of the electric drive system. The disadvantage may be less important if the rest of the electric drive equipment has high efficiency.

This motor is well suited for industrial use case with a relatively smooth change of torque and speed, where the efficiency (losses) and the ability to work in long or even continuous regimes without overheating play a key role. Another example of use may be electric vehicles, where the first requirement is reliability, and the mass of the electric motor plays a secondary role.

ACKNOWLEDGEMENTS

The paper is based on the research that has been conducted in the framework of the project No1.1.1.1/18/A/055 “Development of a New Generation Synchronous Reluctance Electrical Motor” funded by the ERDF.

REFERENCES

1. Moghaddam, R. R., Nategh, S., Islam, J., & Boglietti, A. (2020). Different traction motor topologies used in e-mobility: Part II: Magnet-based solutions. In *2020 International Conference on Electrical Machines (ICEM), (pp. 138–143)*. 23 August 2020, Gothenburg.
2. Hamidizadeh, S., Alatawneh, N., Chromik, R. R., & Lowther, D. A. (2016). Comparison of Different Demagnetization Models of Permanent Magnet in Machines for Electric Vehicle Application. *IEEE Transactions on Magnetics*, *52* (5), 1 –4.
3. Jeong, G., Kim, H., & Lee, J. (2020). A Study on the Design of IPMSM for Reliability of Demagnetization Characteristics-Based Rotor. *IEEE Transactions on Applied Superconductivity*, *30* (4), 1–5.
4. de Pancorbo, S. M., Ugalde, G., Poza, J., & Egea, A. (2015). Comparative study between induction motor and Synchronous Reluctance Motor for electrical railway traction applications. In *2015 5th International Electric Drives Production Conference (EDPC)*, (1560040). 15–16 September 2015, Nuremberg, Germany.
5. Jurca, F. N., Mircea, R., Martis, C., Martis, R., & Florin, P. P. (2014). Synchronous reluctance motors for small electric traction vehicle. In *2014 International Conference and Exposition on Electrical and Power Engineering (EPE)*, (pp. 1–5). 4 December 2014, Iasi.
6. Jurca, F. N., Ruba, M., & Marţiş, C. (2016). Design and control of synchronous reluctances motors for electric traction vehicle. In *2016 International Symposium on Power Electronics, Electrical Drives, Automation and Motion (SPEEDAM)*. 22–24 June 2016, Capri, Italy.
7. Riley, C. P., Bedford, A. M., Topping, P. J., Reeve, J. M., Wale, J. D., Venskus, A. … & Ilea, D. (2014). Simulation based design of reluctance motors for traction applications in hybrid and electric vehicles. In *7th IET International Conference on Power Electronics, Machines and Drives (PEMD 2014)*. 4 August 2014, Manchester.
8. ABB. (2019). *Low Voltage IE5 Synchronous Reluctance Motors.* Available at http://new.abb.com
9. SIEMENS AG. (2019). *SIMOTICS Reluctance Motor with SINAMICS Frequency Converters*. Available at http://www.industry.siemens.com
10. Vagati, A., Pastorelli, M., Franceschini, G., & Petrache, S.C. (1998). Design of Low-Torque-Ripple Synchronous Reluctance Motors. *IEEE Transactions on Industry Applications*, *34* (4), 758–765.
11. Lipo, T. A., & Matsuo, T. (1994). Rotor Design Optimization of Synchronous Reluctance Machine. *IEEE Transaction on Energy Conversion*, *9* (2), 359–365.
12. Orlova, S., Vezzini, A., & Pugachov, V. (2015). Analysis of parameters for optimal design of synchronous reluctance motor. In *56th International Scientific Conference on Power and Electrical Engineering of Riga Technical University (RTUCON)*. 14 October 2015, Riga, Latvia. doi:10.1109/RTUCON.2015.7343178
13. Orlova, S., Pugachov, V., Rassõlkin, A., Kallaste, A., & Vaimann, T. (2019). Design of rotors for synchronous reluctance motor: Analytical treatment and optimization. In *21st European Conference on Power Electronics and Applications (EPE ‹19 ECCE Europe), (pp. 1–9)*. 3–5 September 2019, Genova, Italy.
14. Boldea, I. (1996). *Reluctance Synchronous Machines and Drives*. Oxford: Clarendon Press.
15. Boldea, I., & Nasar, S. A. (2009). *The Induction Machines Design Handbook* (2nd ed.). USA: CRC Press.
16. Pyrhonen, J., Jokinen T., & Hrabovcova V. (2008). *Design of Rotating Electrical Machines*. John Wiley & Sons.
17. Копылов, И.П. (1986). Электрических машины. М.: Энергоатомиздат.

18. Kolehmainen, J. (2010). Synchronous Reluctance Motor with Form Blocked Rotor. *IEEE Trans. Energy Convers*., *25* (2), 450–456.
19. Gulbis, K., Kamoliņš, E., & Brakanskis, U. (2016). Synchronous reluctance machine with improved design of rotor mechanical strength connections. In *2016 IEEE 4th Workshop on Advances in Information, Electronic and Electrical Engineering (AIEEE 2016)*, (pp. 97–101). 10–12 November 2016, Lithuania, Vilnius.
20. Gulbis, K., Kamoliņš, E., Brakanskis, U., & Zarembo, J. (2020). Parameter calculation method of synchronous reluctance motor including cross magnetic saturation. In *2020 IEEE 61th International Scientific Conference on Power and Electrical Engineering of Riga Technical University (RTUCON)*. 5–7 November 2020, Riga, Latvia.
21. Rashad, E. M., Radwan, T. S., & Rahman, M. A. (2004). A maximum torque per ampere vector control strategy for synchronous reluctance motors considering saturation and iron losses. *In 2004 IEEE Industry Applications Conference, 39th IAS Annual Meeting*, (pp. 2411–2417). Seattle, WA, USA, doi: 10.1109/IAS.2004.1348813.

sciendo

LATVIAN JOURNAL OF PHYSICS
AND TECHNICAL SCIENCES
2022, N 4

DOI: 10.2478/lpts-2022-0032

DEVELOPMENT OF LIQUID CRYSTAL LAYER THICKNESS AND REFRACTIVE INDEX MEASUREMENT METHODS FOR SCATTERING TYPE LIQUID CRYSTAL DISPLAYS

A. Ozols[1*], G. Mozolevskis[2], R. Zalubovskis[3], M. Rutkis[2]

[1]EuroLCDs SIA, 2 Ventspils High Technology Park,
Ventspils, LV-3602, LATVIA
[2]Institute of Solid State Physics, University of Latvia,
8 Kengaraga Str., Riga, LV-1063, LATVIA
[3]Latvian Institute of Organic Synthesis,
21 Aizkraukles Str., Riga, LV-1006, LATVIA
*E-mail ainars.ozols@eurolcds.com

We report the measuring method of scattering type display liquid crystal layer thickness based on capacitance values suitable for inline production process control. The method is selected for its effectiveness and simplicity over spectroscopic methods as conventional methods for scattering type displays are not applicable. During the method approbation process, a novel diffuser liquid crystal mixture refractive index was determined based on liquid crystal layer thickness measurement data.

Keywords: *Cell gap, COMSOL, fast switching diffusers, LCD.*

1. INTRODUCTION

Liquid crystal (LC) layer thickness (commonly known as "cell gap") determination is one of the most critical measurements in liquid crystal display (LCD) development and manufacturing, since it determines their most important optical properties, such as transmission and scattering.

In LCD production process, liquid crystal layer thickness between both sides of display glass is formed during vacuum assembly. Thickness is controlled by adjusting spacer size and liquid crystal volume inside the cell. There are deviations caused by liquid crystal dispensing process and

evaporation rate in vacuum during assembly process which decrease production yield or lead to variations in optical properties. Excess of LC can cause visually distinct regions in lower part of display during intense use, called “gravity mura” [1].

Methods for determination of liquid crystal layer thickness using light polarization are well developed and commercially available but do not work for diffuser (light scattering) type LCDs [2]. Scattering LC displays become more and more important in times of digitalization, since they allow for fast adaptive optical elements and high-quality AR/VR visualization displays and glasses [3].

It has been shown that by using mathematical methods a cell gap can be calculated from transmittance spectrum [4], [5]. This indirect measurement method has drawbacks as it is done offline after the first sample production and requires idle production time while waiting for all process steps to be completed. For longer production runs process drift can happen without detection, even with periodic sample check. For certain cases, the use of interference patterns formed by the quasi-monochromatic light reflected from LCD has been reported for inline quality process control [2].

Second, it is not precise. Latest developments in diffuser technology have led to the situation when refractive indices (RI) of various layers are closely index matched, so spectroscopic determination of the maximum peaks becomes difficult. Moreover, this requires RI of material in the layer to be known. However, if novel LC mixtures are used, RI measurement requires to know layer thickness, first. LC refraction index over spectra measurement can be done by multi-wavelength Abbe refractometer [6] or using the spectral reflectometry method [7]. The spectrometer processes the light spectrum reflected or permeated by the sample. If the sample consists of a multilayer system in which multiple internal reflections occur, the interference bands may be observed in the spectrum, whose position is determined by the optical properties of the investigated layers – thickness and refractive index. At the Institute of Solid State Physics, this method is used to determine the breaking coefficients of 1 μm thick layers [5]. Abbe refractometer method has a problem in accuracy because it is difficult to control alignment distribution of LC.

If gap (layer)is filled by air instead of LC material, the interference peak determination is easy but it is commonly known in the industry that cell gap for unfilled displays is larger than for filled displays. After the layer is capillary-vacuum filled, extra pressing step is required to planarize the glass substrates and to bring filled layer to final value, when glass is resting on cell gap spacers. Thus, the layer thickness measured for unfilled displays is not valid any more. For more modern manufacturing method “one drop fill” display liquid crystal layer thickness is directly formed in vacuum with LC drops present, so the layer thickness is dependent on dispensed LC volume.

To overcome these limitations, scanning white light interferometric method was proposed [6]. While capable of determining liquid crystal layer thickness of different display types, it is not yet tested for scattering type of displays.

Additional challenge is the requirement to measure diffuser LCD in transparent mode after all production steps have been finished, as scattering mode typically hinders spectroscopic determination.

Capacitance measurements on the contrary can more easily be integrated in the production process as it is more simple technique. Display capacitance is dependent of liquid crystal layer thickness, and using its measurement we can compare

one display to another in the same series on condition that other parameters are constant and controlled. It might provide a convenient method for in-line process control, and if exact dependence is known, even absolute liquid crystal layer thickness values can be obtained. Display modelling by finite elements method can provide values of capacitance dependence from liquid crystal layer thickness, so a precise model of capacitive and resistive structures (Fig. 2) must be built. COMSOL Multiphysics software frequently is used for modelling complex capacitive systems in displays [8]. Use of software allows modelling displays with more complex electrode geometries like interplane switching electrodes or raised (slanted) electrode regions.

2. EXPERIMENTAL

Two types of functional LCD displays (61.8 x 48.8 mm) were prepared for the study using 2.7 μm spacers and the same layer construction but filled with different LC:

- Most commonly used standard "E7" LC mixture with well-known properties for reference purposes;
- Diffuser LC for measurement.

According to each LC type, polyimide layer had different LC alignment properties, planar for "E7" cell and homeotropic for diffuser.

Diffuser LC was prepared from mixture of "E7" (supplied by Merck) and 3 more components (supplied by the Latvian Institute of Organic Synthesis (LIOS)) with unknown refraction index, see Fig. 1.

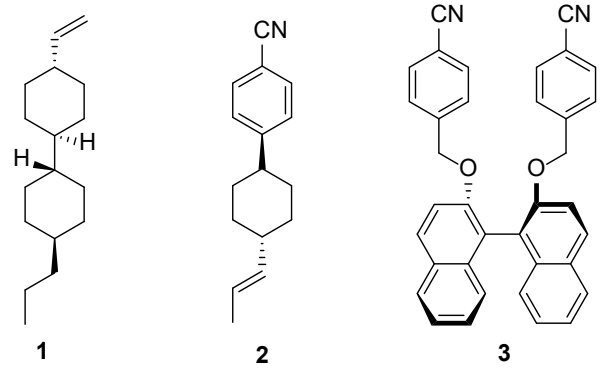

Fig. 1. Chemical compounds synthesized by LIOS, added to LC mixture. **1** ((1s,1'r,4R,4'R)-4-propyl-4'-vinyl-1,1'-bi(cyclohexane)), **2** (4-((1s,4s)-4-((E)-prop-1-en-1-yl)cyclohexyl)benzonitrile), chiral dopant **3** ((S)-4,4'-(([1,1'-binaphthalene]-2,2'-diylbis(oxy))bis(methylene))dibenzonitrile).

MODELLING AND VALIDATION

In order to evaluate liquid crystal layer thickness from measured capacitance data, diffuser and "E"7 display capacitive structure simulation model was built using COMSOL Multiphysics software, see Fig. 2. The model was used to analyse capacitance dependence on liquid crystal layer thickness, see Table 1.

Material	Thickness d, nm	Refractive Index n	Relative dielectric permittivity
Air	-	1.00	1.0
Glass	550000	1.52	7.75
SiO_2 barrier layer	20	1.52	2.18
ITO conductive layer	30	1.82	-
Silica based hard coat	95	1.75	14
PI alignment layer	55	1.58	3.6
LC layer	8000	1.71	9.6
PI alignment layer	55	1.58	3.6
Silica based hard coat	95	1.75	14
ITO conductive layer	30	1.82	-
SiO_2 barrier layer	20	1.52	2.18
Glass	550000	1.52	7.75
Air	-	1.00	1.0

Fig. 2. Capacitative and resistive structure of diffuser. Refractive index and permittivity data from supplier data sheets. On the left, glass and LC layer thickness is not shown on scale, indicated by zig-zag white lines.

Table 1. Modelled Capacitance Values

LC thickness, µm	Diffuser display capacitance, nF	"E7" display capacitance, nF
2.8	74.2	148.2
2.9	72.1	144.1
3.0	70.2	140.3
3.1	68.3	136.6
3.2	66.5	133.1

CAPACITANCE MEASUREMENTS

Both display types were measured for capacitance values with Agilent multimeter model 3606A and compared to modelled results, see Table 2. Measured values are lower than the modelled results. Multimeter uses lower voltage (20V) well below a switching threshold, when we are not completely aligning LC molecules and their orientation is unknown, so average relative permittivity is unknown. Note higher liquid crystal layer thickness value for sample P8-6, as it comes from different (assembled) LCD panel.

There are two other methods of capacitance measurement that can be used, one with resistor in series (method "R"), see Fig. 5, and second (method "C") with capacitor in series instead of resistor.

Table 2. Capacitance Values of Tested Displays with E7

Sample ID	Calculated gap, µm	Capacitance modelled, nF	Capacitance, Agilent 3606A, nF	Capacitance, method "R", nF	Capacitance, method "C", nF
P8-6	3.3	148.2	85±1	129±1	131±0.6
P6-13-R	2.9	148.2	78±1	144±1	144.1±0.6
P6-24-R	2.8	148.2	74±1	152±1	152.8±0.6
P6-6-R	3.0	148.2	78±1	139±1	140.1±0.6
P6-11	2.8	148.2	72±1	147±1	145.5±0.6

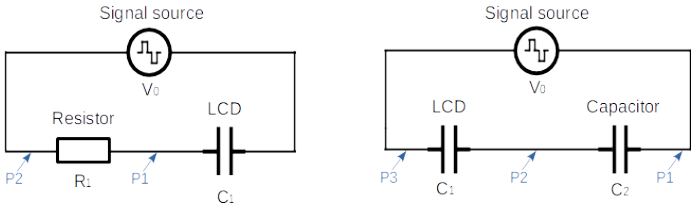

Fig. 5. Capacitance measurement methods. On the left with resistor in series "R", on the right with capacitor in series "C".

The test setup can be simplified to an RC circuit with a diffuser acting like a capacitor. The probes of an oscilloscope are connected to a resistor with a known and fixed value of approximately 10 k ohms. Also, the oscilloscope is configured to capture a measured signal when its value crosses some specific voltage level. For this experiment the trigger value can be set up to +10 and -10 volts for detecting the charge and discharge voltage curves, respectively.

From a standard RC circuit analysis, it is known that the voltage across the resistor will alter only during some rapid changes of the supply voltage or in our case, when the power supply is connected to and disconnected from the circuit. The voltage change on the resistor can be recorded and then converted to a current:

$$I(t)=V_m(t)/R\,, \tag{1}$$

which, by integrating it over the time, is transformed to the total charge that was accumulated on or released from the capacitor.

$$q=\int_{T_{START}}^{T_{FINISH}} I(t)dt\,. \tag{2}$$

This charge is then transformed to a capacitance:

$$C=q/V_s\,, \tag{3}$$

where V_s is the supply voltage.

The method with capacitor in series "C" is suggested [8] for faster switching systems, so it is preferred for this case. The method is also more convenient as capacitance value can be calculated directly from voltage measurements:

$$C_1=C_2\frac{V_2}{V_1}\,, \tag{4}$$

where
C_1 – capacitance of the diffuser;
C_2 – capacitance of serial capacitor that is known (300 nF for E7 cells);
V_1 – the voltage on capacitor C_1;
V_2 – the voltage on capacitor C_2.

Using method "C" measurements with capacitor with known value in series, we get similar capacitance results as with method "R".

SPECTROSCOPIC DETERMINATION

"E7" filled displays were also measured by a spectroscopic method. The required spectra in the 400–700 nm range were obtained using the Agilent Cary 7000 UMS spectrophotometer in five locations of each cell and liquid crystal layer thickness was calculated using the method developed by the Institute of Solid State Physics. The following parameters were used:

- Range ~550-750;
- No of points: 5;
- No of smooth cycles: 2;
- Fixed RI: 1.

Optical anisotropy of E7 LC is n_e=1.7472 and n_o=1.5217.

Extraordinary refractive index was used to calculate liquid crystal layer thickness (see Table 3). There is no difference observed when voltage is applied for most of the samples as expected since LC rotates only in XY plane.

Table 3. Liquid Crystal Layer Thickness of LCD Samples with E7

Driving conditions	Voltage on, 5V		Voltage off, 0V		Data from capacitance studies
Sample ID	LC layer thickness, µm	Stdev	LC layer thickness, µm	Stdev	LC layer thickness, µm
P8-6	3.0	0.2	3.0	0.2	3.3
P6-13-R	2.8	0.4	2.8	0.6	2.9
P6-24-R	2.9	0.2	2.9	0.2	2.8
P6-6-R	3.1	0.1	3.1	0.3	3.0
P6-11	3.1	0.2	3.1	0.2	2.8

REFRACTIVE INDEX DETERMINATION

To use a spectroscopic method for further cell gap measurement of diffuser displays, a refractive index must be known. To determine it, the layer thickness of LC must be known, first. If we take precautions that displays produced in the same conditions have the LC layer thickness, and fill some of them with liquid with the known refractive index different from adjacent boundaries so that interference peaks can be detected with ease and precision in transmission spectra. Obvious choice would be to use isotropic materials instead of LC, such as ethylene glycol and cinnamaldehyde. However, these materials evaporate during filling process in vacuum chamber, so LC with the known refraction index, "E7" typically used for comparable studies, was selected.

Displays were prepared in one batch, so one assumes that all test displays have equal LC layer thickness but an unknown absolute value, somewhat different from spacer size of 2.7 µm. To ensure equal layer thickness, during end sealing process when the excess of LC is squeezed out from cells under press, displays were mixed, see Fig. 4.

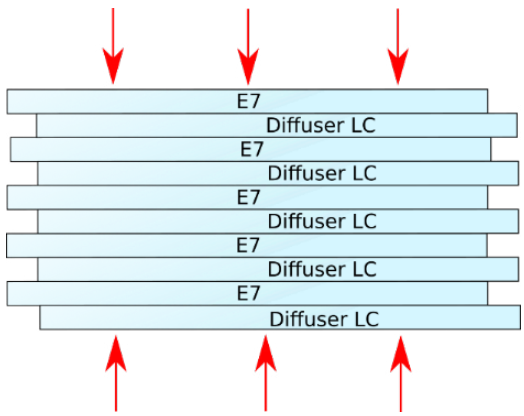

Fig. 4. Display pressing during end seal press step.

Using LC layer thickness calculated for samples with E7 LC, refractive index of diffuser LC was calculated and average *n* calculated, see Table 4. See values plotted in Fig. 5.

Table 4. Refractive Indices of Diffuser LC

Wavelength, nm	P5-6-R	P5-20-R	P5-15-R	P5-16-R	P5-10	P5-19	Average, n
738	1.52	1.48	1.50	1.50	1.50	1.48	1.50
711	1.52	1.51	1.51	1.50	1.51	1.51	1.51
683	1.53	1.55	1.52	1.57	1.52	1.52	1.53
660	1.57	1.55	1.55	1.57	1.55	1.52	1.55
636	1.57	1.51	1.55	1.58	1.55	1.55	1.55
617	1.60	1.58	1.59	1.61	1.54	1.58	1.58
596	1.68	1.61	1.61	1.64	1.61	1.57	1.62
580	1.70	1.62	1.63	1.71	1.62	1.62	1.65
563	1.78	1.69	1.69	1.72	1.63	1.69	1.70
549	1.69	1.66	1.67	1.70	1.72	1.66	1.68
535	1.81	1.77	1.77	1.81	1.77	1.69	1.77

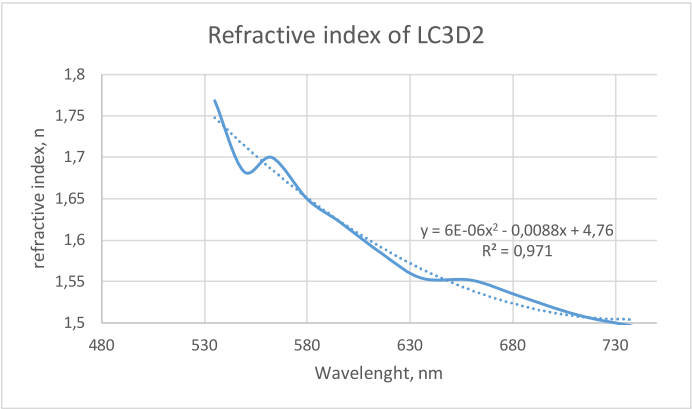

Fig. 5. Plotted *n* values of diffuser liquid crystal.

Refractive index measurement curve below 530 nm starts to have more interference, so 535 nm limit was used for curve estimation. The parabolic curve shape is in agreement with measurements for other LC mixtures in literature [6].

3. RESULTS AND DISCUSSION

To explain measured lower capacitance values than expected from calculations, we need to look at electro-optical response curves of the diffuser display, see Fig. 6. Before measurement, a diffuser display has static transmittance value between 30 % and 40 %, caused by relatively large light scattering domains that are orientated toward each other by weak intermolecular forces. Once low voltage is applied, transmittance drops

to expected transient low value, as now previously large domains are broken down into smaller domains due to electric field which overcomes weak positional intermolecular forces. If the voltage is increased, LC molecules align in the direction of applied field.

Capacitance measurements can be only used when LC has reached uniform homeotropic alignment under electric field, and is not changing when field strength is increased. In this case, if 90 V with known capacitor in series is used, see Fig. 7, the measured value corresponds to simulated capacitance values. The LC layer thickness of 3.0 µm is larger than spacers being 2.7µm, used for LC layer thickness control, so we conclude that cells have little excess of LC volume and glass is not completely resting on spacers. Spectrometric results corelate with model calculations, so the model can be used for other LC layer thickness and size diffusers.

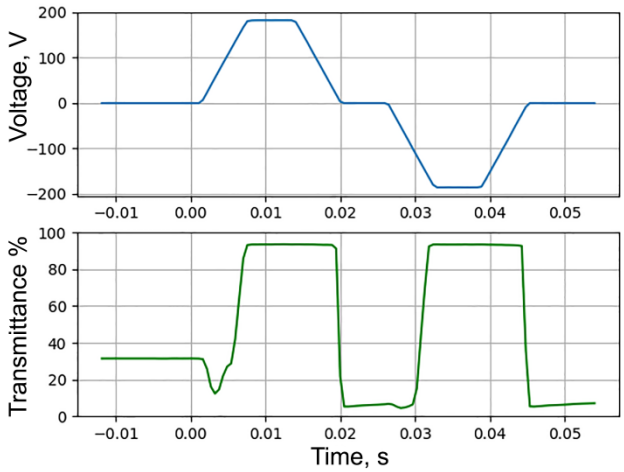

Fig. 6. Diffuser electro-optical response.

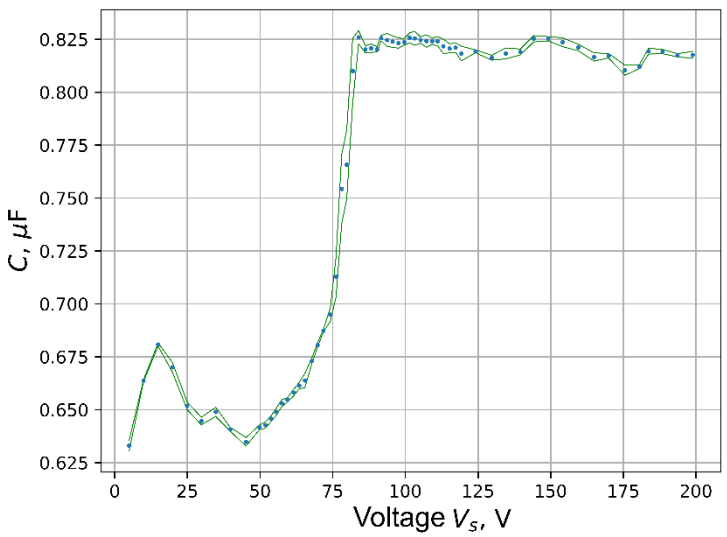

Fig. 7. Capacity measurements depending on measurement voltage with method “R”.

Four other diffusers of intended cell gap of 12µm (size 387.3x294.3mm) were selected for practical demonstration. All of them have quite identical current profiles during the charging and discharging processes.

For example, for the method with resistor, a graph of a resistor current starts as an approximately linear function and then transforms to an exponential decay curve for the second half of the charging process, see Fig. 8.

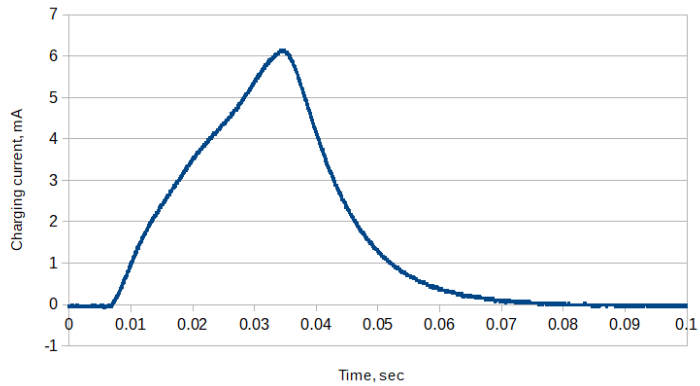

Fig. 8. Charging current of 387.3 x 294.3 mm 12µm diffuser in method "R".

This graph can be transformed to a function of a total charge that accumulates on a diffuser.

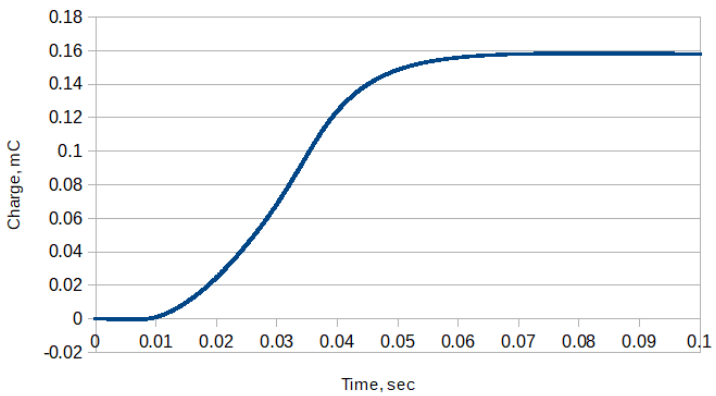

Fig. 9. Total charge stored on 387.3 x 294.3 mm 12µm diffuser during charging in method "R".

From Figs. 8 and 9, it is clear that 387.3 x 294.3 mm 12µm diffuser stores around 16 mC of charge; hence, by using Eq. (3), it is possible to conclude that its capacitance is equal to 0.8 µF. Approximately the same results were calculated for all of the diffusers in the same series, 4 in total. The consistency of the results indicates that that this capacitance value can be considered correct for this particular diffuser series and specific voltage supply level. With method C, we obtain the same capacitance values, as with method "R".

Table 5. Diffuser Capacitance Measurements

Display active area, mm	Calculated LC layer thickness, µm	Capacitance, Agilent 3606A, nF	Capacitance modelled, nF	Capacitance, method C, nF	Capacitance, method R, nF
61.8 x 48.8	3.0	50.8±2.9	70.2	69.7.±0.6	67±1
387.3 x 294.3	11.6	400	779.5	780±0.6	779±1

Using Comsol Multiphysics model, we find that the actual LC layer thickness is 11.6µ, see Table 5.

During the production process, it is important to measure LC layer thickness immediately after glass assembly into panel process, preferably by inline process control system. Coincidentally, standard display glass has notched corner for conductive side and flow direction identification purpose. After assembly both notched corners provide access to opposite display glass conductive layer, so capacitance value can be measured without completing further processing steps, like gasket curing, cutting and soldering of contact pads, see Fig. 10.

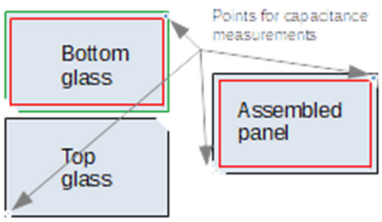

a)

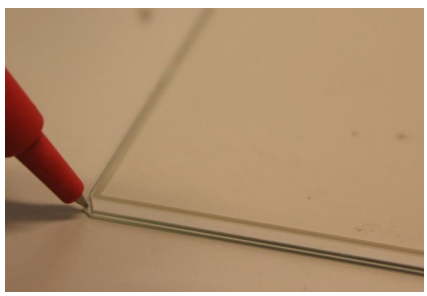

b)

Fig. 10. a) Assembled panel capacitance measurement points;
b) close-up picture of panel corner during the measurement.

4. CONCLUSIONS

We have proposed the control method of scattering type liquid crystal layer thickness based on capacitance measurements. Various capacitance measurement methods have been evaluated and method with capacitor in series has been found most convienent. Comsol Multiphysics software has been used to compute capacitance models.

Capacitance method has been compared through a spectroscopic measurement method using interference spectrum peak detection for LC with a known refractive index, and it has been found that both provide similar results.

At the same time, diffuser LC was filled in identical LC layer thickness cells and previously obtained value of layer thickness was used to determine a refractive index of novel liquid crystal mixture for diffuser (light scattering) LC. Knowledge of refractive index allows for further optimization of LCD cells in future by index matching.

The proposed LC layer thickness control method has been approbed for use in inline LCD production.

ACKNOWLEDGEMENTS

The research has been supported by ERDF No.1.1.1.1/19/A/120 “Improvement of Electro-Optical Characteristics of Liquid Crystal Shutters”.

REFERENCES

1. Cousins, J.R., Wilson, S.K., Mottram, N.J., Wilkes, D., Weegels, L.M., & Lin, K. (2018). A model for the formation of mura during the One-Drop-Filling process. In: *25th International Display Workshop*, 12–14 December 2018, Nagoya.
2. Valykh, S, Sorokin, S., & Chigrinov, V.G. (2015). Inline Quality Control of Liquid Crystal Cells. *Journal of Display technology, 11* (12), 1042–1047.
3. Zabels, R., Osmanis K., Ozols, A., Narels, M., Gertners, U., Smukulis, R., & Osmanis, I. (2020). Volumetric Technology: Enabling Near-Work Compatible AR Displays. *Proc. SPIE 11304, Advances in Display Technologies X,* 113040E, 1–9.
4. Bruyneel, F., Smet, H., Vanfleteren, J., & Calster, A. (2001). Method for Measuring the Cell Gap in Liquid-Crystal Displays. *Optical Engineering, 40,* 259–267.
5. Nitiss, E., Usans, R., & Rutkis, M. (2012). Simple Method for Measuring Bilayer System Optical Parameters. *Proc. SPIE, Opt. Micro- Nanometrology IV 8430,* 84301C-84301C–11.
6. Kao, C., Tsai, S., & Lu, S. (2009). Measuring Cell Gap of Liquid Crystal Displays by Scanning White-Light Tandem Interferometry. *Japanese Journal of Applied Physics, 48,* 106508.
7. Li, J., Wen, C., Gauza, S., Lu, R., & Wu, S. (2005). Refractive Indices of Liquid Crystals for Display Applications. *Ieee/ Osa Journal of Display Technology, 1* (1), 51–61.
8. Ding, L., Shih, W., Lin, M., Hu, Y., & Chang, P. (2012). An Analytical Model for Instant Design of an LCD Cell with Photospacers under Gravity and Local Loading. *Journal of the Society for Information Display, 20* (3), 148–155.
9. Feng, X., Beev, K., & Bos, P. (2019). Polarization-Independent Fast Optical Shutter with High Transmission. *Applied Optics, 58* (17), 4622–4629.

sciendo

LATVIAN JOURNAL OF PHYSICS
AND TECHNICAL SCIENCES
2022, N 4

DOI: 10.2478/lpts-2022-0033

THE GREEN HYDROGEN AND THE EU GASEOUS FUEL DIVERSIFICATION RISKS

L. Jansons[1,2], L. Zemite[1]*, N. Zeltins[1], I. Bode[1], I. Geipele[2], K. Kiesners[1]

[1]Riga Technical University,
Faculty of Electrical and Environmental Engineering,
Institute of Power Engineering
12-1 Azenes Str., Riga, LV-1048, LATVIA
[2]Riga Technical University,
Faculty of Engineering Economics and Management,
Institute of the Civil Engineering and Real Estate Economics,
6 Kalnciema Str. 210, Riga, LV1048, LATVIA
*e-mail: leo.jansons@rtu.lv

Hydrogen is the most abundant chemical element on the Earth, and it has really a wide variety of applications, starting from use in refining, petrochemical industry, steel manufacturing, and ending with use in energy production and renewable gas (*hereinafter* – RG) blending for gradual replacement of natural gas in all sectors of the national economy. Being practically emission-free, if produced in sustainable way or from renewable energy sources (*hereinafter* – RES), hydrogen is regarded as one of the most promising energy sources for decarbonisation of practically the entire segment of industrial and energy production. Growing pressure of the European climate neutrality targets has triggered special interest in production, use, storage and transportation of hydrogen – especially the green one, which can be used in at least four fundamental ways: as a basic material, a fuel, an energy carrier and an energy storage medium. In the context of sector coupling, however, hydrogen facilitates decarbonisation of those industrial processes and economic sectors in which carbon dioxide (*hereinafter* – CO_2) emissions can either not be reduced by electrification or this reduction would be minimal and linked to very high implementation costs. At the same time, development of an extensive hydrogen economy is the key to the achievement of the European climate protection targets, with the European Commission's (*hereinafter* – EC) Hydrogen Strategy, a framework created in 2020 to develop and promote sustainable hydrogen economy in the European Union (*hereinafter* – EU), in its centre.

Green hydrogen also will take its legitimate place in the gaseous fuel diversification risk management strategy, as this gaseous fuel is not only one of the most perspective future energy sources, but also one of the most volatile and demanding sources. In the process of gaseous fuel diversification in the EU and worldwide, new logistical chains and supply – demand networks of green hydrogen will emerge. Therefore, adequate addressing of potential challenges of this new regional and global production, delivery and consumption framework will be of utmost importance for secure, safe and predictable functioning of future energy systems.

Key words: *Diversification risks, gaseous fuels, green hydrogen, hydrogen technologies.*

1. INTRODUCTION

Hydrogen is the most abundant chemical element on the Earth, and it has really a wide variety of applications, starting from use in refining, petrochemical industry, steel manufacturing, and ending with use in energy production and renewable gas (*hereinafter* – RG) blending for gradual replacement of natural gas in all sectors of the national economy. It is also a rich source of energy, far more efficient than other fuels [1]–[3].

To be used in industry and energy production, however, hydrogen needs to be compressed to occupy the smallest possible volume. In comparison with other gases, it has the lowest molecular weight, low density, very low solubility in water and low dynamic viscosity. Also, hydrogen has high mass-energy density with very low volumetric energy density [4]. Other main characteristics of hydrogen are listed in Table 1.

Table 1. The Main Characteristics of Hydrogen

Molecular weight	g/mol	2.016
Density	kg/m^3	0.083
Higher calorific value	MJ/kg MJ/m^3	141.9 11.89
Lower calorific value	MJ/kg MJ/m^3	119.9 10.05
Boiling point	^0C	294
Density as liquid	kg/m^3	70.8
Critical point Temperature Pressure Density	 ^0C Bar kg/m^3	 306 12.84 31.40
Flame temperature	^0C	585
Diffusion coefficient	cm^2/s	0.61
Specific heat	KJ/kg K	14.89

Being a colourless and odourless gas, over time hydrogen has been given many colour markers, which describe sources and sometimes technology used in its production [5], rather than its actual chemical or physical properties. The colour marker of hydrogen, known as green one, is produced by using RES to power electrolysis that splits water molecules into hydrogen and oxygen. Green hydrogen formed through

this process is a clean energy source that can be effectively stored and transported over long distances.

The environmental challenges arising from the climate change have sparked particular interest in green hydrogen, which can be used as a fuel, an energy carrier and an energy storage option. In context of sector coupling, hydrogen facilitates the decarbonisation of those industrial processes and economic sectors in which CO_2 emissions can either not be reduced at all by electrification or only at considerable cost.

The experts are almost unanimous that development of an extensive hydrogen economy, based on sustainable forms of hydrogen – primarily, green hydrogen and blue hydrogen with carbon capture, utilization and storage (*hereinafter* – CCUS) is the key to the achievement of the European energy sector decarbonisation targets [6].

However, production of green hydrogen and sustainable forms of hydrogen using CCUS at the moment is at its infancy. In 2020, global hydrogen demand was 90 Mt, practically all produced almost exclusively from fossil fuels – natural gas and coal, resulting in close to 900 Mt of CO_2 emissions. The average global percentage of hydrogen produced from natural gas stands in more than 70 % [7]. At the same time, by mid-2021, a global capacity of electrolysers, which are needed to produce green hydrogen, doubled over the last five years to reach just over 300 megawatts (*hereinafter* – MW). Around 350 projects currently under development could bring global capacity up to 54 giga-watts (*hereinafter* – GW) by the end of this decade. Another 40 projects accounting for more than 35 GW of electrolyser capacity are at the early stages of development. The main green hydrogen source technologies are alkaline water electrolysis, proton-exchange membrane electrolysis, and solid oxide electrolysis, with the latter being in the research and first-trial phase [8]. If all planned projects are completed, global green hydrogen supply could reach more than 8 Mt by 2030, but this is still well below the 80 Mt required in the way to net zero CO_2 emissions by 2050 set out in the IEA Roadmap for the Global Energy Sector, or 70Mt short of the most conservative EU energy decarbonisation target for the same date [9].

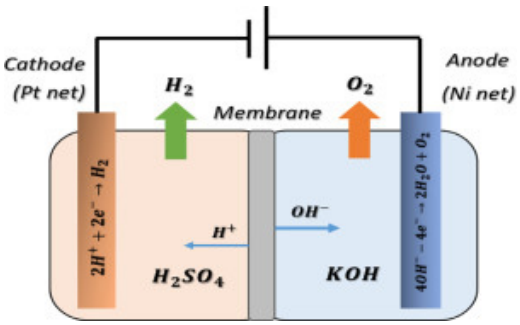

Fig. 1. The general principle of water electrolysis.

2. THE GLOBAL HYDROGEN DEVELOPMENT TRENDS

At present, Europe is a leading green hydrogen producer and electrolyser capacity deployer, with 40 % of global installed capacity, and is set to remain the largest market for this resource in the near term, as ambitious hydrogen strategies of the EU [10] and the United Kingdom [11] have been reviled in recent years. Moreover, supranational hydrogen strategies like one deployed by the EU is also strongly backed by Member States' commitment for hydrogen initiatives, with provision of financial support and necessary sector regulations. As of 2021, over thirty countries worldwide have produced hydrogen related framework documents, such as hydrogen strategies and

road maps, and have committed more than $70 billion in public funding to support the practical action. The German federal government alone is planning to provide up to 9 billion euros (*hereinafter* – EUR) by 2040 to implement its national targets and to build hydrogen-related international partnerships not only at the regional, but also at the global scale. The EC expects that cumulative investment in hydrogen in Europe will make up to 480 billion EUR by 2050.

In Europe, the first ever continent-wide initiative to unify hydrogen transportation and storage infrastructure is deployed, known as the European Hydrogen Backbone (*hereinafter* – EHB) [12]. This initiative consists of a group of thirty-one energy infrastructure operators. The EHB aims to accelerate Europe's decarbonisation journey by defining the critical role of hydrogen infrastructure – based on existing and new pipelines – in enabling the development of a competitive, liquid, pan-European green and sustainable hydrogen market [13].

Also in the United States, movement towards strong promotion of green hydrogen economy shift is seen not only on the federal, but also on the state level. More than thirty states have already adopted plans to promote sustainable hydrogen production and consumption technologies. The goal is to build a broad-based hydrogen industry that in 2030 will generate $140 billion in annual income and employ more than half a million people. The United States is stepping up ambitions with the Energy Hydrogen Program Plan [14], which is one of the most detailed and ambitious hydrogen strategical document to date.

China, one of the biggest consumers and producer of fossil hydrogen, is also planning to invest in the promotion of green and sustainable technology over the next years, which should result in innovative hydrogen production facilities throughout the country. On 23 March 2022, China released a plan on the development of hydrogen energy for the 2021–2035 period, as the country would strive toward its carbon peaking and neutrality goals. By 2025, China will put in place a relatively complete hydrogen energy industry development system, with the innovation capability significantly improved and the core technologies and manufacturing processes basically mastered, according to the plan jointly released by the National Development and Reform Commission and the National Energy Administration. Annual hydrogen production from renewable energy is expected to reach 100 000 t to 200 000 t to become an important part of new hydrogen energy consumption by 2025, and enable CO_2 emission reduction of one million to two million t per year [15].

Also, Australia's National Hydrogen Strategy [16] suggests that it could catch up with Europe in a few years. In context of this document, Australia is about not only to produce and use green and sustainable hydrogen domestically, but also to build up international partnerships, establish well-balanced and transparent guarantee of origin scheme, and create hydrogen industrial hubs in different regions of the country [17].

Bearing in mind that not only production of green hydrogen alone can help radically decarbonize the energy production and industry, but also production of hydrogen from fossil fuels with CCUS could help the matter in short and mid-time perspective, CCUS technologies are also strongly backed and promoted. As for early 2021, sixteen projects for producing hydrogen from fossil fuels with CCUS were operational, producing 0.7 Mt of hydrogen annually. Another fifty projects are under development and, if realized, could increase the annual sustainable hydrogen production to more than 9 Mt by 2030. Canada and the United States lead in the production of

hydrogen from fossil fuels with CCUS, with more than 80 % of global capacity production, although the United Kingdom and the Netherlands are pushing to become leaders in the field and account for a major part of the projects under development [12].

While hydrogen, from a technological point of view, can be used for diverse purposes, the development of a sustainable hydrogen economy is still controversial, because major challenges are presented by the production, storage and transport of hydrogen.

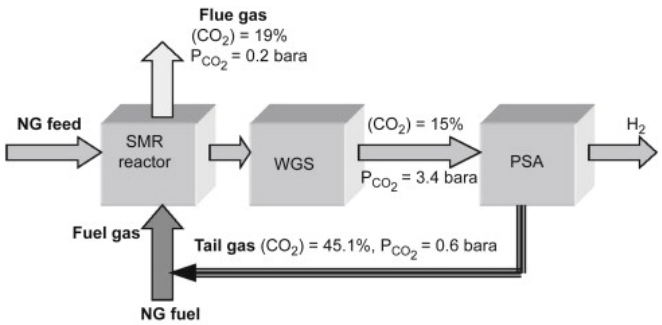

Fig. 2. The principle of methane steam reforming.

A crucial element of a sustainable hydrogen economy is cost-efficient production of green hydrogen. Currently, only about 5 % of hydrogen worldwide is produced via electrolysis, but, at the same time, by 2021, 76 % of all global hydrogen came from the natural gas produced via methane steam reforming cycle [7]. In comparison with electrolysis, steam reforming requires half as much water and significantly less energy. As this process is more cost-effective, natural gas could theoretically remain the predominant energy source for hydrogen production in the short and mid-time perspective. Moreover, the storage and transport of hydrogen present particular technical challenges: hydrogen is usually cooled to minus 253 ^{0}C or stored under very high pressure [18]. Possible alternatives, which make it easier to transport and store hydrogen, include conversion to ammonia, binding to liquid organic hydrogen carriers (*hereinafter* – LOHC) and the production of renewable fuels, such as methanol [19]. However, the conversion and reconversion processes result in energy losses, and some of these processes are not currently ready for the industrial scale usage.

3. ADVANTAGES AND CHALLENGES OF WIDER HYDROGEN USE

In a long-term energy sector transformation perspective, sustainable and in particular green hydrogen can help tackle various critical energy and industrial challenges. First of all, this resource offers ways to decarbonize a wide range of sectors of the national economy, such as freight, air and maritime transport, chemical industry, including production of fertilizers, iron and steel. In all these sectors of the national economy, it has been proven difficult to meaningfully reduce CO_2 emissions. Hydrogen can also help improve air quality and strengthen energy security [20]. Despite very ambitious international climate goals, global energy-related CO_2

emissions reached an all-time high just recently – in 2018 [21]. Outdoor air pollution also remains a pressing problem, with several million people dying prematurely each year.

The strong advantage of wider use of hydrogen is a fact of its versatility. Technologies available today enable hydrogen to produce, store, move and use energy in different ways. A wide variety of fuels are able to produce hydrogen, including RES, nuclear, natural gas, coal and oil [22]. It can be transported as a gas by pipelines or in liquid form by ships, much like liquefied natural gas. It can be transformed into electricity and methane to power households and feed industry, and into fuels for almost all kinds of transport. At the same time, hydrogen can enable RES to provide an even greater contribution to global and the European energy transition. It has the potential to help with variable output from RES, like solar photovoltaics (*hereinafter* – PV) and wind, whose availability is not always well matched with demand curves [23]. Hydrogen is one of the leading options for storing energy from RES and looks promising to be a lowest-cost option for storing electricity over a long period of time. Hydrogen and hydrogen-based fuels can transport energy from RES over long distances – from regions with abundant solar and wind resources, such as Africa and Australia, to energy-hungry industrial cities thousands of kilometres away [16]. With a global energy sector in flux, the versatility of hydrogen is attracting stronger interest from a diverse group of governments and companies. Support is coming from governments that both import and export energy as well as RES electricity suppliers, industrial gas producers, electricity and gas utilities, car industry, and oil and gas companies.

To this date, hydrogen is used mostly in oil refining and for the production of fertilizers. But, to make a significant contribution to clean energy transitions, it also needs to be adopted in sectors where it is almost completely absent at the moment, such as transport, buildings and power generation [24]. In this context, however, clean, widespread use of hydrogen in global energy transitions faces several challenges, too. It is common knowledge that producing hydrogen from RES is still costly. According to the International Energy Agency (*hereinafter* – IEA), the cost of producing hydrogen from RES electricity could fall 30 % by 2030 as a result of declining costs of RES and the scaling up of hydrogen production. Fuel cells, refuelling equipment and electrolysers can all benefit from mass manufacturing [9].

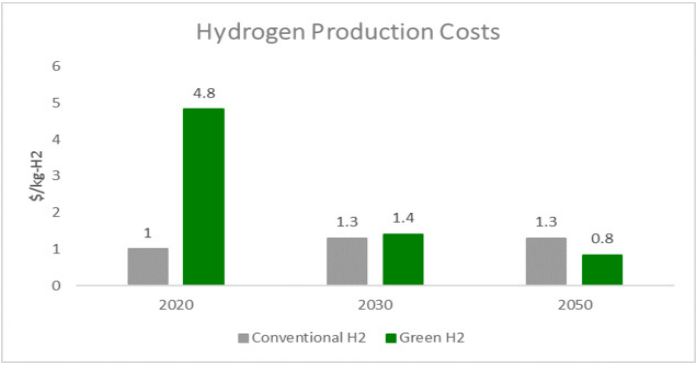

Source: NRDC

Fig. 3. Estimated conventional and green hydrogen cost (2020–2050).

The development of hydrogen infrastructure, including pipelines and large-scale on-ground and underground storage facilities, is slow. Hydrogen prices for consumers are highly dependent on how wide accessibility of resources is at the moment, and how often they are used and how much hydrogen is delivered in a specific period of time (per day, week or month). Tackling this issue is likely to require planning and coordination that bring together national and local governments, industry and investors.

As hydrogen currently is almost entirely produced from natural gas and coal, it is already used at an industrial scale, but its production is responsible for huge annual CO_2 emissions. Harnessing this existing scale on the way to a clean energy future requires both capture of CO_2 from hydrogen production from fossil fuels and greater supplies of green hydrogen. It also must be pointed out that industrial scale usage of hydrogen worldwide is sporadic in its sense – hydrogen is produced and used locally, without a need to develop an extensive logistical network and assure mobility of resources at least at a regional scale. Within the EU, Clean Hydrogen Partnership's hydrogen regional initiative has been carried out since 2016, with significant efforts to reach out to all those European regions and cities having an interest in the potential use of fuel cell and green or sustainable hydrogen-based products to help them achieve their decarbonisation goals [25].

In regulatory sense, regulations limit the development of a clean hydrogen industry, so government and industry must work together to ensure that existing regulations are not becoming unnecessary barriers to investment and subsequent market growth. The hydrogen market expansion would benefit immensely from common international standards for the safety of transportation and storage of large volumes of hydrogen, and for tracing the environmental effects of different hydrogen logistical chains.

4. HYDROGEN IN HEAT AND POWER GENERATION, AND ITS TRANSPORTATION OPTIONS

4.1. Hydrogen in Heat and Power Generation

It is believed that green and sustainable hydrogen, first and foremost, is meant to be used in decarbonisation of industry and energy generation processes, with smaller segments of energy sector not being the first priority. District and local heating are one of these sectors, where there is a great dispute on the necessity to include hydrogen in energy mix in Europe in a short and mid-term perspective. According to the IEA, globally, district heating supplies a relatively small share of heat used in buildings, at only 8.5 % of the sector's heat consumption – a share that has remained impressively constant since 2000, considering that floor area has increased by 65 % at the same time. Although the global average share is low, district heating does cover a high portion of heat delivered to buildings in some European countries, such as Denmark and Sweden (both above 45 %) [26].

As usage of natural gas in district heating is still rather widespread in the EU and the United Kingdom, the injecting of up to 10 % hydrogen (by volume) into the natural gas transportation and distribution networks would not require any major alterations to equipment and would significantly reduce

CO_2 [27] for households and small business consumers. At the same time, injection of up to 10 % hydrogen into the natural gas networks would contribute not only to district heating companies and their clients, but also to local and individual heating system users. They would also use hydrogen – natural gas – biomethane blend in their natural gas boilers and other equipment, not replacing them by new ones, and, at the same time, contributing to national and the EU emission reduction targets [28].

In the electricity sector, burning of liquid and gaseous hydrocarbons, currently represents the largest share of electricity generation around the world. Countries with limited RES and hydrocarbon resources rely significantly on expensive imported and polluting fuels. Importing electricity through transmission lines might sometimes be problematic due to high costs, system losses, and geographical barriers [29]. However, green hydrogen offers a viable alternative. Countries importing large amounts of hydrocarbons today, in the near future could switch to import of low-cost green hydrogen and convert it into electricity through large-scale fuel cells in domestic power plants [1]. Hydrogen concentrations of up to 10 % and 20 % are still permissible for the operation of turbines and compression stations, respectively, while pipelines can stand mixtures of up to 50 % (given some technical adjustments); anything above those values is currently still being researched [30]. For instance, Mitsubishi Hitachi Power Systems, Ltd. has recently disclosed the successful test of a large-scale highly efficient turbine fed with a 30 % hydrogen blend, attaining a stable combustion with a 10 % reduction in CO_2 emissions [31].

4.2. Hydrogen Transportation Options

In order to transport hydrogen, it needs to be compressed, liquefied or chemically combined. Safe and cost-efficient transport and distribution of hydrogen are critical for its large-scale deployment, as its low energy density, high diffusivity, and high flammability imply important technological and infrastructural challenges associated with the transport and large-scale adoption in such markets, as sustainable district and local heating or transport. It is likely that the initial adoption and use will be locally concentrated in hydrogen hubs or hydrogen valleys [32], while for global large-scale integrated value chains it will take longer to emerge. In terms of means of transport, hydrogen can be transported by road and rail, as gaseous or liquid, in special vessels, tubes, and containers, by sea, primarily in specialized cryogenic tankers in a liquefied form, and by pipelines, which can carry either pure methane-biomethane, pure hydrogen or a blend [12]. For distances that fall below 2000 km, transporting hydrogen through pipelines is the lowest-cost option. In case of longer distances, ammonia shipping is the most economical solution. It is estimated that investments required to meet green hydrogen export demand in 2050 are around $2.1 trillion, where $1 trillion would go to building the dedicated RES capacity, $900 billion – to setting up the hydrogen conversion and export facilities, and $200 billion – to developing the water electrolysis facilities [1].

4.3. Building up New Pipelines or Retrofitting the Existing Ones

At the same time, hydrogen blending into the existing natural gas network has multiple advantages and can be a cost-effective transitional option in the short term in regions without parallel or duplicated networks. The retrofitting and repur-

posing of existing natural gas networks can be combined and complemented with the construction of new dedicated hydrogen infrastructure. It needs to be reminded that a purely hydrogen pipeline infrastructure is not a novelty. Such networks, although strictly compact and localized, are already used to supply single consumers, for example, petrochemical and fertilizer plant. At present, a 900 km long hydrogen pipeline network is built along the Gulf coast of the United States, which is regarded as the longest high-pressure hydrogen transportation network in the world [33]. In Europe, currently the largest and longest industrial hydrogen pipeline network is located in the area of ports of Rotterdam and Antwerp, with total length around 1500 km, where the longest part consists of small diameter distribution infrastructure [12]. In line with this, there are various initiatives, EHB and the Re-Stream studies carried out [34], in order to assess the potential of the existing European oil and gas infrastructure to carry hydrogen and/or carbon monoxide.

In addition, in the EU, a well-developed and regulated network of natural gas is already in place, with the transmission grid being approximately 200 000 km long.

A distribution grid, which is double the size of the current transmission grid, implies that the natural gas infrastructure is the key enabler for the deployment of a hydrogen economy. The UNECE Group of Experts on Gas recognised the key role of the natural gas transmission and distribution operators (*hereinafter* – TSO, DSO), natural gas industry and the natural gas infrastructure in the transition to a hydrogen economy through the energy system integration [35]. Even though pipelines and the natural gas storage facilities today are being considered the most cost-competitive solution for hydrogen distribution, numerous challenges remain. One of them is an increasing difficulty of building new pipelines, as many landowners are not ready to have such objects close to their properties. Thus, it is in the best interest of actors in the hydrogen value chain to find ways to extensively reuse existing natural gas infrastructure instead of constructing an entirely new hydrogen infrastructure. It is necessary to start immediate retrofitting and repurposing of current natural gas infrastructure. Given TSO and DSO know-how in operating natural gas transmission and distribution infrastructure, the gas TSOs should be among those certified as owners and operators of future hydrogen networks [36]. Authorizing the natural gas TSOs to carry out activities related to the development, integration and operation of hydrogen infrastructure would facilitate an efficient way forward due to their experience in planning, financing, constructing, operating and maintaining gas infrastructure, since existing gas grids will be retrofitted and repurposed for hydrogen [12].

5. OUTLINING THE MAJOR HYDROGEN-RELATED RISK ASSESSMENT

Work is underway worldwide to further develop technologies in the fields of hydrogen electrolysis, storage and transportation. The vast majority of hydrogen today is produced and used on-site in industry. The production of ammonia and oil refining are the prime purposes, accounting for two-thirds of hydrogen use. Ammonia is used as nitrogen fertilizer and for the production of other chemicals. At petroleum refineries, hydrogen is added to heavier oil for transport fuel production [37].

What is new is that the type and scale of its use are changing fundamentally, with the expected rapid growth of generation capacities in close future. New companies are entering the market as planners, manufacturers and operators, but there is a steep learning curve involved. Established players size up their offers and are simultaneously required to find skilled staff and realise cost-saving potential. As such, all projects require careful risk assessment. The potential risks involved with green hydrogen production, storage and transportation include, but are not limited to: *fire and explosions, market immaturity, material embrittlement and business-related challenges.*

5.1. The Major Physical Hydrogen-Related Risks

Possibility of fire and explosion is the main risk when handling hydrogen, as it is highly explosive, when mixed with air. In addition, leaks are hard to identify without dedicated detectors because hydrogen is colourless and odourless [38]. A hydrogen flame is almost invisible in daylight. Industry loss investigation statistics show that approximately one in four hydrogen fires can be attributed to leaks, with around 40 % being undetected prior to the loss. Fire and explosion protection needs to be considered on three different levels: preventing the escape of inflammable gases as much as possible, ensuring safe design of electrical and other installations in areas where ignition sources cannot be excluded, constructing buildings and facilities to withstand an explosion with limited damage [39].

Proper handling of hydrogen is critical, and any emergency requires appropriate fire safety equipment. An AGCS analysis of more than 470 000 claims across all industry sectors over five years shows how costly the risk of fire and explosion can be. Fire and explosions caused considerable damage and destroyed values of more than €14 billion ($16.7 billion) over the period under review [40].

Material or metal embrittlement or hydrogen-assisted cracking (*hereinafter* – HAC) *is another potentially dangerous side effect of hydrogen handling.* Diffusion of hydrogen can cause metal and steel, especially high-yield steel, to become brittle, and a wide range of components could be affected, for example, piping, containers or machinery components. For the safety of hydrogen systems, it is important that problems such as the risk of embrittlement and HAC are taken into account at the design phase. This is ensured by selecting materials that are suitable under the expected loads as well as considering appropriate operating conditions (pressure, temperature, mechanical loading). High-yield strength steel is particularly at risk of hydrogen-related damage [41].

5.2. Business and Market Formation Related Risks

Business inconsistency or interruption risks are also potentially present in green and sustainable hydrogen risk management. Hydrogen production, transportation and distribution involve high-tech equipment and failure to critical elements could result in significant financial losses. For example, in case of damage to electrolysis equipment or heat exchangers in liquefaction plants, it could take very long to replace such essential equipment, resulting in production delays. In addition, such interruption costs following a fire can add significantly to the final loss

total. For example, AGCS analysis shows that, across all industry sectors, the average business loss from fire incidents is around 45 % higher than the average direct property loss – and in many cases the business interruption share of the overall claim is much higher, especially in volatile segments such as oil and natural gas [40].

Slow market development also represents a potential threat to widespread green hydrogen penetration of crucial European economy sectors, as hydrogen infrastructure development is still at an early stage. As mentioned previously, a group of the European companies and TSOs have proposed to start planning the EHB. As large supply corridors come together, a core EHB can be envisaged by 2040. This means that a pan-European hydrogen infrastructure can be created connecting twenty-eight European countries. By 2040, the proposed backbone can have a total length of almost 53 000 km, consisting of approximately 60 % repurposed existing infrastructure and 40 % of new hydrogen pipelines. Assuming that the backbone is equipped with a fit-for-purpose and technically robust compression system, the proposed network could be able to adequately meet the expected annual hydrogen demand in Europe by 2040 [42]. But, at the moment, creation of such massive infrastructure and retrofitting of existing natural gas pipelines are moving at a rather slow pace, putting a major accent to the regulatory framework of infrastructure building.

In this context, massive public investments and financing are to be committed to kick-starting the hydrogen market. The conditions for access to the transmission networks and common rules for the internal market in hydrogen need to be designed, as well as the framework for how hydrogen should compete for demand. In many respects, this is far from simple, particularly with respect to trading rules and guarantees of origin. There are many unknowns, and considerable technological development will occur in upcoming years. For example, promising new manufacturing processes for zero and even negative carbon hydrogen are emerging, such as pyrolysis powered by RES. It is important not to create market structures and support mechanisms for financing what may become stranded assets [43].

Therefore, at this stage, the best way to establish the basic future hydrogen market rules would be to follow the logic and principles established for the regulation of the natural gas market through the EU directive on gas and hydrogen networks [44]. On 15 December 2021, the EC adopted a legislative proposal to recast the 2009 EU Gas Directive [45], as part of the proposed hydrogen and decarbonised gas markets package. This reflects the EU's growing climate ambitions, set out in the European Green Deal and its "Fit for 55" package. The EC's proposal aims to support the decarbonisation of the energy sector by ramping up the production of RG and hydrogen, and facilitating their integration in the EU energy networks. The recast directive would become a central element of a new EU legislative framework for hydrogen networks, comparable to those that already exist for natural gas and electricity. The proposal would refine the principles of the existing Gas Directive and fully extend its scope to cover hydrogen networks. This includes an important set of consumer rights, provisions relating to TSOs and DSOs – especially, their unbundling, third-party access and integrated network planning, and independent regulatory authorities [46].

6. HYDROGEN AND THE GASEOUS FUEL DIVERSIFICATION RISKS

The gaseous fuel diversification, which includes, but is not limited to wider RG usage in energy generation and energy intensive industry throughout the EU, has strong national economy and climate related advantages. But, at the same time, gaseous fuel diversification, especially when carried out at a large scale, can be associated with numerous risks factors. These risks can vary from sector to sector, and apply not only to large-scale energy and industrial processes, but to a residential gas supply as well.

A risk matrix is one of the most effective assessment tools to pinpoint and generalize risks factors [47] that can be present in residential gas supply sector during a period of gaseous fuel diversification. If the main avenues of gaseous fuel diversification correspond to blending of the following RGs: biomethane and green hydrogen, into existing natural gas networks with subsequent delivery of blended resources to all consumers, including residential ones, – risks associated with it fall into two categories. The first category is methane rich fuel associated risks (the natural gas and biomethane) and the second – non-methane rich fuel associated risks (hydrogen). The first category includes the natural gas related risks, as chemically biomethane is a substance identical to it. These risks are leaks, fire, explosion and suffocation; however, natural gas alone will not burn or explode. It needs the right amount of air and an ignition source. The second category includes green hydrogen (or hydrogen of any origin) that could be blended with methane and biomethane in low proportions with minimal investments into the existing natural gas systems. The share of hydrogen in a blend may range up to 10 % by energy, although this is subject to ongoing debate. Any quantity of hydrogen exceeding a 10 % threshold may require either major network repurposing measures or a buildout of an entirely new hydrogen pipeline networks [27].

The main risk factors associated with usage of pure hydrogen or high concentration of hydrogen in hydrogen-methane blends are propensity to leaks, as hydrogen can diffuse through many materials considered airtight or impermeable to other gases, buoyancy as hydrogen is the lightest known gas that rises quickly under atmospheric conditions, flammability – when mixed with air, hydrogen can easily ignite or/and explode, hydrogen-induced cracking as reduction in the ductility of metal can occur due to absorbed hydrogen (in steel, iron, nickel, titanium, cobalt, and their alloys). Also risks of proper mechanical blending of hydrogen and methane may arise in certain situations that might, among other, result in rising gaseous fuel usage risks in the residential sector, especially, when domestic appliances that are not designed to run on a high mix of hydrogen (gas boilers, furnaces, cook stoves etc.) are concerned. To mitigate these risks in a timely manner, at least part of them have to be replaced with hydrogen-compatible alternatives, which are currently available to consumers in rather limited amounts [37].

As with any energy risk, fire and explosion is a key point. Business interruption and liability exposures are also important, as are transit, installation and mechanical failure risks. There is rightly great enthusiasm around hydrogen solutions as a key driver toward a low-carbon economy, but it should not be neglected that these projects involve complex industrial and energy risks and require high levels of engineering

expertise and insurance know-how to be able to provide coverage.

To some extent, risks related to smart gas distribution can also be listed in association with hydrogen risks, as smart gas distribution is being built upon natural gas and biomethane, bearing in mind prioritization of their chemical and physical properties. An important factor that ought to be examined is the effect of hydrogen blending in the natural gas supply chain. Considering an average lower calorific value of natural gas and hydrogen [48], injection of hydrogen into natural gas networks will inevitably translate into reduction in the calorific power of the blend. From a theoretical point of view, a blend with significantly more than 10 % of hydrogen, the calorific value of which remains within the limits currently imposed by regulation, might pose certain challenges for some smart gas distribution network elements [49].

Hydrogen underground storage associated risks are still analysed by the industry experts not only in Europe, but also in other parts of the world. Underground hydrogen storage facilities can be distinguished from other types of energy storage primarily by the large volume of gas stored, the seasonal or long storage period, and large capital expenditures related to their construction and exploitation, as their economic viability is directly affected by the cost of electricity for water electrolysis and the construction costs [50]. Some parameters affect underground storage differently, for example, low viscosity of hydrogen and the associated rate of gas movement carry a higher risk of leakage.

For underground hydrogen storage different types of storage – namely, salt caverns, deep water aquifers and depleted oil and natural gas reservoirs – have been proposed [51], which are specific environments characterised by potentially high microbial abundance and activity. Subsurface microorganisms can use hydrogen in their metabolism and thus lead to a variety of undesired side effects or risks, such as hydrogen loss, methane and acid formation, as well as clogging and corrosion [52].

In contrast to above ground storage systems, underground gas storages have several strong advantages, too: they allow gas to be stored in large quantities, thus reducing storage costs, ensure storage safety – underground storage is less vulnerable to fire or terrorist attack, optimize the land use – traditional above ground storage may occupy significant areas, which might be used for other purposes, and existing engineering and safety management experience in underground gas storage sector (regarding storage of natural gas) [53].

6. CONCLUSIONS

The EU gaseous fuel diversification risks fall into several categories and they may be mitigated in various ways. In order to mitigate the EU gaseous fuel diversification risks, it is necessary to evaluate mitigation pathways, which are close to future tasks of hydrogen sector development, and not the current situation of its development. The following pathways therefore must be addressed with particular attention.

One of the long-term risk mitigation ways is to establish a stable role for green and sustainable hydrogen in long-term energy strategies. This concerns not only supranational and the national framework documents, but also regional and city-wide initiatives that can guide and help the hydrogen economy to grow on various

levels. The businesses and other companies should also have clearly defined long-term energy goals, which, if necessary, should define their own green hydrogen adaptation agenda. Key sectors here include, but are not limited to refining, chemical industry, iron and steel production, freight, long-distance, air and maritime transport, building sector, and power generation and storage. It means that stimulation of commercial demand for green hydrogen also would follow the framework strategic initiatives, as incentives for doing so would also become more and more present in different consumption segments. At the moment, sustainable and green hydrogen technologies are available on the market; thus, their costs are rather challenging. Policies that create sustainable markets for green hydrogen and help reduce emissions from fossil fuel-based hydrogen are needed to underpin investments by suppliers, distributors and consumers. By scaling up supply chains, these investments can drive cost reductions, whether from low-carbon electricity or fossil fuels with carbon capture, utilization and storage. New applications for green and sustainable hydrogen, as well as hydrogen supply and infrastructure projects stand at the riskiest point of the deployment curve.

The other important issue to mitigate the EU gaseous fuel diversification risks regarding green hydrogen is widespread support for research and development (*hereinafter* – R&D) activities to eventually bring down green and sustainable hydrogen production costs. Alongside cost reductions from economies of production scale, R&D is crucial to lower costs and improve performance, including for fuel cells, and hydrogen-based fuels. Government actions, including the use of public funds, are critical in setting the long-time research agenda and gradually attracting private capital for innovation.

Elimination of regulatory barriers and harmonization of standards are the issues addressed in the EU gaseous fuel diversification risk mitigation. Green hydrogen project developers in the EU still face impediment, where regulations and permit requirements are unclear, unfit for new purposes, or inconsistent across sectors and countries. Sharing knowledge and harmonizing standards is a key, including for equipment, safety and certifying emissions from different sources. Enhancement of international cooperation is needed across the board but especially on standards, sharing of good practices and cross-border infrastructure. Hydrogen production and use need to be monitored and reported on a regular basis to keep track of progress towards long-term goals. By relying on current policies, infrastructure and skills, these mutually supportive opportunities can help scale up infrastructure development, enhance investor confidence and lower costs. For instance, it is possible to use the most of existing industrial ports to turn them into hubs for lower-cost, lower-carbon hydrogen, use existing gas infrastructure to spur new clean hydrogen supplies, support transport fleets, freight and corridors to make fuel-cell vehicles more competitive, and establish the first shipping routes to kick-start the international hydrogen trade.

The EU gaseous fuel diversification risks of green and sustainable hydrogen can also be minimalized and mitigated by building up and improving the planning and simulation process of the entire hydrogen production, transportation and consumption chain – green hydrogen ecosystem. Here digital twin (*hereinafter* – DT) technologies can be successfully used for the intelligent management of all types of data. By using different applications, for instance, the internet of things, software simulation, and data analytics, DT technologies

create a digital replica of a physical object or a system, in this case – even a replica of green hydrogen ecosystem. DT use is gaining momentum due to rapidly evolving simulation and modelling capabilities, better coupling between interoperability and the internet of things sensors, and increased availability of infrastructure for the use of digital devices. Furthermore, DT technologies have proven to offer advantages in accelerating technology growth, optimizing design, and improving return on capital. Despite the potential offered by DT technologies, little attention has been given to their application in green hydrogen facility design. To address these gaps, the present study proposes a DT-driven approach based on stochastic simulations for the smart design of green hydrogen facilities.

ACKNOWLEDGEMENTS

The research has been supported by the National Research Programme, project "Trends, Challenges and Solutions of Latvian Gas Infrastructure Development" (LAGAS) (No. VPP-EM-INFRA-2018/1-0003).

REFERENCES

1. PwC. (2020). *The Dawn of Green Hydrogen. Maintaining the GCC's Edge in a Decarbonized World*. Available at https://www.strategyand.pwc.com/m1/en/reports/2020/the-dawn-of-green-hydrogen/the-dawn-of-green-hydrogen.pdf
2. Kobzars, V., Zemite, L., Jasevics, A., Kleperis, J., Dimanta, I., Knoks, A., & Lesnicenoks, P. (2021). Appropriateness of hydrogen production in low-power hydropower plant. Paper presented at the *2021 IEEE 62nd International Scientific Conference on Power and Electrical Engineering of Riga Technical University, RTUCON 2021 - Proceedings,* doi:10.1109/RTUCON53541.2021.9711687
3. Kleperis, J., Boss, D., Mezulis, A., Zemite, L., Lesnicenoks, P., Knoks, A., & Dimanta, I. (2021). Analysis of the Role of the Latvian Natural Gas Network for the Use of Future Energy Systems: Hydrogen from RES. *Latvian Journal of Physics and Technical Sciences, 58* (3), 214–226. doi:10.2478/lpts-2021-0027
4. Edwards, P., Kuznetsov, V., & David, B. (2007). Hydrogen Energy. Philosophical Transactions. *Series A, Mathematical, Physical, and Engineering Sciences, 365*. DOI: 10.1098/rsta.2006.1965
5. National Grid. (n.d.). *Energy Explained*. Available at https://www.nationalgrid.com/stories/energy-explained/hydrogen-colour-spectrum
6. Sadik-Zada, E.R. (2021). Political Economy of Green Hydrogen Rollout: A Global Perspective. *Sustainability, 13*, 13464. https://doi.org/ 10.3390/su132313464
7. Colombia, Sipa. (2021.) *Hydrogen Fact Sheet: Production of Low-Carbon Hydrogen*. Available at https://www.energypolicy.columbia.edu/sites/default/files/pictures/HydrogenProduction_CGEP_FactSheet_052621.pdf
8. Nnabuife, S.G., Ugbeh-Johnson, J., Evaristus Okeke, N., & Ogbonnaya, C. (2022). Present and Projected Developments in Hydrogen Production: A Technological Review. *Carbon Capture Science & Technology*, *3*. https://doi.org/10.1016/j.ccst.2022.100042
9. IEA. (2021). *Global Hydrogen Review 2021*. Available at https://www.iea.org/reports/global-hydrogen-review-2021/executive-summary

10. COM (2020) 301 final. Communication from the Commission to the European Parliament, the Council, the European Economic and Social Committee and the Committee of the Regions. *A Hydrogen Strategy for a Climate-Neutral Europe*. Available at https://ec.europa.eu/energy/sites/ener/files/hydrogen_strategy.pdf
11. HM Government. (2021). *UK Hydrogen Strategy*. Available at https://assets.publishing.service.gov.uk/government/uploads/system/uploads/attachment_data/file/1011283/UK-Hydrogen-Strategy_web.pdf
12. UNECE. (2021). *Technology Brief. Hydrogen*. Available at https://unece.org/sites/default/files/2021-10/Hydrogen%20brief_EN_final_0.pdf
13. Gasforclimate. (2020). *European Hydrogen Backbone. How a Dedicated Hydrogen Infrastructure can be Created*. Available at https://gasforclimate2050.eu/wp-content/uploads/2020/07/2020_European-Hydrogen-Backbone_Report.pdf
14. US. Department of Energy. (2020). *Department of Energy Hydrogen Program Plan*. Available at https://www.hydrogen.energy.gov/pdfs/hydrogen-program-plan-2020.pdf
15. CSIS. (2022). *China Unveils its First Long-Term Hydrogen Plan*. Available at https://www.csis.org/analysis/china-unveils-its-first-long-term-hydrogen-plan
16. COAG Energy Council. (2019). *Australia's National Hydrogen Strategy*. Available at https://www.industry.gov.au/sites/default/files/2019-11/australias-national-hydrogen-strategy.pdf
17. Australian Government. (2022). *Growing Australia's Hydrogen Industry.* Available at https://www.industry.gov.au/policies-and-initiatives/growing-australias-hydrogen-industry
18. Li, J-Q., Li, J-C., Park, K., Jang, S-J., & Kwon, J-T. (2021). An Analysis on the Compressed Hydrogen Storage System for the Fast-Filling Process of Hydrogen Gas at the Pressure of 82 MPa. *Energies*, *14* (9): 2635. https://doi.org/10.3390/en14092635
19. Preuster, P., Papp, C., & Wasserscheid, P. (2016). Liquid Organic Hydrogen Carriers (LOHCs): Toward a Hydrogen-free Hydrogen Economy. *Accounts of Chemical Research, 50* (1). doi: 10.1021/acs.accounts.6b00474.
20. US. Department of Energy. (n.d.). *Hydrogen Benefits and Considerations*. Available at https://afdc.energy.gov/fuels/hydrogen_benefits.html
21. Scientific American. (2018). *CO2 Emissions Reached an All-Time High in 2018*. Available at https://www.scientificamerican.com/article/co2-emissions-reached-an-all-time-high-in-2018/
22. Tholen, L., Leipprand, A., Kiyar, D., Maier, S., Küper, M., Adisorn, T., & Fischer, A. (2021). The Green Hydrogen Puzzle: Towards a German Policy Framework for Industry. *Sustainability, 13,* 12626. https://doi.org/10.3390/su132212626
23. Stamatakis E., Perwög E., Garyfallos E., Millán M.S., Zoulias E., & Chalkiadakis N. (2022). Hydrogen in Grid Balancing: The European Market Potential for Pressurized Alkaline Electrolyzers. *Energies*, *15* (2): 637. https://doi.org/10.3390/en15020637
24. Espegren, K., Damman, S., Pisciella, P., Graabak, I., & Tomasgard, A. (2021). The Role of Hydrogen in the Transition from a Petroleum Economy to a Low-Carbon Society. *International Journal of Hydrogen Energy, 46* (45). https://doi.org/10.1016/j.ijhydene.2021.04.143.
25. Clean Energy Partnership. (n.d.). *Background Info FCH Regions' Initiative*. Available at https://www.clean-hydrogen.europa.eu/get-involved/regions-hub/background-info-fch-regions-initiative_en
26. Jaribion, A., Khajavi, S., Ohman, M., Knapen, A., & Holmstrom, J. (2020). A digital twin for safety and risk management: A prototype for a hydrogen high-pressure vessel. In *15th International Conference on Design Science Research in Information Systems and Technology*, (pp. 369–375), 2–4 December 2020. Kristiansand, Norway. doi: 10.1007/978-3-030-64823-7_34

27. Savickis, J., Zemite, L., Zeltins, N., Bode, I., Jansons, L., Dzelzitis, E., & Ansone, A. (2020). The Biomethane Injection into the Natural Gas Networks: The EU's Gas Synergy Path. *Latvian Journal of Physics and Technical Sciences*, *57* (4), 34–50. doi: 10.2478/lpts-2020-0020
28. ADBA. (2021). *Biomethane & Hydrogen. Two Green Gases, One Future. Biogas Insights 2*. Available at https://www.greengastrading.co.uk/wp-content/uploads/2021/07/ADBA-Hydrogen-and-biomethane-Decarbonising-gas.pdf
29. World Nuclear Association. (2020). *Electricity Transmission Systems*. Available at https://world-nuclear.org/information-library/current-and-future-generation/electricity-transmission-grids.aspx
30. Bolobov, V.I., Latipov, I.U., Popov, G.G., Buslaev, G.V., & Martynenko, Y.V. (2021). Estimation of the Influence of Compressed Hydrogen on the Mechanical Properties of Pipeline Steels. *Energies*, 14.
31. Mitsubishi Power. (n.d.). *MHPS Successfully Tests Large-Scale High-Efficiency Gas Turbine Fuelled by 30 % Hydrogen Mix*. Available at https://power.mhi.com/news/20180119.html
32. EC. (2021). *Hydrogen Valleys. Insights into the Emerging Hydrogen Economies around the World*. doi: 10.2843/133091
33. Air Products. (2012). *Air Products' U.S. Gulf Coast Hydrogen Network Enhanced Reliability from the World's Largest Hydrogen Pipeline*. Available at https://microsites.airproducts.com/h2-pipeline/pdf/air-products-us-gulf-coast-hydrogen-network-datasheet.pdf
34. Re-Stream. (2021). *Study on the Reuse of Oil and Gas Infrastructure for Hydrogen and CCS in Europe*. Available at https://www.concawe.eu/wp-content/uploads/Re-stream-final-report_Oct2021.pdf
35. UNECE. (2020). *Report of the Group of Experts on Gas*. Available at https://unece.org/sed/documents/2022/04/reports/report-group-experts-gas
36. ENTSOG. (2021). *ENTSOG Summary of Proposals for Addressing Hydrogen Regulation in the Revision of the 3rd Energy Gas Package*. Available at https://www.entsog.eu/sites/default/files/2021-06/202106%20-%20Position%20-%20ENTSOG%20-%20Open%20PC%20Hydrogen%20Gas%20Market%20Decarbonisation%20Package.pdf
37. Van Gend, C. (2021). *Hydrogen Economy: Opportunities and Risks in the Energy Transition*. Available at https://www.propertycasualty360.com/2021/05/12/hydrogen-economy-opportunities-and-risks-in-the-energy-transition/
38. HyDeploy. (n.d.). *Hydrogen is Invisible and does not Smell. How will we Know if there is a Leak*? Available at https://hydeploy.co.uk/faqs/hydrogen-invisible-not-smell-will-know-leak/
39. EDF. (2022). *For Hydrogen to be a Climate Solution, Leaks must be Tackled*. Available at https://www.edf.org/blog/2022/03/07/hydrogen-climate-solution-leaks-must-be-tackled
40. Allianz. (2022). *Fire, Natural Catastrophes and Faulty Workmanship Top Causes of Insurance Claims for Business: Allianz.* Available at https://www.agcs.allianz.com/news-and-insights/news/claims-review-2022.html
41. Sandeep Kumar, D., & Manish, V. (2019). Effect of Hydrogen in Advanced High Strength Steel Materials. *International Journal of Hydrogen Energy,* 44 (51). doi: 10.1016/j.ijhydene.2019.08.149
42. EHB.(2022).*European Hydrogen Backbone. European Hydrogen Infrastructure Vision Covering 28 Countries*. Available at https://ehb.eu/files/downloads/ehb-report-220428-17h00-interactive-1.pdf
43. ACER. (2021). *Possible Regulation of Hydrogen Networks.* Available at https://www.acer.europa.eu/en/Gas/Documents/ACER%20H2%20Paper_%20vFinal_clean.pdf
44. EP. (2022). *EU Directive on Gas and Hydrogen Networks.* Available at https://www.europarl.europa.eu/RegData/etudes/BRIE/2022/729303/EPRS_BRI(2022)729303_EN.pdf

45. *Directive 2009/73/EC of the European Parliament and of the Council of 13 July 2009 concerning common rules for the internal market in natural gas and repealing Directive 2003/55/EC*. Available at https://eur-lex.europa.eu/legal-content/EN/ALL/?uri=celex%3A32009L0073
46. EP. (2022). *EU Directive on Gas and Hydrogen Networks*. Available at https://www.europarl.europa.eu/thinktank/en/document/EPRS_BRI(2022)729303
47. Sandia National Laboratories. (2019). *Hydrogen Quantitative Risk Assessment.* Available at https://www.hydrogen.energy.gov/pdfs/review19/scs011_muna_2019_o.pdf
48. ToolBox. (n.d.). *Fuels—Higher and Lower Calorific Values.* Available at https://www.engineeringtoolbox.com/fuels-higher-calorific-values-d_169.html
49. Savickis, J., Zemite, L., Bode, I., & Jansons, L. (2020). Natural Gas Metering and its Accuracy in the Smart Gas Supply Systems. *Latvian Journal of Physics and Technical Sciences*, *57* (5). https://doi.org/10.2478/lpts-2020-0026
50. Le Duigou, A., Bader, A–G., Lanoix, J.–C., & Nadau, L. (2017). Relevance and Costs of Large-Scale Underground Hydrogen Storage in France. *International Journal of Hydrogen Energy*, *42* (36). https://doi.org/10.1016/j.ijhydene.2017.06.239.
51. Storengy. (2021). *Large Scale Hydrogen Storage – the Underground Perspective.* Available at https://www.storengy.de/en/medias/news/large-scale-hydrogen-storage-underground-perspective
52. Dopffel, N., Jansen, S., & Gerritse, J. (2021). Microbial Side Effects of Underground Hydrogen Storage – Knowledge Gaps, Risks and Opportunities for Successful Implementation. *International Journal of Hydrogen Energy*, *46* (12). https://doi.org/10.1016/j.ijhydene.2020.12.058.
53. EIA. (2015). *The Basics of Underground Natural Gas Storage*. Available at https://www.eia.gov/naturalgas/storage/basics/

sciendo

LATVIAN JOURNAL OF PHYSICS
AND TECHNICAL SCIENCES
2022, N 4

DOI: 10.2478/lpts-2022-0034

ANALYSIS OF REMOTELY PILOTED AIRCRAFT PAYLOAD FOR OIL SPILL DETECTION

V. Zavtkevics[1]*, M. Urbaha[2]

[1] Riga Technical University, Institute of Aeronautics,
Department for Transport Systems and Logistics
8 Lauvas Str., Riga, LV-1019, LATVIA
*e-mail: vladislavs.zavtkevics@rtu.lv
[2] Latvian Maritime Academy,
12-k1 Flotes Str., Riga, LV-1016, LATVIA
e-mail: margarita.urbaha@latja.lv

Operational monitoring of large sea aquatorium areas with the aim of detecting and controlling oil pollution is now carried out using various technological systems, such as satellite remote sensing, sea-going vessels, various aircraft and remotely piloted aircraft (RPA). Currently, the use of RPA for the fulfilment of monitoring tasks in the aquatorium is being intensively developed and can eliminate problems of remote sensing performed by satellites and piloted aircraft, such as short presence in the monitoring area, very long delay of information (up to 48 hours) and low quality of imagery. This paper presents mathematical modelling of RPA multi-sensor payloads for oil spill detection, monitoring and control. Information obtained from payload sensors is critical for increasing effectiveness of detection and monitoring of oil spills. Nowadays, many types of sensors are used for oil spill detection and monitoring. The most common sensors for detection of oil pollution are optical, multispectral, hyperspectral, thermal and laser fluorometers. Some oil pollution detection sensors have limitations, such as false alarm, only daytime operation, weather restrictions. Airborne remote sensors cannot provide all information required for detection of and response to oil spills, and water quality monitoring in the spill area. A model for selecting sensors for multi sensor payload that will make it possible to optimize the application of RPA for oil spill detection was developed. The RPA payload can be increased/reduced to the greatest possible extent with the help of different types of equipment at various parameters. The mathematical model of the integrated payload considers detection capability of sensors, weather conditions, sensor characteristics, and false alarm rate. The optimal multi-sensor payload will optimize the application of RPA for oil spill detection and monitoring.

Keywords*: Mathematical model, oil pollution, RPA, RPA payload, water quality.*

1. INTRODUCTION

The most critical environmental and ecosystem problem is oil pollution of the sea aquatorium. The Baltic Sea is special when compared to other seas. The pollution does not disappear so quickly from it because the Baltic Sea has a very weak water exchange with the World Ocean. The ecological condition of the Baltic Sea also causes serious concern for environmentalists, social scientists and responsible organisations. The main reason is the increase in oil pollution as a result of the expansion of the oil and gas industry and the increase in vessel traffic [1]. The growth of oil transport volumes increases the risk of marine pollution with oil products; thus, it is necessary to develop a highly effective programme for oil pollution monitoring, based on innovative technologies. Nowadays, the environmental monitoring of sea waters requires particular attention in order to detect and monitor oil spills as well as control water quality parameters in the spill area. Operational monitoring of large sea aquatorium areas with the aim of detecting oil pollution is now carried out using various technical devices – satellites, seagoing vessels and various aircraft. Satellite platforms equipped with synthetic aperture radar (SAR) application are limited in operation by the wind speed and wave height [2], [3]. The number of detected oil spills has been constantly decreasing as a result of intensive aerial surveillance in the Baltic Sea, which indicates to the ships that they are constantly being watched [4]. The existing air surveillance methodology has serious deficiencies, such as the limited number of flight hours, especially at night, high operation cost and the necessity to reduce flight hours due to maintenance of aircrafts. Currently, the use of RPA for the fulfilment of monitoring tasks in the aquatorium is being intensively developed. The Water Framework Directive (WFD) 2000/60/EC requires Member States to implement monitoring programmes for prevention and elimination of pollution of the marine environment with oil as well as to conduct a comprehensive overview of the ecological and chemical status of water quality. Taking into account that oil spills cannot be completely eliminated, the main objective is to develop multi-sensor RPA payloads for more efficient and sustainable water monitoring and management in line with the WFD 2000/60/EC requirements. The actual service can certainly be improved by integrating additional observations as well as new sensors and platforms, for example, RPA [5].

Remote sensing data are used for many purposes, such as oil spill detection, monitoring, surveillance of static and dynamic parameters, slick thickness, border and movement mapping, defining an eliminating strategy. The main types of remote sensing data can be divided into three groups according to oil pollution monitoring flight mission types: detection and confirmation; surveillance of the fate of an oil slick and GIS presentation; physical parameters and water quality in the spill area and monitoring of the border of a slick. Hence, oil pollution monitoring mission can be presented as a set of tasks that shall be performed with maximum efficiency to achieve a defined objective. Performing an oil pollution monitoring mission by using only one specific type of sensors with utility that depends on a particular task does not guarantee reliable completion of the defined complex tasks and high quality of remote sensing data. It is important to divide the use of remote

sensing into the end use or objective, as the utility of the sensor is best defined in this way [6]. The decision regarding the payload sensor set design is complicated due to different types of sensing data, utility of each specific type of sensor and external factors, such as weather and others.

The afore-mentioned requirements and conditions require the development of a special multifunctional multi-sensor payload to perform various tasks, taking into account utility, physical characteristics, constraints of each sensor and mission specifics. Nowadays, the state of the oil spill monitoring can be improved due to the development of the new generation of low weight sensors with improved capability that gives the opportunity to maximize the utility of payloads for RPA by integrating different types of sensors [5]. Design and number of specific types of sensors of multi-sensor payload customized for the oil contamination surveillance mission depend on RPA physical characteristics, such as internal volume of the payload module, maximum carrying weight and mission objectives. The use of small drones requires an analysis of the choice of sensors, based on the limitations of the RPA payload weight, but the estimation of the weight of components cannot ensure that utility of sensors, detecting capability, resistance to false alarms and the influence of external factors are taken into account. The development of a multi-sensor payload is a combinatorial problem the objective of which is to maximize overall utility, detection capability, information quality subject to multiple constraints. It would be feasible to develop a mathematical model for a wide range of RPA that would take into account not only weight and volumetric constraints during the solving process and where all specific types of sensors used to solve problems in oil monitoring missions would be present in a dataset.

This paper focuses on the modelling of an RPA multi-sensor payload for detection of oil spills, static, dynamic parameters, fate of an oil slick and monitoring of the water quality in the spill area. Moreover, a mathematical model for selecting specific types of sensors for multi-sensor payload taking into account mission requirements, restrictions and external factors was developed and described. The main objective of the paper is to consider the problem of selecting sensors for the monitoring of oil contamination of sea aquatorium, using mathematical modelling to maximize utility, detection and reliability of a multi-sensor payload.

2. FORMULATION OF MATHEMATICAL MODEL

Taking into account complexity of the RPA mission for detecting and monitoring oil pollution of the sea aquatorium and various parameters, such as the sensor capability, weather, physical characteristics, etc., to solve the problem of payload optimization, it is advisable to apply a mathematical optimization model. The main objective is to determine the optimal set of payload sensors in order to maximize the efficiency of using RPA while solving the tasks of oil spill identifying and monitoring mission. The selection of the set of sensors for payload restricted by internal volume and weight capacity can be represented as a multi-dimensional knapsack problem (MKP). In this variant of the MKP, the set of all items is partitioned, and one item from each partition must be selected [7]. A multi-dimensional knapsack problem is a flexible approach to optimization of the complicated problem with many constraints in practical

applications. Many practical decision processes can be represented by an appropriate combination of several binary decisions [8]. Internal volume and weight capacity of the payload, weather, detection capability, false alarm factor, day/night operation represent multiple dimensions of the knapsack. Approaching selection of sensors for the multi-sensor payload as a knapsack problem can be described as a set of potential, feasible solutions that satisfy all the constraints, and the objective function defines the maximal utility value of the multi-sensor payload. $J = \{1,2,\dots,N\}$ will be a set of specific types of sensors that can be used for oil spill detection as well as monitoring of oil pollution and water quality parameters in the spill area. In the mathematical model, the problem is described as a set J and a multi-sensor payload (knapsack) with:

C_j = utility of a specific type of sensors for oil spill detection and monitoring of oil pollution and water quality parameters in the spill area;

W_j = weight of the sensor j;

V_j = volume of the sensor j;

V_p = maximum allowable internal volume of the payload;

W_p = maximum weight capacity of the payload.

In the mathematical model of the multi-sensor payload, is the nonnegative integer decision variable defined as:

$$X_j = \begin{cases} 1 \text{ if the sensor j is selected for the payload,} \\ \text{otherwise } 0. \end{cases} \quad (1)$$

A mathematical model for the selection of a set J of sensors for payload with integer decision variable X_j is formulated as integer liner program $X_j \in \{0;1\}, j = 1,\dots,n$. In the selection procedure, each sensor must be selected only once, selection of a fraction portion of a sensor is prohibited because 0 is in the set. The problem of the selection of sensors for the multi-sensor payload is a maximization problem where one will find a feasible solution that will maximize the value of the objective function in comparison with all feasibility solutions. However, selected items must not exceed resource capacities; this is expressed by the knapsack constraints [9]. Function to be maximized is:

$$\sum_{j=1}^{n} CjXj \quad (2)$$

subject to constraints:

$$\sum_{j=1}^{n} W_j X_j \leq W_p; \quad (3)$$

$$\sum_{j=1}^{n} V_j X_j \leq V_p. \quad (4)$$

Solving the problem of sensor selection for the multi-sensor payload, with many restrictions as a multidimensional knapsack problem will derive the optimal multi-sensor payload as the integer decision variable Xj.

The objective of the RPA payload selection model is to develop a sensor set to be carried out by the RPA during the deployment in missions for detecting oil spills and monitoring water quality in the oil spill area. Each time one uses the RPA, it requires a different combination of payload attached to the aircraft. Finding an appropriate sensor is a difficult task, as the RPA is often predefined [10]. The sensor in the model is described as a sensor with specific parameters using a specific sensor type j and a sensor k of the same type with utility, physical characteristics, capability and other parameters. X_{jk} is a binary variable represented as a sensor k of a specific type of the sensor j. For this purpose, there are two sets, J and K, described in the model. A problem formulated as k sensors with different utility,

parameters and physical characteristics of the set *J* are candidates for being included in the multi-sensor payload. Specific types of sensors for oil pollution detection, oil spill and monitoring of the water quality in the spill:

$$K \in \left\{ \begin{matrix} all\ specific\ types\ sensors\ with\ different \\ utility,\ capability\ and\ physical\ characteristics \end{matrix} \right\}. \quad (6)$$

The model can be solved using integer liner programming methods, taking into account many restrictions. The mathematical model is formulated using *J*, *K* compatible pairs: a specific type of sensor and a sensor *k*. Taking into account model formulation, the objective function is:

$$\left\{ \sum_{j} \sum_{k} C_{jk} X_{jk} \right\}, \quad (7)$$

where C_{jk} – utility value of the compatible pair *J, K*;
X_{jk} – a binary variable represented as a sensor *k* of a specific type of the sensor *j*.

This formulation of the model allows determining a multi-sensor payload for oil pollution monitoring, taking into account utility of separate sensors and restrictions formulated in the model. Each distinct sensor selection variant for the multi-sensor payload adds the most effective sensors to the payload and increases its utility. The weighted value of utility was analysed at the first stage using SWOT analysis matrix and determined base on the Analytic Hierarchy Process (AHP) analysis. Presenting the binary variable X_{jk} as compatible pairs of two sets *J, K* allows including only one specific sensor type for oil pollution detection and monitoring in the set of possible solutions:

$$\sum_{k} \left(JK(j,k), X_{jk} \right) = 1. \quad (8)$$

This approach allows excluding duplicates of specific sensor types with equivalent properties, performance and capability during the process of selection from the sets *J* and *K*. The development of a model, where one considers selection and inclusion of different sensors in the multi-sensor payload for complex tasks of oil pollution surveillance, can help improve the design of the payload.

Dimensions and weight constraints of sensors must be considered when selecting a multi-sensor payload for the RPA at the design stage. In the model, constraints of physical characteristics are presented by two equations:

$$\sum_{j=1}^{n} \sum_{k=1}^{n} W_{jk} X_{jk} \leq W_p; \quad (9)$$

$$\sum_{j=1}^{n} \sum_{k=1}^{n} V_{jk} X_{jk} \leq V_p, \quad (10)$$

where W_{jk} is the weight of the k sensor; X_{jk} is an integer variable the value of which is equal to one sensor *k* of specific sensor type *j*, selected as a candidate for being included as a part of the multi-sensor payload, and zero otherwise; V_{jk} is the volume occupied by the sensor *k* of a specific sensors type *j*.

The constraints in the mathematical model are formulated considering sensor capabilities and operation restrictions defined by external factors, such as weather conditions, day or night missions and remote operation.

Weather constraints ensure consideration of weather conditions in the mission area and provide maximum effective usage of sensors in the defined weather conditions:

$$\sum_{j=1}^{n} \sum_{k=1}^{n} WTH_{jk} X_{jk} \leq weather, \quad (11)$$

where WTH_{jk} – a value 0 or 1 of specific sensor type j operation performance in the defined weather conditions; $weather$ is weather criteria that define weather conditions when planning an RPA mission.

Weather conditions, analysing weather restrictions for implementation of all sensor types, are divided into two types. For a sensor with the following operational parameters: surface wind < 18 m/s, wave height < 4 m (weather type 0), value of operation performance is 0, whereas for surface wind < 15 m/s, wave height < 3.5 m (weather group 1) value is 1. For weather of type 0, weather criterion is 0, and for weather of type 1, weather criterion is n number of specific types of sensors. This model presentation allows using weather criteria to optimize sensor selection for a mission with heavy weather conditions. The capacity to perform a particular task and work under certain environmental conditions (e.g., topography, weather) is sensor-dependent [5], [11]. Analysing oil pollution accident statistics, it has been found that there is high probability that an accident happened in bad weather conditions. These weather conditions created obstacles for detection, monitoring and additional RPA oil pollution surveillance mission tasks. Sensors in the model with weather parameters 0 are intended for severe weather conditions and can be selected for a special multi-sensor payload module for bad weather. In case weather condition criterion is 0, the model will select only sensors compatible for weather type 0; otherwise, all sensors.

To improve oil spill detection capability, a constraint based on detection capability of sensors is included in the model.

$$\sum_{j=1}^{n} \sum_{k=1}^{n} DET_{jk} X_{jk} \geq DETECTmin, \quad (12)$$

where DET_{jk} – a weighted value of oil spill detection capability for specific type sensor k; $DET_{jk} \in [0,1]$; $DETECTmin$ – a minimal weighted value of oil spill detection capability in comparison with all sensors.

The weighted value of detection capability was evaluated and calculated on the basis of SWOT analysis and AHP analysis using such criteria as identification probability and performance parameters. This approach allows providing selection for including specific sensor types in the model, starting from the minimal detection capability, and using the strong options for all specific sensor types. Optical sensors, such as video cameras, are widely used in remote sensing for initial detection and surveillance of oil spills and, as candidates for inclusion in a selection set with other sensors, will maximize the detection probability and capability of a multi-sensor RPA payload. Video cameras are mainly used in conjunction with filters to improve contrast for the initial detection of a possible oil spill [5].

Selecting more than one sensor for a multi-sensor payload will reduce the possibility of false alarm for oil pollution detection and reduce the necessity to confirm false detection. A false image resembling an oil spill, which may be caused by the shadow of a cloud, the convergence of cold and warm water, muddy and warm water, floating algae and sandbanks, has to be checked using a standard algorithm, the same as for possible oil pollution [5]. The constraint based on false alarm rejection capability of each specific type of sensors, which will be selected as candidates in a multi-sensor payload, allows reducing misdetections to the minimum possible value:

$$\sum_{j=1}^{n} \sum_{k=1}^{n} FALSED_{jk} X_{jk} \leq FALSEDETmin, \quad (13)$$

where $FALSED_{jk}$ – a weighted value for sensor resistance to false alarms caused by external factors, such as weather, sea surface conditions, biogenic films and other environmental conditions, of specific sensor type sensor $FALSED_{jk} \in [0,1]$; $FALSEDETmin$ – a weighted value for the acceptable maximum number of false detections.

During oil spill detection and monitoring missions, the main problem is false detection probability that differs for different specific types of sensors. In the model, the capability to resist false alarms was estimated and predicted using SWOT analysis and AHP process matrices with a group of criteria. Using only one sensor cannot provide reliable recognition of pollution and exclude false alarms. Only a complex solution, such as a multi-sensor payload created by the optimization model with a set of different sensor types, can realize efficient monitoring, reduce the number of mistakes and cancel confirmation procedures. The objective of the model is to reduce to the minimum the probability of false alarms caused by weather conditions, sunlight or biological sheen.

A constraint for operation efficiency in the day or at nighttime is included in the model. Some types of sensors can operate only in daytime or may be affected by sunlight. Visible spectrum optical sensors have a better quality of oil spill imagery due to having a higher resolution than other specific types of sensors. A constraint that allows defining the operating time gap of a multi-sensor payload during the selection of sensors is formulated in the model. This solution allows modelling a multi-sensor payload for different airframe types of RPA with distinct operation parameters, such as mission duration without recharging of energy. If an RPA has limited flight time and is equipped by a module payload equipment that allows fast change of payloads, the operation criteria allows optimizing the payload for surveillance only during the day or night.

The constraint for operation during particular daytime:

$$\sum_{j=1}^{n} \sum_{k=1}^{n} DAYNIGHT_{jk} X_{jk} \leq DAYNIGHT_{CRITERIA}, \quad (14)$$

where $DAYNIGHT_{jk} X_{jk}$ – a value 0 or 1 for operation possibility in the time period of 24 hours of a specific sensor type j; $DAYNIGHT_{CRITERIA}$ is operation criteria during day or at nighttime that define RPA mission planning time during daytime, nighttime and 24 hours.

The implementation conception of modular design improves the possibility of including in multi-sensor payload specific types of sensors for immediate response to the required task for small low cost RPA airframes. Specific types of sensors in the set J were divided into groups according to their operation ability: only daytime and 24 hours. Using SWOT analysis, all sensor types were analysed, and for the sensors restricted by daytime, $DAYNIGHT_{jk}$ was defined as 0 and otherwise 1. In the mathematical model, three multi-sensor mission payload scenarios can be realised: 24-hour operation, daytime and nighttime by changing $DAYNIGHT_{CRITERIA}$.

During the monitoring of oil contamination in the sea aquatorium, one of the main tasks is to obtain information about pollution parameters, such as geometrical parameters of an oil slick border, static and dynamical changes, product type and oil layer thickness. The objective of reliable oil pollution monitoring is to use strong options of specific types of sensors because only one sensor type cannot define pollution parameters with maximum efficiency due

to operation capability restrictions caused by external factors. The impact of a given oil discharge is highly determined by the nature of the hydrocarbons in the oil [12].

$$\sum_{j=1}^{n} \sum_{k=1}^{n} INFO_{jk} X_{jk} \geq INFO_{min}, \quad (15)$$

where $INFO_{jk}$ is a weighted value of information utility about oil spill parameters for the specific type of sensor k; $INFO_{min}$ is a minimum weighted value of information utility about oil spill parameters in comparison with all sensors.

The weighted value of information utility was analysed at the first stage, using a SWOT analysis matrix, and determined on the basis of AHP analysis. The AHP matrix was used as the main criteria, such as information about the product, oil layer thickness, possibility of pH and DO (Dissolved oxygen) measurement. To maximize the efficiency of the multi-sensor payload, the model will select remote sensors that can give approximate information about the type of product, thickness of an oil sheen, sampling devices and water quality sensors while in operation.

For specific types of RPA, such as airframes with fixed wings with high altitude in model, a restriction for including only remote sensors can be added:

$$\sum_{j=1}^{n} \sum_{k=1}^{n} REMOTE_{jk} X_{jk} \leq remoteoperationcrit, \quad (16)$$

where $REMOTE_{jk}$ is a value 0 or 1 of a specific sensor type k for the capability of remote operation; is remote operation criteria that define the type of sensing activities of a multi-sensor payload.

For sensors that are designed only for remote sensing, the value of $REMOTE_{jk}$ is 0. For example, for selection of a sensor set for an RPA with fixed wing airframe, the remote operation criteria will be defined as 0, and the model will select only remote sensors k while in operation.

The model determines the optimal solution for including specific types of sensors in the set for a multi-sensor payload that maximally improves efficiency and reliability of oil pollution surveillance missions. The SWOT analysis shows that the integrated payload has more advantages than a single sensor [5]. The optimization process is based on a complex approach, taking into account utility value of each sensor and sensor detection capability, information capability and capability to reject false detections that are defined by constraints. In the model, constraints define operation restrictions caused by external factors, such as weather conditions, daytime or nighttime operation, remote operation; this formulation allows optimizing specific types of sensor selection as candidates for a multi-sensor payload for different deployment modes using all types of RPA platforms. The developed model can be used for the whole range of RPA and for the new design RPA projects with a multi-sensor payload for detecting various oil spills, monitoring and defining water quality parameters in the spill area.

3. MODEL RESULTS

In this section, results of the launch of the numerical model for selection of specific types of sensors are presented. The developed model is employed to optimize the selection of specific sensor types from the defined data set *J, K* as candidates for the multi-sensor payload.

To launch the model, two main options

were selected based on the weight and internal volume of the mini-RPA payload. The model was working for the mini-RPA category: RPA with payload maximum weight equal to 1.0 kg, internal volume – 1000 cm3 and RPA with payload maximum weight equal to 1.2 kg, internal volume – 1300cm3.

The necessary input data of specific types of sensors *J* and sensors *K* to perform a case study of the model are presented in Table 1.

Table 1. Input Data

Specific types of sensors *J*	Sensors *K*
Visible range of electromagnetic spectrum sensors	High-resolution camera Multispectral camera Ultraviolet camera with minimum UV sensitivity equal to 7.8 x 10-18 watt/cm² Ultraviolet camera with minimum UV sensitivity equal to 2.6 x 10-18 watt/cm²
Hyperspectral imaging sensors	Visible and near-infrared (VNIR) hyperspectral camera Short-wave infrared (SWIR) hyperspectral camera
Infrared range of electromagnetic spectrum sensors	Thermal imaging infrared camera with a resolution of 336X256 Thermal imaging infrared camera with a resolution of 640X215 Light detection and ranging sensor
Conductivity sensors	Conductivity sensor with a measuring range of 500–200,000 µs Mini-conductivity sensor with a measuring range of 1,300 µs to 40,000µs
pH sensors	pH sensor with an accuracy of +/– 0.01 mini pH sensor with an accuracy of +/– 0.002
DO sensors	DO sensor with a measuring range of 1–100 mg/L, accuracy of +/- 0,05 mg/L Mini DO sensor with a measuring range of 1–50 mg/L, accuracy of +/- 0,2 mg/L
Sampling devices	Sampling device [13] (Urbahs and Zavtkevics, EP20150174649) Sampling device [14] (Urbahs and Zavtkevics, LV patent application P-15-88 2015-08-20)

During the use of the model, while performing the monitoring of oil pollution using an RPA, the constraints were set as the most probable. The weather criterion for the model input was specified for the marine environment with the following parameters: surface wind < 15 m/s; wave height < 3.5 m. The detection value was defined as to be included in the process of selecting visible spectrum sensors. To improve the quality of alarms in case of the detection of a probable oil spill as well as to increase resistance to false alarms, was defined. In case of model simulation, the missions were planned during a 24-hour period. The minimum value of the weighted utility of the information about oil spill parameters was set to minimum to allow all sensors to participate as candidates for selection. Due to the requirements to achieve maximum efficiency of the multi-sensor payload, remote operation criteria were set in order to allow all specific types of sensors to participate in the selection.

The time required for the calculation of the optimal solution of the model for the composition of a sensor set is 473 milliseconds.

The results obtained after the launch of the model under these conditions are presented in Table 2.

Table 2. The Results: Sensor Sets Selected for the Multi-Sensor Payload

Option 1: Payload with the maximum weight of 1.2 kg and an internal volume of 1300 cm3	Option 2: Payload with the maximum weight of 1 kg and an internal volume of 1000 cm3
Multispectral camera VNIR hyperspectral camera Thermal imaging infrared camera with a resolution of 336X256 Mini-conductivity sensor with a measuring range of 1,300 µs to 40,000 µs Mini-PH sensor with an accuracy of +/– 0.002 Mini-DO sensor with a measuring range of 1–50 mg/L, accuracy equal to +/- 0.2 mg/L Sampling device [13]	Multispectral camera Thermal imaging infrared camera with a resolution of 336X256 Mini-conductivity sensor with a measuring range of 1,300 µs to 40,000 µs Mini-PH sensor with an accuracy of +/– 0.002 Mini-DO sensor with a measuring range of 1–50 mg/L, accuracy equal to +/- 0.2 mg/L Sampling device [13]

4. CONCLUSIONS

In the research, the problem of selecting a sensor set was analyzed, and the mathematical model for the optimization of the multi-sensor payload for oil pollution monitoring of sea aquatorium was formulated.

The developed model determines a set of specific types of sensors, taking into account utility value of the separate sensor evaluated and calculated on the basis of SWOT analysis and AHP analysis, and considers sensor capabilities, such as detection, information and rejection of false detection defined by constraints. Operation restrictions caused by external factors, such as weather conditions, daytime or nighttime operation, remote operation, are defined by constraints in the mathematical model; this formulation of the model allows optimizing the process of selection of specific types of sensors as candidates for the multi-sensor payload for different deployment modes, using all types of RPA platforms. Taking into consideration the complexity of the requirements for the missions of the monitoring of oil pollution in the sea aquatorium and various parameters, such as utility, capability, physical characteristics of sensors and environment conditions, it is advisable to use the mathematical optimization model for the optimization of the multi-sensor payload used. This model can be widely used for the planning of the missions of environmental monitoring of oil pollution performed using different types of RPA in different operational conditions, taking into account external factors. The application of mathematical modelling to optimize the choice of sensors allows maximizing the effectiveness of the multi-sensor payload to solve the tasks of oil pollution monitoring. The optimized multi-sensor payload, used for oil pollution monitoring, will minimize the number of RPA missions, time and energy consumption due to the possibility of performing all the necessary tasks and the absence of secondary missions for confirmation, monitoring of the fate of spilled oil and water quality in the spill area. The present research has demonstrated that the use of the multi-sensor payload will maximize the probability of detecting an oil spill, rejecting false detections and providing the responsible organizations with the information about parameters of pollution and the quality of water in the area of the spill. The developed model can be used as a tool for

designing, customizing and analysing RPA payloads for environmental monitoring of the sea aquatorium and internal waters.

ACKNOWLEDGEMENTS

The research has been supported by the European Regional Development Fund within the Activity 1.1.1.2 "Post-doctoral Research Aid" of the Specific Aid Objective 1.1.1 "To increase the research and innovative capacity of scientific institutions of Latvia and the ability to attract external financing, investing in human resources and infrastructure" of the Operational Programme "Growth and Employment" (No.1.1.1.2/VIAA/4/20/650).

REFERENCES

1. Urbahs, A., & Zavtkevics V. (2020). Oil Spill Detection Using Multi Remote Piloted Aircrafts for Environmental Monitoring of Sea Aquatorium. *Environmental and Climate Technologies, 24* (1), 1–22. https://doi.org/10.2478/rtuect-2020-0001
2. Urbahs, A., & Zavtkevics, V. (2014). Oil pollution monitoring of sea aquatorium features with using unmanned aerial vehicles. In *17th International Conference Transport Means*, (pp.75–78). 23–24 October 2014, Lithuania, Kaunas: Kaunas University of Technology.
3. Garello, R., & Kerbaol, V. (2017). Oil pollution monitoring: An integrated approach. In *IEEE Workshop on Environmental, Energy, and Structural Monitoring Systems (EESMS)*, (pp.1–6). 24–25 July 2017, Italy, Milan. https://doi.org/10.1109/EESMS.2017.8052689
4. HELCOM. (2020). *HELCOM Annual Report on Discharges Observed during Aerial Surveillance in the Baltic Sea 2019*. Available at https://helcom.fi/wp-content/uploads/2021/02/Aerial-surveillance-in-the-Baltic-Sea-2019.pdf
5. Urbahs, A., & Zavtkevics V. (2019). Oil Spill Remote Monitoring by Using Remote Piloted Aircraft. *Aircraft Engineering and Aerospace Technology, 91*, 648–653. https://doi.org/10.1108/AEAT-12-2017-0273
6. Fingas, M. (2011). *Oil Spill Remote Sensing.* New York: Gulf Publishing Company.
7. Martello, S., & Toth, P. (1990). *Knapsack Problems: Algorithms and Computer Implementations.* USA: John Wiley & Sons, Inc.
8. Kellerer, H., Pferschy, U., & Pisinger, D. (2004). *Knapsack Problems*. Berlin: Springer.
9. Puchinger, J., Raidl, G., & Pferschy, U. (2010). The Multidimensional Knapsack Problem: Structure and Algorithms. *INFORMS Journal on Computing, 22*, 250–265. https://doi.org/10.1287/ijoc.1090.0344
10. Klimkowskaa, A. Leea, I., & Choia, K. (2016). Possibilities of UAS for maritime monitoring. In *XXIII ISPRS Congress. The International Archives of the Photogrammetry, Remote Sensing and Spatial Information Sciences, Volume XLI-B1*, (pp. 885–891). 12–19 July 2016, Czech Republic, Prague. https://doi.org/10.5194/isprs-archives-XLI-B1-885-2016
11. Gomez, C., & Green, D. (2017). Small Unmanned Airborne Systems to Support Oil and Gas Pipeline Monitoring and Mapping. *Arabian Journal of Geosciences, 10*, 202. https://doi.org/10.1007/s12517-017-2989-x
12. Kerr, R. (1977). Oil in the Ocean: Circumstances Control its Impact. *Science, 198* (4322), 1134–1136. https://doi.org/10.1126/science.198.4322.1134

13. Urbahs, A., & Zavtkevics, V. (2017). *Unmanned Aerial Vehicle for Collecting Samples from the Surface of Water.* EU patent EP3112840 (A1). (Application No. EP20150174649 20150630, 30.06.2015).
14. Urbahs, A., & Zavtkevics, V. (2015). *Water Sampling Method of Oil Pollution and for Analysis Using Unmanned Aerial Vehicle with Fixed Wings and Device for Method Perform*. LV patent application P-15-88 2015-08-20.
15. Glizde, N., & Urbaha, M. (2019). Remotely Piloted Aircraft System Air Vehicle Type Selection. *Engineering for Rural Development, 18,* 1302–1312. doi:10.22616/ERDev2019.18.N241.

sciendo

LATVIAN JOURNAL OF PHYSICS
AND TECHNICAL SCIENCES
2022, N 4

DOI: 10.2478/lpts-2022-0035

DEVELOPMENT SOLUTIONS OF RIGA CITY LOCAL GEODETIC NETWORK

A. Celms[1], J. Kaminskis[2], J. Akmentins[3], I. Varna[4*]

[1]Latvia University of Life Sciences and Technologies,
Department of Land Management and Geodesy,
19 Akadēmijas Str., Jelgava, LV-3001, LATVIA
[2]Riga Technical University
Department of Geomatics
1 Meža Str., Riga, LV-1048, LATVIA
[3]Riga City Council City Development Departament
4 Amatu Str, Riga, LV-1003, LATVIA
[4*]University of Latvia, 3 Jelgavas Str., Riga, LV-1004, LATVIA
*e-mail: inese.varna@lu.lv

Throughout the centuries, Riga has been the city with dynamic development. Its territory has unceasingly expanded, whereby previously unused territories have been urbanized. Managers of the city understood already at the end of 19th century that unified geodetic network had great importance in the development of the city. Since then, Riga's local geodetic network has evolved with the city, several coordinate and height systems have been replaced, but the task has remained the same – to provide a flawless, homogeneous geodetic foundation for various surveying activities. In 2018, the development of the local geodetic network in several parts of the city was completed, whereby the problem arose – altitude values of surveyed terrain points determined by using the improved geodetic network did not coincide with altitude values determined using the GNSS method. Considering the above-mentioned problem, the objectives of this study were set: to plan and carry out control measurements of the improved local geodetic network in the vicinity of Grizinkalns, to provide analysis of the obtained results and recommendations for further development of a local geodetic network. The difference between the heights determined by the geometric levelling method and the heights determined by the GNSS method shall not exceed 2 mm. According to the GNSS method, using the quasi-geoid model LV'14 v2, the determined heights of the geodetic grid points differ from the given ones by 0.062 m on average. The differences are systematic. To overcome these differences, the quasi-geoid model needs to be refined.

Keywords: *Geodesy, GNSS, levelling, quasi-geoid model.*

1. INTRODUCTION

The purpose of the local geodetic network is to provide the necessary geodetic reference points for surveying in the relevant administrative area. Geodetic reference points are needed for cadastral survey, for obtaining highly detailed topographic data, for geodetic works in construction, ensuring precise ties of designed engineering structures and buildings to the terrain [1]. After completing the local geodetic network development in several neighbourhoods of Riga in 2018, it was found that height values for surveyed terrain situation points determined using the optimized geodetic network did not coincide with height values determined using the GNSS (Global Navigation Satellite Systems) method. Therefore, the aim of the study is to provide an assessment of the accuracy of the local geodetic network and give recommendations for its improvement. For that purpose, we develop a control measurement plan and perform control measurements for the improved local geodetic network in the Grizinkalns neighbourhood and provide an analysis of the obtained results.

In order to achieve the aim, control measurements have to be made between the points of the class N1 levelling network of and the upgraded points of the local Riga geodetic network; GNSS measurements performed at selected points 6475 and 626a of the class N1 levelling network and at points 6618, 6600 of the local geodetic network; the heights determined by GNSS method have to be compared with those obtained by geometric levelling; analysis of the results of the control measurements has to be carried out and suggestions to the local geodetic network development solutions have to be proposed. This study is based on geodetic theory which is supporting determination of the precise figure of the Earth, including traditional land surveys and GNSS technique.

2. MATERIALS AND METHODS

The history of development of Riga local geodetic network is almost 140 years long [2], [3]. According to the results of the local geodetic network survey in 2012 and 2013, only 55.2 % of the local network geodetic points were recognized as normal for use in Riga, and many (34.5 %) destroyed points were detected (Fig. 1) [4]. To solve the situation, Riga Local Geodetic Network Development Concept for 2014– 2022 was developed. According to the concept, the renovation and development of the local geodetic network is underway [5].

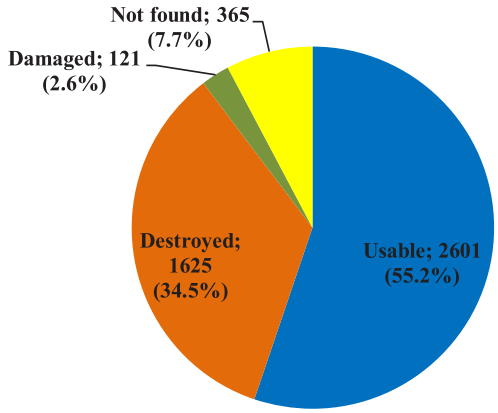

Fig. 1. Results of the inspection of the local geodetic network in 2012–2013.

Grizinkalns is neighbourhood in Latgale Suburb of Riga, although it is partially situated in the central region of Riga. Neighbourhoods and their boundaries in Riga are formed taking in account the geographical, cultural-historical and functional factors with gentle attitude to toponyms. They are not considered administrative units. There are cases, when individual neighbourhoods are situated in several administrative regions at the same time.

The total area of Grizinkalns neighbourhood is 1.517 km², the length of its perimeter is 5547 m. Construction of this neighborhood was started at the end of 19th century in an empty place. It developed as a typical worker suburb, where workers of nearby factories lived.

Several points of the local geodetic network were destroyed as a result of diverse reconstruction works – construction works of revitalization of Grizinkalns Park, reconstruction works of Daugava Stadium, Deglava Bridge and Vagonu Street. It is planned to restore points after the completion of construction works.

To improve the local geodetic network in Riga, surveys in Grizinkalns neighbourhood were started in 2009, but technical report on completed works was compiled in 2010 [6]. Actually, the territory of the research included also Avotu neighbourhood, but the plan of the improvement of the network was called "Grizinkalns".

The improvement of the local geodetic network was done before the Regulations of the Cabinet of Ministers No. 497 of 24 July 2012 "Local Geodetic Network Regulations" came into force. After 24 July 2012, the improved local geodetic network of Grizinkalns could not be used legally for topographic and cadastral surveying.

From 2010, coordinates of Continuously Operating Reference Station (CORS) network LatPos reference station "Ojars" were recalculated, two CORS EUPOS-Riga reference stations were moved. On 1 December 2014, a new height reference system LAS-2000,5 was implemented.

Due to these reasons, it was necessary to carry out recalculation of the previously determined coordinates and heights of the improved local geodetic network and examine it in the procedure defined by regulatory acts in state agency "Latvian Geospatial Information Agency".

On 27 October 2017, state agency "Latvian Geospatial Information Agency" gave a positive opinion on the improvement of the local geodetic network "Riga local geodetic network in territories "Centre", "Maskavas forstate" and "Grizinkalns"". From this moment, the use of the improved local geodetic network of Grizinkalns became legal for topographic and cadastral surveying.

Unfortunately, when active use of the improved geodetic network in surveying works started, it was found that in the framework of previously performed survey works, where points of network determined by GNSS served as geodetic reference, the determined heights did not match the heights determined by measurements with the improved local geodetic network.

Research of a similar nature has been carried out at the Finnish Geospatial Research Institute (FGI), which is testing various direct and indirect surveying methods, combining different geodetic instruments and techniques, such as GNSS and tachymetric surveys. Complex data processing and analysis, as well as critical evaluation has been performed [7].

Due to this reason, it was decided to perform control measurements of the local geodetic network of Grizinkalns neighbourhood and to find out the reasons of discrepancy.

Before performing control measure-

ments, plan of measurement campaign was elaborated (Fig. 2). Considering the problem – mutual discrepancy of heights determined by different methods, decision was made to perform geometric leveling works and to measure elevations between points of leveling network N1 and points of the improved local geodetic network, as well as to determine these elevations by the use of GNSS method.

In the framework of this study, recognition of the area was performed, points of state geodetic leveling network N1 and points of the local geodetic network: wall mark No. 626a, ground mark No. 6475, fundamental mark No. 3378, polygonometry points No. 6600 and No. 6618 were inspected. Such activities were performed to make sure that the above points of national and the local geodetic network could be found in the field and used, as well as to determine the best trajectories of leveling lines.

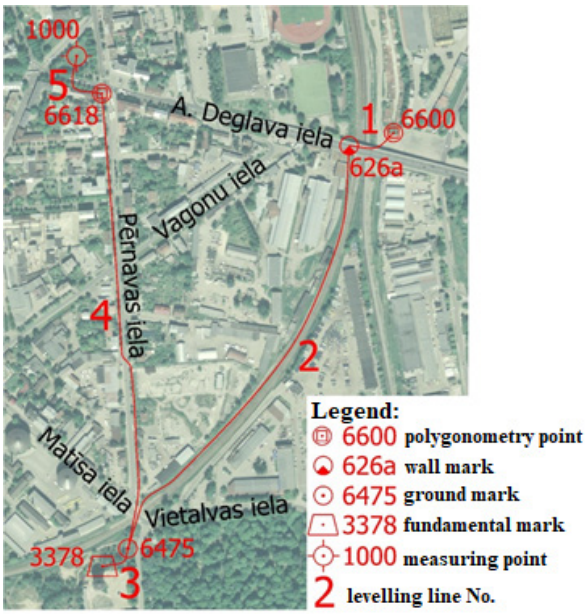

Fig. 2. Scheme of performance of control measurements.

As a result of recognition of the area and inspection of geodetic points, the following decisions have been made:

- 1st leveling line shall be drawn between polygonometry point No. 6600 and wall mark No. 626a;
- 2nd leveling line shall be drawn from wall mark No. 626a up to ground mark No. 6475 along the railway, along unused track;
- 3rd leveling line shall be drawn from ground mark No. 6475 and fundamental mark No. 3378;
- 4th leveling line shall be drawn from ground mark No. 6475 up to polygonometry point No. 6618 along Pērnavas Street;
- 5th leveling line shall be drawn between polygonometry point No. 6618 and measuring point No. 1000 that shall be fixed in the field with temporary mark.

The 1st and 5th leveling lines are necessary to transfer height determined by GNSS method for wall mark No. 626a and polygonometry point No. 6618 by geometric leveling. The 2nd and 3rd leveling lines

are measured between points of class N1 leveling network in order to examine the previously measured elevations. The 4th leveling line is necessary to examine tie of the point of local geodetic network to the state geodetic point.

Geometric leveling was performed by digital level Trimble DiNi and two 3 m long barcode invar rods. Digital level Trimble DiNi with 0.3 mm standard deviation to 1 km double traverse is one of the most stable and durable instruments; it is intended for precision measurements, establishing the geodetic networks, construction and observation of deformations.

GNSS measurements were performed in three points: ground mark No. 6475, polygonometry point No. 6600, measurement network point No. 1000 (see Fig. 2) to determine their heights. Leica Viva GS14 was used for the GNSS measurements. In each point, measurement session duration was 5 hours. GNSS measurements were performed on 2 March 2019 for polygonometry point No. 6600, 3 March 2019 for ground mark No. 6475 and 28 March 2019 for measurement network point No. 1000.

The GNSS data post-processing was performed by Bernese GNSS Software v5.2 [8] in a double-difference mode. The final CODE precise orbits, Earth orientation and clock products, and final ionosphere product were used. A cut-off elevation angle of 3° was selected. The positions of all stations were corrected for solid Earth tide effect and ocean tide loading. The dry Global Mapping Function was used as the a priori troposphere model, and zenith path delay parameters were estimated using the wet Global Mapping Function. 6 CORS stations were used as reference stations: LatPos station OJAR and five EUPOS-Riga stations, all of them located in the city of Riga.

3. RESULTS AND DISCUSSION

As fundamental mark (fr) No. 3378 and ground mark (gr) Nr. 6475 were installed already in leveling works of class II in 1975, it was possible to compare the measured heights of year 1979 (h_{1979}), heights available in the database of the state geodetic network ($h_{VĢTDB}$) and measurements performed in the framework of this study ($h_{measured}$). Elevation between ground mark No. 6475 and wall mark (sr) No. 626a can be compared only with heights available in the database of the state geodetic network. Comparison is given in Table 1.

Table 1. Historical and Measured Elevations

Type of point, No.	h_{1979} (m)	$h_{VĢTDB}$ (m)	$h_{measured}$ (m) 2019.g.	$\Delta h_{1979-} h_{VĢTDB}$ (m)	$\Delta h_{VĢTDB}- h_{measured}$ (m)
fr 3378	-1.156	-1.157	-1.158	-0.001	-0.001
gr 6475					
gr 6475	n/a	-2.770	-2.772	n/a	-0.002
sr 626a					

The measured elevations ($h_{measured}$) between ground mark No. 6475 and point of the local geodetic network No. 6618, wall mark No. 626a and point of the local geodetic network No. 6600 can be compared with the elevations ($h_{VĢTDB}$) that

are obtained by calculating the difference between heights of geodetic points available in the database of state geodetic network and heights published in the overview of improved local geodetic network in Grizinkalns. Comparison is given in Table 2.

Table 2. Calculated and Measured Elevations

Type of point, No.	$h_{VĢTDB}$ (m)	$h_{measured}$ (m) 2019.g.	$\Delta h_{VĢTDB-} h_{measured}$ (m)
gr 6475	-2.336	-2.331	0.005
cs 6618			
sr 626a	-1.840	-1.842	-0.002
cs 6600			

As the comparison of the measured elevations shows, heights of points of the local geodetic network are determined by linking to points of class N1 state geodetic network.

To investigate the discrepancy between heights of points of the improved local geodetic network and heights determined by GNSS method, it is necessary to compare elevations obtained from geometric leveling with elevations obtained by the GNSS method. The measured elevations and their comparison are summarised in Table 3.

Table 3. Comparison of Geometric Leveling and GNSS Elevations

Type of point No.	Geometric leveling elevation (m)	GNSS measured elevation LAS 2000,5 (m)	Δ geometric leveling-GNSS LAS2000,5 elevation (m)
gr 6475	-2.331	-2.333	-0.002
cs 6618			
sr 626a	2.772	2.773	-0.001
gr 6475			

Quasi-geoid model LV'14 v2 was used to calculate LAS 2000,5 heights. Elevations, which were determined by geometric leveling methods, and elevations, which were determined by GNSS post-processing, differed within limits of few millimeters.

For a complete picture on the problematic of usage of the improved local geodetic network for performance of geodetic works, it is necessary to compare heights determined by GNSS method using quasi-geoid model LV'14 v2 with heights available in the database of the state geodetic network and heights of the improved local geodetic network. Their comparison is given in Table 4.

Table 4. Comparison of Heights of Geodetic Points

Type of point, No.	H LAS 2000,5 given (m)	H LAS 2000,5 measured (m)	ΔH given-measured (m)
fr 3378	16.509	16.543	-0.034
gr 6475	15.352	15.385	-0.033
sr 626a	12.582	12.621	-0.039
cs 6618	13.016	13.069	-0.053
cs 6600	10.742	10.779	-0.037
Average:			**-0.039**

Systematic height differences of geodetic points in the territory of Grizinkalns show that these points should not be used for the purpose of surveying works.

Heights of these points do not satisfy the accuracy requirements stipulated by Point 24.1 of Regulations of the Cabinet of Ministers No. 281 issued on 24 April 2012 "Regulations for the Topographic Information of High Detail and its Central Database" – whilst repeated survey of the corresponding territory, difference of heights for clearly visible objects and contours shall not exceed 3 cm [9].

Considering the results obtained in control measurements and their analysis, it is necessary to improve the quasi-geoid model in the territory of the city. It is important to be able to use both the improved points of the local geodetic network and GNSS method as geodetic base of surveying in future to obtain compatible results.

It is necessary to continue to improve the local geodetic network in densely built-up areas and areas of new development, to provide homogenous geospatial data for administration, municipality and economic purposes.

The authors propose three solutions to improve Riga local geodetic network (see Table 5).

Table 5. Riga Local Geodetic Network Development Solutions

No.	Geodetic network solution	Note
1	Improved and fixed local geodetic network for the entire territory of the city.	The most expensive solution that will require large financial investments and regular maintenance but will provide homogenous geospatial information.
2	Improved and fixed local geodetic network in densely built-up areas and areas of new development + CORS network in other areas of the city.	Optimal solution that will provide homogenous geospatial data both in densely built-up areas and outside of them. However, it is mandatorily necessary to improve the accuracy of quasi-geoid model in the territory of the city.
3	CORS network for the entire territory of the city.	Solution that has been the only legal geodetic reference for surveying 2012–2018. It does not require large financial investments, but it is mandatorily necessary to improve the accuracy of quasi-geoid model in the territory of the city.

4. CONCLUSIONS

Geodetic measurements were performed in the selected research area, followed by data processing, repeated measurements, processing and analysis were performed, including previously known measurement results. The results include comparison of the data with the results obtained for different time periods, complex data analysis and identification of systematic processes, their exclusion, visualization and predicted impact of the obtained result on future processes. The following conclusions and suggestions for improvement of the local geodetic network have been drawn:

1. Riga local geodetic network has rich history of more than 100 years long. It contains geodetic points that are measured in various time periods with different accuracy. They make the geodetic network that does not comply with the requirements of Regulations of the Cabinet of Ministers.

2. During establishment of Riga local geodetic network, a wide range of geodetic instruments have been used: starting with old optical instruments and ending with modern electronic devices that maximally exclude the factor of human errors, improve the efficiency and accuracy of geodetic works.
3. The main improvements that contributed to accuracy of measurements is implementation of electronic distance measurement, automatization of readings and recording, electronic measurement data processing and implementation of GNSS technologies in civil usage.
4. Geometric leveling works that were performed in the framework of this research corresponded to accuracy requirements of leveling of class I.
5. Results of control measurements performed between points of class N1 leveling network show that N1 network in Grizinkalns neighbourhood is stable; changes of mutual elevation of leveling marks fixed in the area do not exceed 2 mm.
6. Mutual differences of elevations determined by geometric leveling and of elevations determined by GNSS method do not exceed 2 mm.
7. Heights of geodetic network points determined by GNSS method and using quasi-geoid model LV'14 v2 differ from the given catalogue values by 0.039 m in average. Differences are systematic. To eliminate these differences, it is necessary to improve accuracy of the quasi-geoid model.
8. To provide credible geospatial data according to Regulations of the Cabinet of Ministers, it is necessary to use the state geodetic network, improved local geodetic network as a geodetic reference or to tie survey network to the above-mentioned ones.

REFERENCES

1. Cabinet of Ministers. (2012). *Vietējā ģeodēziskā tīkla noteikumi*. [*Regulations of Local Geodetic Network*]. Regulations No 497 as of 4 July 2012. Available at https://likumi.lv/doc.php?id=250460 (In Latvian).
2. Kletnieks, J. (2014). *Astronomija un ģeodēzija Latvijā līdz 20.gadsimtam.* [*Astronomy and Geodesy in Latvia till 20th Century*]. Riga: University of Latvia (In Latvian).
3. Silabriedis, G. (2010). Rīgas ģeodēziskā vertikālā tīkla vēsture un nākotne. [Riga Geodetic Vertical Network: History and Future]. *Scientific Journal of Riga Technical University, 7*, 14–26 (In Latvian).
4. Rīgas vietējā ģeodēziskā tīkla pilnveidošanas pārskats teritorijās "Centrs", "Maskavas forštate" un "Grīziņkalns". [*Riga Local Geodetic Network Improvement Report in Areas "Centre", "Maskavas Forstate" un "Grizinkalns"*]. (2017). Riga (In Latvian).
5. Reiniks, M. (2013). *Rīgas vietējā ģeodēziskā tīkla atīsīības koncepcija 2014. – 2022. gadam*. [*Riga Local Geodetic Network Development Concept for 2014–2022*]. Riga (In Latvian).
6. Ģeodēziskā tīkla tehniskā atskaite. Ģeodēzisko datu atjaunošana Rīgas pilsētas centrālajā daļā, no A. Čaka ielas līdz dzelzceļam. [*Technical Report of Geodetic Network. Renewal of Technical Data in the Central Part of Riga from A.Caka Street to Railway*] (2010). Riga (In Latvian).
7. Kallio, U., Koivula, H., Nyberg, S., Hakli, P., Rouhiainen, P., Saaranen, V., … & Golovka, V. (2012). GNSS antenna offset field test in Metsähovi. In *Knowing to Manage the Territory, Protect the Environment, Evaluate the Cultural Heritage: FIG Working Week 2012*, (pp. 1–5). 6–10 May 2012. Italy, Rome.

8. Dach, R., Lutz, S., Walser, P., & Fridez, P. (2015). *Bernese GNSS Software Version 5.2.* Astronomical Institute, University of Bern, Bern, Switzerland.
9. Cabinet of Ministers. (2012). *Augstas detalizācijas topogrāfiskās informācijas un tās centrālās datubāzes noteikumi.* [*Regulations for the Topographic Information of High Detail and its Central Database*]. Regulations No 281 as of 24 April 2012. Available at https://likumi.lv/doc.php?id=%20246998 (In Latvian).